XFEL.EU TR-2014-001

TECHNICAL DESIGN REPORT

Scientific Instrument High Energy Density Physics (HED)

July 2014

M. Nakatsutsumi, K. Appel, G. Priebe, I. Thorpe, A. Pelka,
B. Muller, and Th. Tschentscher
for the Scientific Instrument HED (WP82)
at European XFEL

European X-Ray Free-Electron Laser Facility GmbH
Albert-Einstein-Ring 19
22761 Hamburg
Germany

Contents

1 Executive summary

This technical design report (TDR) of the High Energy Density Physics scientific instrument (HED instrument) at the European XFEL outlines the scientific and technological requirements for the various subsystems and describes the technical realization chosen to match these requirements.

The scientific requirements have been extracted from a range of proposed scientific applications at the HED instrument. Most of these applications had been discussed in the past years as the core of scientific activity at the HED instrument, but, with the recent start of operation of the Matter in Extreme Conditions instrument at the Linac Coherent Light Source (LCLS) at SLAC National Accelerator Laboratory in Menlo Park, California, several new ideas and applications have been included. High energy density (HED) matter is generally defined as having an energy density above 10^{11} J·m^{-3}, which is equivalent to 100 GPa (1 Mbar) pressure and 500 T magnetic pressure.

Key science applications at the HED instrument will include the following:

- Solid-matter properties following extreme excitation by various means
- Solid matter in states of extreme pressure and density exceeding parameters that can be reached using static compression techniques
- Complex solids in very high pulsed magnetic fields
- Warm dense matter (WDM) and hot dense matter (HDM) systems
- Isochoric creation of WDM using X-ray free-electron laser (FEL) radiation
- Plasma physics in the relativistic-electron regime
- Quantum states generated by extremely high-field laser pulses

Experiments and applications in these scientific areas are generally performed in pump–probe mode, where a first pulse (X-ray or optical laser) excites a sample, and a second pulse (typically, X-ray) probes the sample a defined delay time later.

Requirements have been identified for the X-ray delivery, optical laser (OL) parameters, corresponding diagnostics, vacuum operation conditions, sample exchange, and detection channels and detectors. In addition, operational parameters, such as ease of use and high efficiency of setup and operation, have been considered. Finally, fast turnover of experiments has to be possible in order to enable a large number of experiments per year and high efficiency during the scheduled beam time.

The X-ray beam delivery system is designed to keep the X-ray beam location in the experiment room laterally fixed, even for varying beam sizes, photon energies, or monochromaticity conditions. For this purpose, inline focusing optics and monochromators have been selected. For some configurations of beam transport, a vertical offset of a few millimetres remains. The X-ray beam optics system includes mirrors for beam steering, beryllium compound refractive lenses for focusing, silicon channel-cut crystals for monochromatization, and a multilayer-based X-ray beam split and delay unit (SDU). The SDU will be provided through external funds. Slits and an attenuator unit allow beam definition, and several diagnostics units are installed for measuring intensity, beam position and size, arrival time, and spectrum. In normal operation, the entire X-ray beam path up to the X-ray beam energy absorber at the very end of the X-ray beam transport will be located in a window-less vacuum system. Operation of the interaction areas in air may be possible in special cases. The majority of elements of the X-ray beam delivery system are designed for the high repetition rate and burst mode delivery of X-ray pulses specific to the European XFEL. By this choice, a large degree of flexibility can be maintained at the HED instrument, even if, to date, many applications request only an X-ray pulse repetition of 10 Hz or less. Table 1-1 shows a brief summary of the X-ray performance at the HED instrument.

Table 1-1. *Overview of X-ray FEL beam parameters at the HED instrument*

Photon energy	Photon number on sample	Maximum intensity	Smallest spot size	Largest spot size	Energy
keV	/pulse	$W \cdot cm^{-2}$	µm	mm	mJ
5–24	> 10^{12} at 5–10 keV > 10^{11} at > 10 keV	> 10^{17}	2–3	> 1	~ 3 mJ at 5 keV, > 1 mJ for < 20 keV > 0.7 mJ for > 20 keV
3–5	> 10^{12}	> 10^{16} *	~ 4 *	> 1	> 1 mJ

* For a few selected energies

Three OL systems will be available at the HED instrument for driving samples into extreme states. A high-energy optical laser will be used for shock and shock-less compression experiments. An ultrahigh-intensity optical laser reaches focused intensities far beyond 10^{18} $W \cdot cm^{-2}$, allowing the study of relativistic laser–matter interactions. In addition, a pump–probe optical laser provides high repetition rates, thereby matching the X-ray delivery pattern with ~ 1–100 mJ pulse energies. These lasers will be placed in rooms adjacent to the experiment room, and transport lines of 10–20 m in length have been designed. Both high-energy laser systems are provided through external funds (see Section 2.3, “User consortia”, on page 22).

Provisions are taken to include a high-field pulsed magnet setup providing ≥ 30 T magnetic fields. This configuration is still under discussion, and only a placeholder is included.

The layout and configuration of the main interaction chamber represents one of the major new developments of this report. In contrast to the previous setup, which had two chambers for experiments using both X-ray and high-energy optical lasers, the current setup comprises only one large-volume chamber (see Figure 1-1). This chamber will use the horizontal plane to enable highly flexible but preconfigured OL configurations both for pumping and probing the samples. The vertical plane is used for the X-ray scattering

diagnostics, in accordance with the X-ray beam's horizontally linear polarization. Forward direct scattering (e.g. in imaging, powder, or liquid diffraction, or small-angle X-ray scattering) will be recorded in several planes near and far from the sample. At the present stage, the exact choice of detectors has not been made. This report includes instead in Chapter 8, "Detectors and diagnostics", an overview of requirements for the area detectors and some specifications of detectors under consideration.

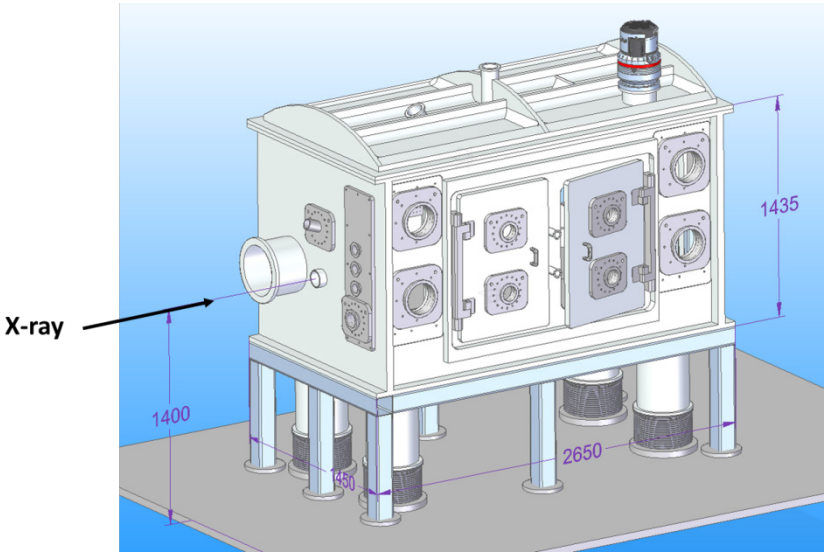

Figure 1-1. *3D model of the main interaction chamber IA1 of the HED instrument*

The complete science scope of the HED instrument is achievable only by integrating additional instrumentation, provided through external funding schemes. The largest of these contributions is through the Helmholtz International Beamline for Extreme Fields (HIBEF) user consortium (UC). This consortium consists of nearly 100 institutes around the globe and has applied for major funding grants in Germany and the UK. In addition, contributions in kind and in personnel are to be expected from many other countries.
A smaller contribution is that of the SDU provided by the University of Münster, Germany, and funded by the German Federal Ministry of Education and Research (BMBF).

The time schedule for constructing and starting operation of the HED instrument includes the following important milestones:

Aug. 2016 Access to hutches inside the experiment hall; start of installation

Apr. 2017 First X-ray beam

Aug. 2017 Early user experiments

Dec. 2017 HED ready for user operation (X-ray and OL commissioned)

Jan. 2019 Full operation with extended performance

The biggest risk to date for building the HED instrument is the integration of the HIBEF UC contributions due to the unclear funding situation. In case funding of this UC or its most important partners is delayed or, in the worst case, does not occur, the high-energy laser systems and several smaller instrumentations will not be available at the beginning of operation of the HED instrument.

2 Introduction

This document describes the technical design of the High Energy Density Physics scientific instrument (HED instrument) at the European XFEL. The HED instrument will be a new, unique platform for experiments combining hard X-ray free-electron (FEL) radiation with the capability to place matter under extreme conditions of pressure, temperature, or electric and magnetic field using high-energy optical lasers or pulsed magnets. Scientific applications will include, but are not limited to, the study of matter within exoplanets, new extreme-pressure phases and solid-density plasmas, and structural phase transitions of complex solids in high magnetic fields.

The current status of the HED instrument is based on the conceptual design report (CDR) for this instrument published in May 2013 [1]. Recent activities have focused on the definition of rooms and infrastructure inside the experiment hall. In order to cope with the overall time schedule of the European XFEL, it became necessary to tender the construction of the concrete walls and roof of the main experiment room (HED-EXP). Due to its weight, it was necessary to construct the enclosure before the final floor finish inside the experiment hall could take place. In January 2014, the contract was awarded, and construction of HED-EXP is scheduled for June 2014.
Another activity focus was the collection, analysis, and refinement of detailed descriptions of experiments to be performed at the HED instrument. Following a suggestion of the HED advisory review team (HED-ART) at the occasion of the review of the CDR, the HED group approached people inside the HED-ART and additional experts to provide these descriptions. An analysis of this process can be found below.

On the occasion of the European XFEL Users' Meeting, held in Hamburg on 29–31 January 2014, a half-day HED user workshop was organized to interact with the future user community of the HED instrument, learn about recent technique developments, provide information on the present status of designing the HED instrument, and discuss the proposed design in all matters of importance to the users.

The time schedule for the European XFEL, and more specifically for the HED instrument, foresees construction of the instrument inside the experiment hall starting in the second half of 2016. First X-ray FEL beam will be provided to the HED instrument by April 2017, and early user experiments are scheduled to start from August 2017. By the end of 2017, the HED instrument, including its OL suite, will be fully commissioned and ready for regular user operation.

2.1 Scope of this document

This TDR outlines the scientific and technological requirements for the various subsystems and describes the technical realization chosen to match these requirements. The status of technical design varies for different subsystems of the HED instrument. The X-ray beam delivery system and the definition of X-ray, control, laser, and rack rooms and their infrastructure requirements are already in a very advanced state. These are the first parts of the instrument to be constructed. The requirements for and realization of the optical lasers and their beam transport systems are also very advanced, but, in this area, some risk still exists that the chosen technology will not be available in the form described in this report. Construction of the laser hardware needs to start by the end of 2014 at the latest. Another focus of this report is the main interaction chamber (IA1). Several technical details of this chamber remain to be worked out before its construction can start. Parts that are defined at a conceptual design level are: the sample replacement and debris protection systems, the detectors to be employed at the HED instrument—importantly, the 2D large-area detectors—and the design of the second interaction zone (IA2). Note that IA2 has several uses, i.e. pulsed-magnet experiments, out-of-vacuum experiments, placement of the area detector for small-angle X-ray scattering (SAXS), and imaging experiments at long distance (3–6 m) from the sample.

Furthermore, this TDR does not describe all baseline features and boundary conditions within which the HED instrument was designed. The reader is referred to the CDR for this information [1]. This TDR focuses on further detailing of instrumentation and on specific issues that were previously

identified for some of the subsystems. Following this introduction, we report on the X-ray delivery system in Chapter 4, “X-ray beam transport”, where we emphasize the description of the X-ray focusing optics designed to achieve a large range of spot sizes, at two locations in the experiment room, for a large range of photon energies.

Chapter 5, “Optical lasers”, presents the OLs, their beam transport systems, and their integration. The current plan for the HED instrument foresees to provide three OL systems at the start of operation. The pump–probe optical laser (PP-OL) can provide laser pulses with the same time pattern as the electron bunches delivered by the accelerator, which subsequently lead to X-ray pulses. This laser will be used for less strong driving of samples, for optical diagnostics of sample excitation, and for cross-correlation measurements of X-ray and OL pulse arrival. Two high-energy laser systems will be available for strongly driven samples. The high-energy optical laser (HE-OL) provides nanosecond, shaped pulses of energies up to 100 J. The ultrahigh-intensity optical laser (UHI-OL) provides 30–50 fs pulses with a peak power at the sample of up to 100 TW. For experiments requesting a time resolution in the sub-picosecond regime, it is critical to synchronize the OL pulses and to measure the actual beam arrival times with femtosecond resolution.

In Chapter 6, “Arrival time monitor”, the implementation of the necessary X-ray-to-OL and OL-to-OL synchronization systems is described.

Chapter 7, “Experiment chamber setups”, describes the interaction chamber and the proposed implementations of the large variety of experimental techniques specific to the HED instrument. The chapter also includes a description of the present design state of the sample replacement system and the debris protection system. The latter is required to shield the OL delivery optics and X-ray instrumentation from debris following laser impact, plasma formation, and hydrodynamic expansion of the sample volume.

Chapter 8, “Detectors and diagnostics”, describes the observations tools employed to study sample transformation. These tools include X-ray detectors and spectrometers as well as optical probe and particle detection techniques. Although optical techniques such as Fourier domain

interferometry (FDI) and velocity interferometer system for any reflector (VISAR) are well established, for the X-ray techniques, the detectors pose a real challenge.

2.2 Experiment details

The scientific objectives of the HED instrument were described in the CDR [1]. Applications were divided into the areas *condensed matter at extreme excitation*, *solid-density plasmas*, and *quantum states of matter*. In its review of the CDR, the HED-ART recommended the development of a detailed experiment plan for a few key experiments from each of these areas. Below, we provide an overview of the scientific applications for which these details have been gathered in collaboration with the scientific community. We further discuss the X-ray and OL techniques to be employed in relation to these applications. Later, we use these selected applications for the X-ray and OL instrumentation at the HED instrument.

The experiment details show that a significant part of the proposed experiments are aimed at studying *condensed matter at extreme states* of temperature, pressure, density, or external field. These experiments typically assume that the sample can be described using condensed-matter theories. The overarching interest lies in the structural dynamics of these systems.

A second large area is the study of *solid-density plasmas*. The focus on solid-density plasmas follows from the possibility of using hard X-ray probes. In contrast, the study of dilute plasmas is possible, and is extensively done, using visible-light techniques. Solid-density plasmas can exist in several states of excitation. In the warm dense matter (WDM) regime, both condensed-matter and plasma theories need to be considered. Hot dense plasmas (HDMs) are generally much closer to ideal, and the study of plasma dynamics is particularly interesting. Finally, relativistic electron plasmas, following extreme excitation and occurring at femtosecond time scales, feature extreme non-equilibrium of electron and ion systems, creating new interaction phenomena.

Table 2-1. *Overview of representative science applications at the HED instrument (FDI: Fourier domain interferometry, IXS: inelastic X-ray scattering, SAXS: small-angle X-ray scattering, VISAR: velocity interferometer system for any reflector, XAS: X-ray absorption spectroscopy, XES: X-ray emission spectroscopy, XI: X-ray imaging, XRD: X-ray diffraction)*

Area	Application	Category	X-ray techniques	OL techniques
Condensed matter at extreme excitation	Laser processing; ultrafast phase transitions	OL pump – X-ray probe	Powder & liquid XRD, SAXS	Sample excitation by ultrashort pulses
	Material properties of high P-T states	OL pump – X-ray probe	Powder & liquid XRD	Dynamic compression (shocks, ramps); VISAR
		X-ray probe	Powder & liquid XRD	Static compression with pulsed laser heating
	X-ray–matter interaction	X-ray pump – X-ray probe	XAS, XES, SAXS	FDI
	Material properties of magnetic phases	Pulsed magnetic field – X-ray probe	Single-crystal XRD	—
Solid-density plasmas	WDM properties of high P-T states	OL pump – X-ray probe	IXS, XAS, XES	Dynamic compression (shocks, ramps); VISAR
	WDM generation	OL pump – X-ray probe	IXS, XAS	Shocks; FDI; VISAR
	Shock propagation; plasma density distribution	OL pump – X-ray probe	XI	Plasma creation and shocking
	Relativistic OL–matter interaction	OL pump – X-ray probe	SAXS, XAS	Plasma creation under relativistic-electron regime
	Faraday rotation by fast electron-induced magnetic field	OL pump – X-ray probe	X-ray polarization	—
Quantum states of matter	Vacuum polarization	OL pump – X-ray probe	X-ray polarization	Extreme E-M field excitation

The third area, *quantum states of matter*, refers to the experimental study of fundamental quantum electrodynamics using highest OL fields and X-ray probing. This last area will need extreme laser fields (at least > 10^{22} W·cm^{-2} or beyond) in order to achieve sizable cross sections. Such laser fields will not

be reached in the first implementation of the HED instrument, and this application will therefore not be considered in detail in this report.

The majority of experiments investigate highly transient processes during which the sample will usually be irreversibly altered and will need to be replaced before the next X-ray or OL pulse arrives. In this context, the issue of employing high repetition rates also becomes relevant. The HED instrument will be designed for a repetition rate of 10 Hz for all experiments requiring fast solid-sample replacement. Only by enabling the use of this moderately high repetition rate will the HED instrument be able to enter the regime where small-signal studies, e.g. in inelastic X-ray scattering (IXS)–type experiments, or systematic parameter studies can be attempted. This higher repetition rate represents a significant difference compared to many high-energy OL facilities, where experimental campaigns often receive much smaller repetition rates or even only a few laser shots. For HED experiments, the 10 Hz operation should be understood as a critical improvement enabling studies that would otherwise be impossible. However, the experimental duty factor will be much lower than 10 Hz because operation at 10 Hz will occur only during a fraction of the available time per experiment campaign. Sample consumption and debris generation for a given experiment campaign will be reduced accordingly. The 10 Hz rate poses significant challenges for the sample replacement and positioning system, the high-energy OLs, and the diagnostics systems. One challenge is that many well-established OL diagnostics schemes rely on charge-coupled device (CCD) area detectors, both for visible light and X-rays. These detectors often have problems combining high frame rates with high dynamics range, low noise, and large frames.

For experiments employing high-speed sample replenishment, e.g. liquid or pulsed gas jets, and for experiments not damaging or heating the samples significantly, instrumentation at the HED instrument allows operation at much higher repetition rates within the X-ray pulse trains (0.1 to 4.5 MHz).

2.2.1 Science applications

This section briefly describes the science applications that constitute the HED portfolio. These applications have been extracted from the detailed user

requirement specifications that were used to define the requirements for the HED subsystems described in this report.

Dynamic compression of matter will allow access of states in the P-T phase diagram not accessible to static high-pressure methods. Using high-energy OL pulses and depending on the OL pulse shape, one can compress matter using shocks or ramped pulses to very high internal pressures. Another method uses diamond anvil cells (DACs) with an attached piezo-driven inducer (dynamic DACs) to apply much higher compression rates than can be probed at present. Also, the study of highly irreversible processes using DACs is expected to become a strong application area. X-ray diffraction (XRD) and X-ray absorption spectroscopy (XAS) as probes of structural and electronic properties are required to study such transformations.

Studies of the transition of matter from solids to warm dense matter and further to ideal plasmas will uniquely benefit from the probing by ultrashort and intense X-ray pulses. These experiments need to measure the properties of the electron and ion systems. Properties of free and correlated electrons, as well as of ions, are of importance. In addition to the absolute parameters of the subsystems, the ability to determine if the plasma is in local equilibrium following the excitation from the cold condensed matter state is an important asset for the further analysis of data and for their modelling. Initial test measurements at the Linac Coherent Light Source (LCLS) at SLAC National Accelerator Laboratory in Menlo Park, California, and at large laser facilities have shown that, in particular, scattering (IXS, liquid XRD) and spectroscopy techniques (XAS) are of great use here.

Relativistic laser–matter interaction processes occur when irradiating solids with very high-intensity OL pulses. Here electrons are accelerated to relativistic energies and propagate through the cold lattice of ions. Strong fields and currents act on the charged particles. These processes are important because they can create charged particles beams, in particular ions or protons, which have been proposed as a next-generation medical therapy protocol. In these relativistic laser–matter processes, several interactions and non-linear phenomena take place in parallel, thereby making these systems very difficult to simulate. In addition, many processes take place on the

femtosecond time scale. X-ray FEL pulses provide the intensity, duration, shape, divergence, and repetition rate to study these systems systematically. SAXS or X-ray photon correlation spectroscopy (XPCS) are exquisite tools to study the mesoscopic length scales of the density modulations in the excited sample volume.

Much smaller laser fields are needed for laser processing of condensed matter. This technological process, already commercially employed by several products, is still in its infancy when it comes to describing the dynamics of structural transitions. As the process is often irreversible, it is important to collect all information from single experimental exposure. X-ray FELs provide the intensity and repetition rate that allow systematic studies. Ultrafast single-crystal, powder, or amorphous-material XRD techniques are required for these studies.

When placing highly complex crystalline solids into extreme magnetic fields, the interaction of the internal, crystalline fields and the external fields can lead to significant structural transitions and to the formation of new phases, and can aid in the development of materials with new properties. The external field strength is critical for such experiments. The highest fields can be achieved using pulsed magnets with pulse durations close to that of the European XFEL X-ray pulse trains (~ 600 µs). Following the structural and electronic dynamics of the crystal along the external field switching will allow the study of the dynamic behaviour of these materials. High-resolution XRD is very sensitive to these structural modifications, and, with the time structure of the European XFEL X-ray pulse delivery, it will be possible to observe the dynamics of the new structure formation.

2.2.1.1 X-ray and OL techniques

Probing structural properties in cold, well-ordered (long-range) matter is typically done by X-ray diffraction (XRD). Depending on the state of the matter in the probe volume, single-crystal, powder, or non-crystalline diffraction techniques may be used. The latter technique is important in the detection of melting and also applies to disordered and ionized plasmas. The further one departs from the ordered condensed-matter state, the more important spectroscopic techniques become. X-ray absorption spectroscopy

(XAS) provides information about structural properties, typically short-range order properties. In addition, electronic properties and electron temperatures can be obtained from the near-edge features using X-ray absorption near-edge structure spectroscopy (XANES; typically, a few 10 eV around the absorption edge). Extended X-ray absorption fine structure spectroscopy (EXAFS; typically, a few 100 eV above the edge) can provide short-range structural information. At present, no schemes exist to provide FEL radiation with such a bandwidth in a single pulse. Thus, EXAFS requires scanning of the X-ray energy in a series of measurements. Special accelerator operation schemes to provide FEL radiation with an enlarged bandwidth are currently under investigation. Inelastic X-ray scattering (IXS) with eV resolution provides information about single electrons and quasi-particles like plasmons. In a high-resolution experiment (hr-IXS) achieving meV resolution, it will be possible to study the properties of the atom cores and ions. X-ray emission spectroscopy (XES) also provides important information on electronic structure and, in the case of Raman spectroscopy, reveals XAS signals containing the information described above. Plasma self-emission spectroscopy (SES) in the visible to X-ray regime occurs for highly excited systems and provides detailed information about atomic and plasma properties inside the solid-density plasmas.

For experiments using DACs, very small spot sizes (< 10 μm) and hard X-rays (> 20 keV) are necessary requirements. Using the high repetition rate of the European XFEL, it will be possible to have as many photons on the sample in a millisecond as currently available in a second. This increase enables experiments not feasible at spontaneous radiation (SR) sources

For optical diagnostics, VISAR and FDI are installed. VISAR [2] is a well-established technique for the characterization of shocks in solid matter by measurement of the rear surface motion [3]. Typically, velocities in the range from few m/s to 10s of km/s can be measured with sub-100 ps temporal resolution. FDI [4][5] measures both the amplitude and the phase of the complex reflection coefficient of an excited solid with high spatial and temporal resolution. These quantities, observed in single-shot measurements, are closely related to both the optical properties of the probed sample and its hydrodynamic evolution.

2.3 User consortia

The design of the HED instrument is planned for the contribution of several key components through external partners. At present, two activities are in progress or in preparation. Funded through the German Verbundforschung (grant applications: 05K10PM2 and 05K13PM1), the group of Helmut Zacharias at University of Münster is designing, is constructing, and will commission a multilayer-based X-ray beam split and delay unit (SDU). This device will be installed inside the tunnel section of the HED X-ray beam transport and will enable X-ray pump – X-ray probe experiments. The device is optimized for high throughput and will allow X-ray–X-ray time correlation experiments. The construction is quite advanced. The device is described in Chapter 4, “X-ray beam transport”.

A second, much larger contribution has been proposed by the Helmholtz International Beamline for Extreme Fields (HIBEF) user consortium (UC). The major components to be contributed by the HIBEF-UC will be a 100 J pulse energy, nanosecond laser system, a 100 TW ultrashort-pulse laser system, their infrastructure, a sample production facility, and a high-field pulsed magnet setup. These contributions will be complemented by the personnel to design, construct, commission, and later operate them, and also by additional X-ray and optical laser instrumentation components. The UC includes a large number of institutions in numerous countries. It is coordinated by Thomas Cowan at Helmholtz-Zentrum Dresden-Rossendorf (HZDR), Germany. Funding will come through several channels in various countries. Proposals are being evaluated at present.

These contributions will be fully integrated into the European XFEL framework and will be available to all users of the HED instrument. In this document, we describe the current state of these components. In doing so, we sometimes refer to them as “external contributions”; in fact, they are considered integral parts of the HED instrument. While the contribution by University of Münster is secured and ongoing, the funding scheme for the HIBEF-UC contributions is not yet settled. The ongoing evaluations are progressing well, but a risk remains that these contributions, or at least a considerable part of them, could become delayed or cancelled.

3 HED hutch layout overview

Before describing the subsystems in detail, this chapter gives a brief overview of the HED instrument hutches located inside the ~ 90 x 50 m^2 underground experiment hall (XHEXP).

3.1 Overview of HED hutches

A top view of the HED hutches in the SASE2 area is shown in Figure 3-1. HED comprises the HED control room (HED-CTR) measuring 7 x 4 m^2, the X-ray optics hutch (HED-OPT) measuring 9 x 2.2 m^2, and the experiment hutch (HED-EXP) measuring 11.4 x 9 m^2 (inside). Clear room heights are 2.7, 3.5, and 4.0 m, respectively. Additional rooms associated with the HED instrument are the instrument laser room (COM-LAS) located immediately before the optics hutch and operated jointly with the Materials Imaging and Dynamics (MID) instrument, the high-power laser hutch (HED-HPLAS) located on top of HED-EXP, and the SASE2 preparation lab (COM-PRP) located to the side of HED-EXP and, once again, operated jointly with MID.

The 100 TW UHI-OL will have its utility installations in the racks and laser utilities room (HED-RCK1) that is located right next to (just south of) HED-HPLAS. This room will include the racks for the electrical installations inside HED-EXP. A further racks and laser utilities room (HED-RCK2), mostly for the 100 J HE-OL, is located next to (north of) HED-HPLAS. These two racks and utilities rooms are accessible from a small mezzanine level above the HED control room.

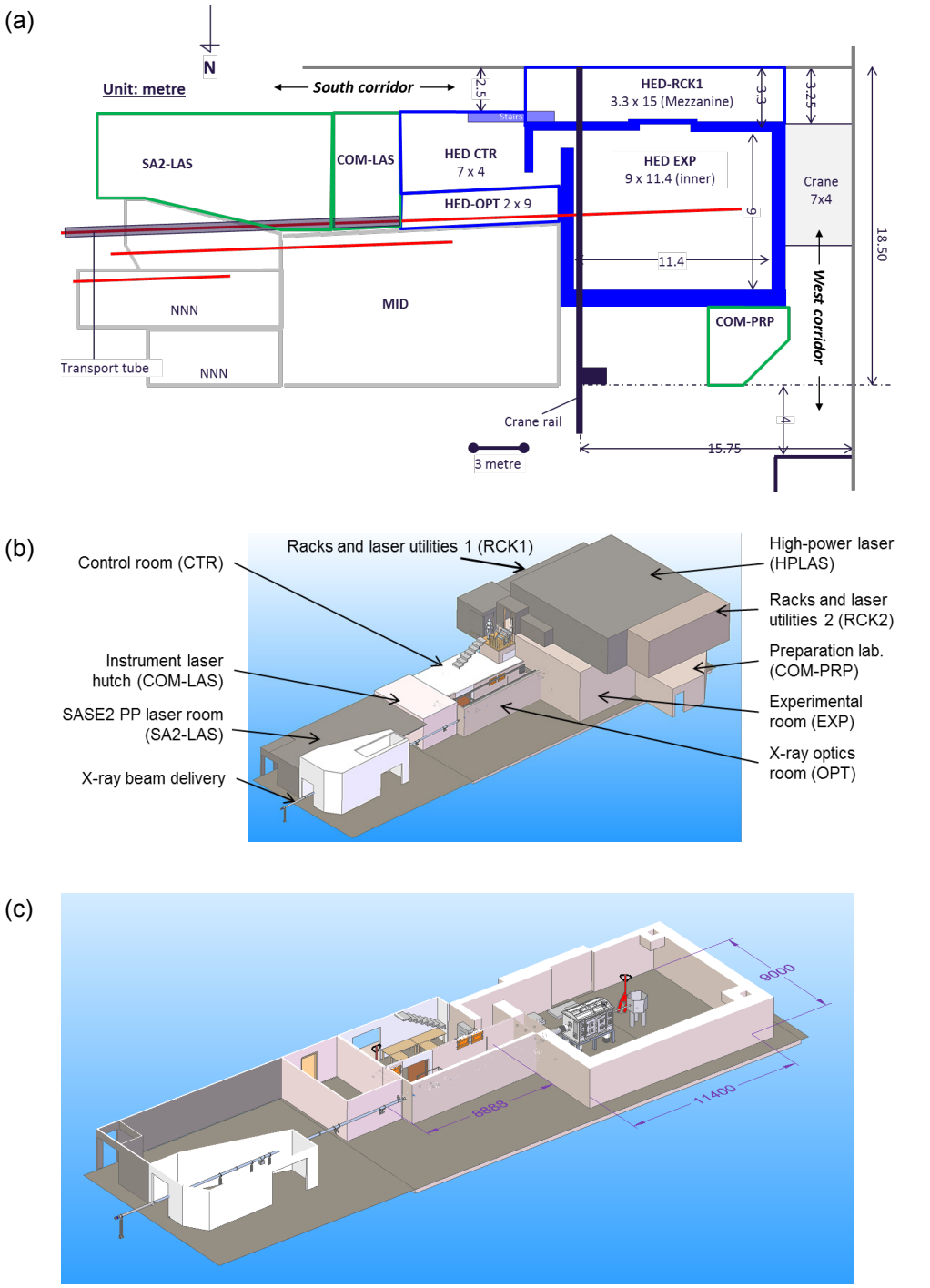

Figure 3-1. *Overview of the HED instrument hutches in the SASE2 area. X-rays come from the left. North is down on the drawing. (a) Top view at the floor level. Red lines indicate the X-ray beam for the HED and MID instruments and an optional third (NNN) instrument. (b)(c) 3D drawings.*

3.2 HED X-ray beam transport

To connect the HED X-ray beam transport in the XTD6 tunnel with the X-ray optics hutch (HED-OPT), a ~ 20 m long vacuum transport without any optical element will be installed. Coming from the XTD6 tunnel, this transfer tube passes first through open space, then through the MID-OPT room, the SASE2 PP-OL room (SA2-LAS), and the MID-EXP room before entering into HED-OPT. A tube diameter of 100 mm is foreseen. The tube centre will be at a height of 140 cm above the floor, and the supports and vacuum pumps will be mounted in a way that minimizes interference with the main usage of these rooms.

3.3 HED control room (HED-CTR)

HED-CTR provides the workspace for the users. Instrument control, data analysis, and miscellaneous activities will be performed here. Figure 3-2 shows a sketch of the room.

HED-CTR is laid out to give users access to HED-OPT and HED-EXP. Transport of components into HED-OPT will be done through HED-CTR. The size of the room is approximately 4.3 x 7 m^2 with an inner height of 2.7 m. The access to HED-EXP is designed as a chicane to avoid radiation leakage from HED-EXP. The chicane will also serve as laser interlock and for clothes changing for cleanroom working conditions inside HED-EXP. Interlock panels for access to HED-OPT and HED-EXP will be installed next to the access doors inside HED-CTR. Stairs outside HED-CTR that partially cover the south façade provide access to the HED-RCK1 and HED-HPLAS rooms on the elevated floor level.

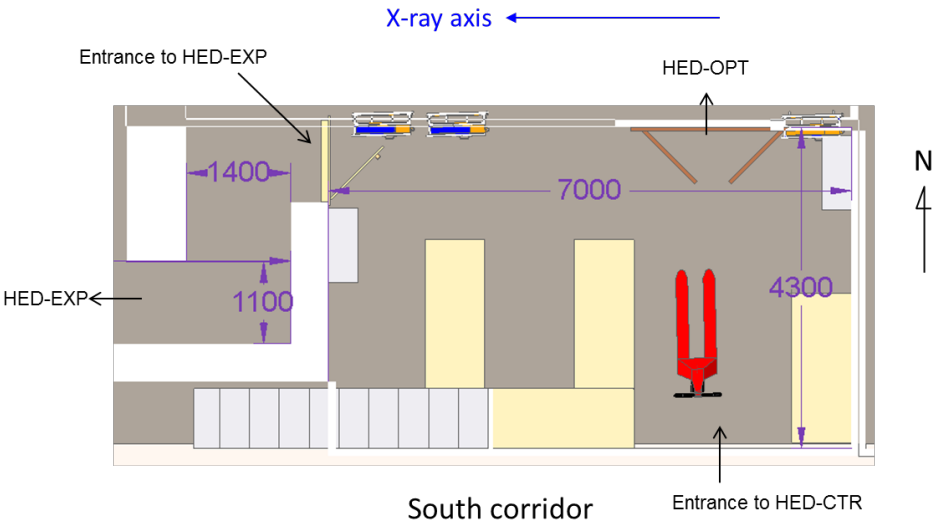

Figure 3-2. *Layout of the HED control room (HED-CTR). Top view (top) and 3D model (bottom).*

3.4 X-ray optics hutch (HED-OPT)

The basic purpose of the HED X-ray optics hutch is the installation of the X-ray beam delivery and diagnostics devices. These devices are the slits, an X-ray screen, the pump–probe laser arrival time monitor, an attenuator unit, one of the compound refractive lens units, a placeholder for an X-ray quarter-wave plate, an I_0 monitor, and a beam shutter. All the devices are under ultrahigh-vacuum (UHV) conditions and connected by vacuum tubes. The height of the X-ray beam determines the mounting height of components at 1400 mm from the floor. Some provision is kept for future developments or small experiment setups.

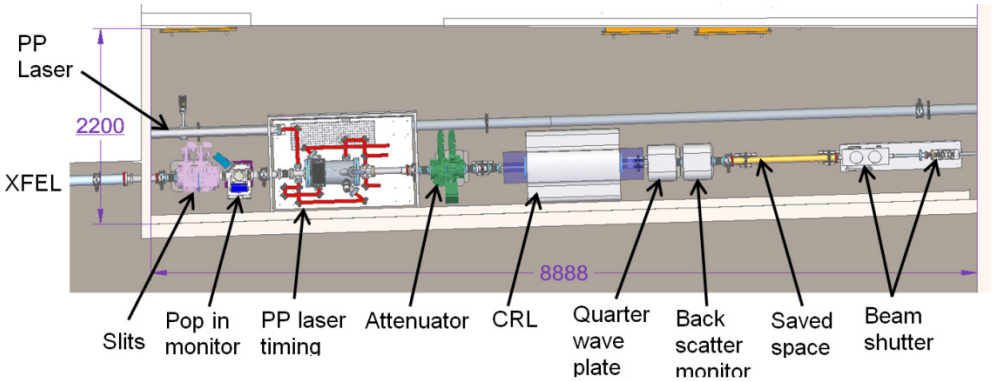

Figure 3-3. *X-ray optics hutch (HED-OPT) viewed towards HED-CTR. The X-ray beam comes from the left.*

The transport of the PP-OL beams occurs through two vacuum tubes parallel to the X-ray beam transport: one for the experiment in HED-EXP (PP line) and a second (timing line) for the cross-correlation measurement of the timing jitter with respect to the X-ray pulse arrival. The PP-line tube runs through the full length of the HED optics hutch and is placed at a height of 1050 mm from the floor and 500 mm south of the X-ray beam. The timing line is placed at a height of 1400 mm from the floor and runs to the timing jitter measurement setup located between slits and attenuator.

3.5 Experiment hutch (HED-EXP)

HED-EXP is the main experiment room where users will carry out experiments at the HED instrument (Figure 3-4). This room measures 11.4 m internally along the beam and is 9 m wide. Its inner clear height is 4 m. Due to secondary radiation generated by the 100 TW UHI-OL, this area has to be enclosed by 50–100 cm thick heavy concrete walls. There are two access points for HED-EXP: a heavy-load door on the south side (3 m wide, 2.5 m high opening) and a chicane entrance from HED-CTR in the southeast corner. The big door allows for the transport of large components. It has to provide the shielding equivalent of the south wall and requires special movement. Personnel access will usually occur through the chicane entrance. In January 2014, the contract for the construction of the HED-EXP enclosure

and the heavy-load door was awarded, and installation is scheduled for June 2014.

HED-EXP will contain the main interaction chamber (IA1) and a second interaction zone (IA2) where several setups, dedicated to specific experiments or techniques, can be used and exchanged. Optical laser transport at present is provided only to IA1, with a defined interaction point 3.5 m from the east wall. The arrangements inside HED-EXP and for IA1 and IA2 are described in more detail in Chapter 7, “Experiment chamber setups”.

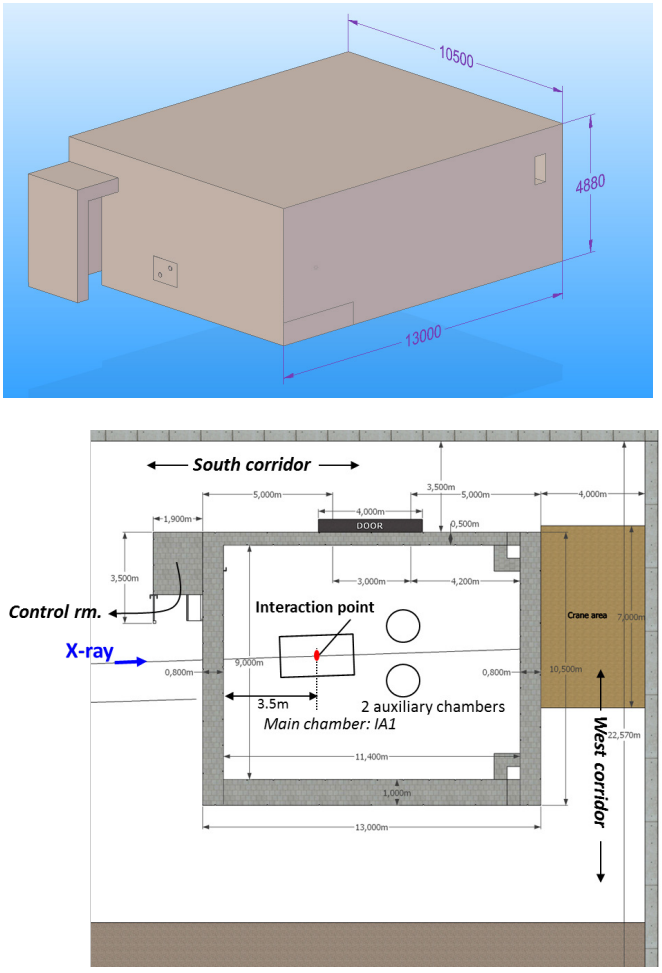

Figure 3-4. *HED experiment hutch (HED-EXP) with 50–100 cm thick heavy concrete walls for radiation shielding in 3D (above) and from a top view (below).*

4 X-ray beam transport

The HED X-ray beam transport at the SASE2 undulator is about 1 km long and is composed of three major sections where X-ray optical components and monitors are installed (Figure 4-1).

The first section starts at the separation of electron and photon beams and ends with the distribution mirror (XTD1: 150–390 m). This section hosts general components, provided by the X-Ray Optics and Beam Transport group (WP73) and the X-Ray Photon Diagnostics group (WP74) to run and tune the FEL beam, as well as the first focusing unit, shared by HED and the two other SASE2 instruments, Materials Imaging and Dynamics (MID) and an optional third instrument (NNN).

In the second section (XTD6: 390–930 m), the beam transport is split into three beamlines in order to steer the three beams to the three instruments in the experiment hall (XHEXP). This section starts with the distribution mirror and ends with the beamline front end, which allows blocking of the beam before entering XHEXP. Besides beam monitors, it hosts important components for HED, such as the split and delay unit (SDU), the monochromator, the second focusing unit, and a pulse picker.

As described in Chapter 3, “HED hutch layout overview”, the third section of the HED beam transport starts in XHEXP and ends with the beam stop in the experiment hutch (HED-EXP). It consists of a transport tube, the X-ray components inside the optics hutch (HED-OPT) and the X-ray components in HED-EXP. HED-OPT hosts important devices for the X-ray beam transport, such as a slit system, beam monitors, the third focusing unit, an attenuator system, and a beam shutter. Optics and experiment hutches are connected via a differential-pumping system. The HED X-ray beam transport ends at the beam stop placed at the west wall of HED-EXP.

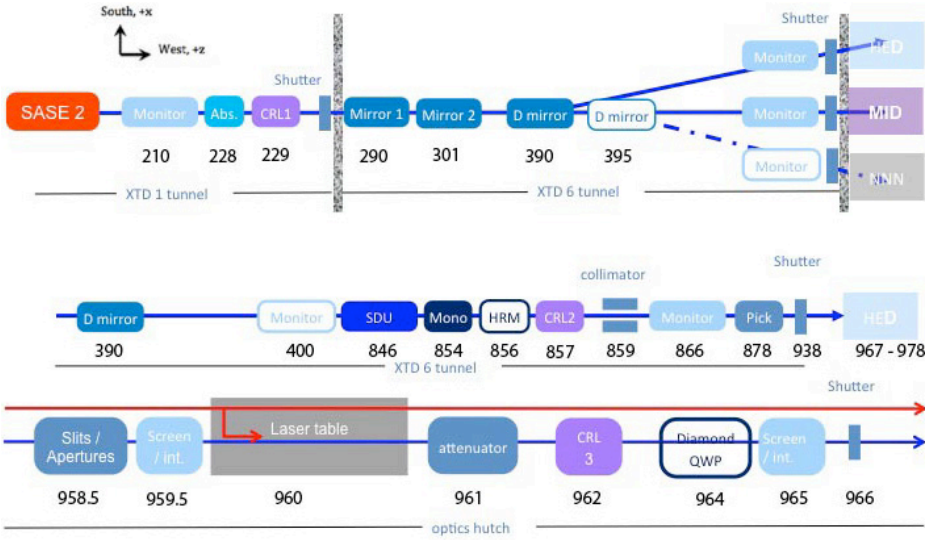

Figure 4-1. *Overview of the layout of the HED instrument. More details on beamline components can be found in the corresponding chapters. The numbers are distances in metres from the source.*

After a summary of the SASE2 X-ray beam properties and an introduction of the requirements for the HED beam delivery, the crucial components for the X-ray transport of the HED instrument are described. Additional information is given in the HED-CDR [1]. As coordinates, we use the *z*-axis parallel to the X-ray beam (positive along the beam) and the *x*- and *y*-coordinates in the plane lateral to the X-ray beam (Figure 4-2). The *x*-axis describes the horizontal direction (positive corresponding to down), and the *y*-axis the vertical direction (positive corresponding to up).

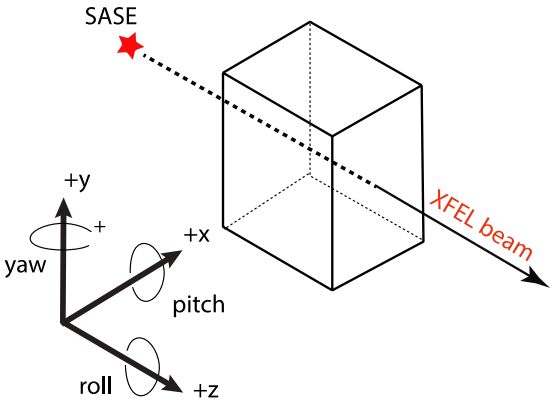

Figure 4-2. *Coordinate system at the SASE2 instruments*

4.1 X-ray beam properties

This section describes the X-ray FEL radiation parameters and self-seeded FEL operation at the HED instrument.

4.1.1 X-ray parameter summary

The HED instrument will be located in a side branch of the X-ray beam transport at the SASE2 undulator of the European XFEL. The electron accelerator has four working points at 8.5, 12, 14, and 17.5 GeV electron energy. An optimization of the overall facility layout has been done for 14 GeV electron energy, but reaching the smallest photon energies at 3–4 keV or the highest photon energies of above 20 keV will require operation of the accelerator at 8.5 or 17.5 GeV, respectively.

Table 4-1 indicates the photon energy dependence on electron energy and SASE2 gap setting. The highest photon energies for which saturation of the FEL radiation can be expected depend on the electron beam emittance, and only approximate values can be given at present.

Table 4-1. *Photon energies at the SASE2 undulator as a function of electron energy and gap setting. The magnet period is 40 mm. Values shown in grey indicate that FEL saturation is not expected.*

Electron energy [GeV]	**Magnetic gap [mm]**						
	10	**12**	**14**	**15**	**20**	**24**	**28**
K parameter	4.2159	3.4851	2.8925	2.6391	1.6940	1.2098	0.8780
8.5	1.74	2.43	3.31	3.83	7.05	9.92	12.40
12	3.46	4.84	6.60	7.64	14.06	19.77	24.71
14.0	4.71	6.59	8.99	10.40	19.14	26.91	33.63
17.5	7.36	10.29	14.05	16.24	29.90	42.04	52.55

The X-ray FEL radiation properties were simulated by E. Schneidmiller and M.V. Yurkov [6] in 2011 and are listed in Table 4-2. The 10.5 GeV working point for the accelerator has, in the meantime, been replaced by two working points at 8.5 and 12 GeV. A particular parameter is the charge of the electron bunch. Less-charged bunches can be more strongly compressed, therefore

providing shorter X-ray bunches. For simulations with bunch charges of 20, 100, 250, 500, and 1000 pC, X-ray pulse durations of 2, 9, 23, 43, and 107 fs, respectively, have been obtained. In general, the higher charge leads to the generation of X-ray pulses with higher pulse energy, narrower bandwidth, and reduced coherence.

Table 4-2. *SASE2 FEL radiation parameters at saturation and for selected photon energy and bunch charge parameters*

Parameter	**Unit**	**Value**											
Photon energy	keV	**3.0****			**5.0**			**7.75**			**12.4**		
Electron energy	GeV	**10.5**			**14**			**14**			**14**		
Bunch charge	nC	**0.02**	**0.25**	**1**	**0.02**	**0.25**	**1**	**0.02**	**0.25**	**1**	**0.02**	**0.25**	**1**
Peak power	GW	51	47	38	55	49	36	46	37	24	35	24	12
Source size (FWHM)	µm	38	49	58	33	41	49	31	39	46	29	37	49
Source divergence (FWHM)	µrad	6.3	5.1	4.3	4.1	3.3	2.8	2.8	2.3	1.9	1.9	1.5	1.3
Spectral bandwidth	1E-3	3.3	2.9	2.4	2.7	2.3	1.9	2.3	1.9	1.4	1.9	1.4	1.0
Photons/pulse	1E11	1.9	25	92	1.1	14	49	0.6	7.0	20.7	0.3	2.8	6.4
Pulse energy	µJ	85	1090	4050	92	1130	3920	76	864	2570	58	549	1260
Peak brilliance	1E33*	0.6	0.7	0.6	1.5	1.6	1.5	2.4	2.4	2.0	3.5	3.2	1.6

* In units of photons/(mm^2 mrad^2 0.1% bandwidth s), ** calculated for 2.75 keV

Parameter	**Unit**	**Value**								
Photon energy	keV	**15.5**			**20.7**			**24.8**		
Electron energy	GeV	**14**			**14**			**17.5**		
Bunch charge	nC	**0.02**	**0.25**	**1**	**0.02**	**0.25**	**1**	**0.02**	**0.25**	**1**
Peak power	GW	29	15	9	21	11	7	25	13	8
Source size (FWHM)	µm	29	35	54	28	39	60	25	36	55
Source divergence (FWHM)	µrad	1.5	1.3	1.0	1.2	1.0	0.8	1.1	0.9	0.7
Spectral bandwidth	1E-3	1.6	1.3	0.8	1.3	0.9	0.6	1.3	0.9	0.6
Photons/pulse	1E11	0.2	1.4	4.0	0.1	0.7	2.1	0.11	0.8	2.2
Pulse energy	µJ	49	347	991	35	248	708	42	302	863
Peak brilliance	1E33*	4.3	2.5	1.6	5.0	2.7	1.5	7.6	4.0	2.3

An important consequence of the source properties and of the long distances in the beam transport is their effect on the X-ray beam sizes. Using as source origin the centre of the third-to-last undulator segment (~ 12 m upstream from the end of the undulator) and using an analytical fit, one obtains for the estimated largest divergence $\Delta\theta_{\max}$ and for the associated beam size $D_{\max}$ [6][7]

$$\Delta\theta_{\max}[\text{rad}] = 1.2 \times 10^{-5}(\lambda\,[\text{nm}])^{0.75}\,,$$
$$D_{\max} = \Delta\theta_{\max} \times z.$$

These are full-width half-maximum (FWHM) values. The 6σ beam size is $D_{\max\_6\sigma} \sim (6/2.35) \times D_{\max}$. The estimated smallest divergence is

$$\Delta\theta_{\min}[\text{rad}] = 0.73 \times 10^{-5}(\lambda[\text{nm}])^{0.85}.$$

This divergence is very close to the diffraction limit. Within this envelope, the divergence depends on bunch charge and electron energy (see Table 4-2). The estimated beam sizes at source distances of 220 m and 800 m are shown in Figure 4-3. These distances correspond to the locations of the first focusing optics and the monochromator.

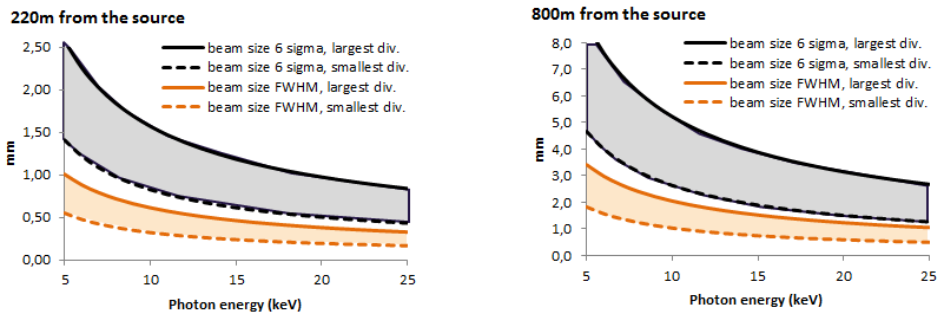

Figure 4-3. *Estimated X-ray beam size without any focusing component at 220 m (left) and 800 m (right) from the source point. Shown are FWHM and 6σ size for the largest divergence and the smallest divergence.*

4.1.2 Self-seeded FEL operation

As mentioned in Section 4.1.1, “X-ray parameter summary”, the description of X-ray FEL radiation properties is valid for operating in self-amplified spontaneous emission (SASE) mode. Following theoretical prediction [8] and experimental demonstration for hard X-ray radiation at the Linac Coherent Light Source (LCLS) at SLAC National Accelerator Laboratory in Menlo Park,

California [9], self-seeded FEL operation mode is now in use at the LCLS and the SPring-8 Angstrom Compact Free Electron Laser in Hyogo, Japan (SACLA). It is applied predominantly for experiments requiring high spectral resolution, e.g. requiring a narrower spectral width than provided by SASE FEL radiation. While the total radiated energy so far is less than in the SASE mode of operation, the spectral flux within the amplification band is much higher. Because the growth of SASE radiation in the amplifier part of the undulator is not negligible, one typically uses monochromators to clean the beam from unwanted spectral components. This monochromator can considerably reduce the flux for soft X-rays, but, for hard X-ray energies, only small absorption factors need to be accounted for. The typical bandwidth for hard X-ray seeded FEL radiation is 5×10^{-5} at 8.3 keV and is perfectly matched by using the Si_{111} monochromator installed in the HED beam transport as described in Section 4.5; “Monochromator”, on page 62.

It is planned to install the instrumentation for self-seeding at the European XFEL following the completion of initial commissioning of the respective SASE undulators with beam. This will occur one to two years after the start of operation, according to current planning. The exact conditions for self-seeded FEL radiation at the European XFEL have yet to be determined. It is expected that a dedicated working group will start on this matter during the year 2014. One proposal is to install a two-stage seeding scheme, allowing the total power on the monochromator crystals to be reduced in the first stage, while ensuring sufficient seed power in the amplifier section behind the second monochromator. This scheme could potentially improve the ratio of seeded power to SASE power in the emitted beam. In order to allow switching between both modes of operation without restricting their respective performance expectations, it was recently decided to prolong the undulator section by ~ 12 m, allowing the installation of two chicanes for the two-stage seeding planned for the European XFEL. Although we do not explicitly refer to the FEL parameters for self-seeded operation, the current layout is designed to maximize the benefit of this mode. In particular, the imaging and scattering experiments will benefit from the reduced bandwidth and higher brilliance.

4.2 X-ray requirements summary

Detailed experimental requirements have been collected for a set of key experiments to be performed at the HED instrument (see Chapter 2, “Introduction”). From the X-ray parameter point of view, photon energies between 5 and 25 keV should be provided at variable spot sizes. The required energy resolution ranges from natural (10^{-3}) to 10^{-6} (Table 4-3). Figure 4-4 shows an overview of the required beam sizes and energy ranges. From this, it becomes clear that the requirements are extremely diverse and extend over the entire energy range. The concept of the HED X-ray beam transport has been designed to ensure that the key experiments can be performed.

Table 4-3. *Requirements for X-ray parameters for experiments at the HED instrument (t.b.i.= to be investigated)*

Experiment	Photon energy [keV]	Bandwidth	SDU	Focal spot size [µm]
Magnetic scattering	16	10^{-2}–10^{-3}	No	200
Magnetic scattering	8	10^{-4}	No	1
Excited states, IXS	5–15	3 x 10^{-3}	No	50
Excited states, IXS	5–15	2 x 10^{-4}	No	50
Dynamic compression	10–25	10^{-3} (10^{-4})	No	50–100
SAXS	4–20	10^{-2}–10^{-3}	t.b.i.	5
Dynamic DAC	24	10^{-3}–10^{-4}	t.b.i.	5
Double DAC	25	10^{-3}	t.b.i.	1
WDM with IXS/XAS	9	Small	Yes	20
hr-IXS	7.919, 9.899, 13.858	Si_{444}, 6 x 10^{-6}	No	10
Birefrigence	12.914	As low as possible	No	< 1
Transient SAXS/WAXS	8–25	< 10^{-3}	No	10

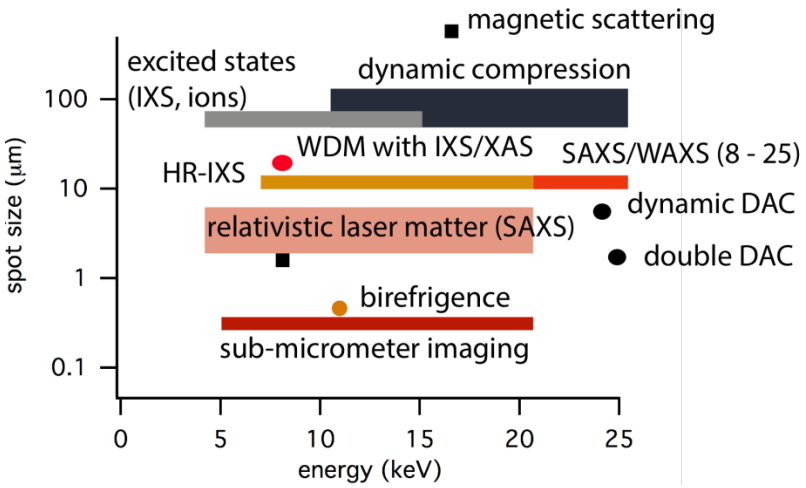

Figure 4-4. *Overview of spot sizes and energies required for experiments at HED*

4.3 Compound refractive lenses

This section describes the focusing concept, compound refractive lenses (CRLs), wavefront simulation, single-shot damage estimates and heat simulation, CRL mechanics, and nanofocusing setup of the HED instrument.

4.3.1 Summary of focusing concept

The focusing concept of the HED instrument is based entirely on the use of CRLs. The fundamental element of the CRL system will be the beryllium (Be) lens. Each lens is formed by stamping a Be plate to impart symmetrical parabolas with the geometry depicted in Figure 4-5. Multiple lenses will be stacked to achieve the desired focal length.

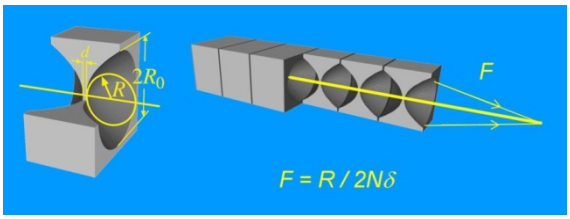

Figure 4-5. *Schematic of focusing with CRLs*

Besides the important point that those lenses focus the beam on axis, they have the advantages of easy alignment and handling. A relatively large variation of focus sizes is required for HED at the sample locations, classified

into large, medium, and tight focusing. To reach these spot sizes under the condition that the focus is located at the sample, three different lens positions were proposed in the HED CDR. This scheme has been further refined in the past year and is discussed in Section 4.3.2, “CRL1, 2, 3 lens configurations, transmissions”, on page 40. The envisaged positions for the focusing units and the focusing schemes are shown in Figure 4-6. The three lens units have different functionalities, as explained in the following paragraphs.

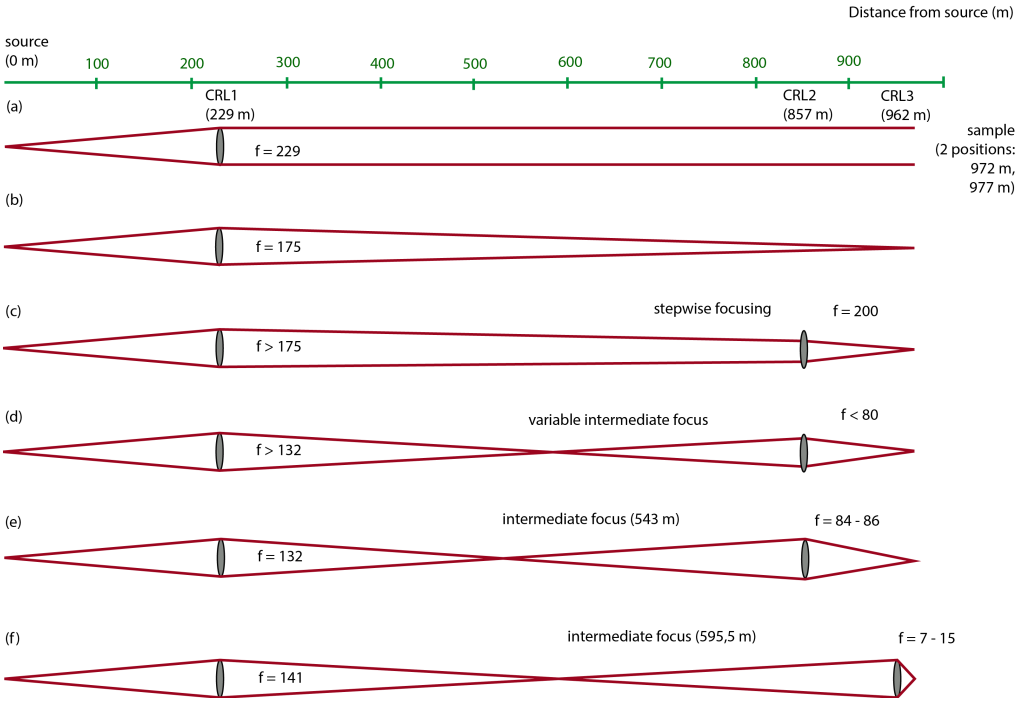

Figure 4-6. *Schematic layout of different focusing and collimation schemes planned for HED. Schemes (a) to (f) are explained in the text.*

CRL1 is positioned as close to the source as possible, i.e. at 229 m. This lens system has the functionality to either (a) collimate the beam, (b) directly focus the beam to the sample position, (c) pre-focus the beam in a stepwise focusing scenario, or (d–f) create an intermediate focus.

The spot sizes obtained with the scheme shown in Figure 4-6(a) range from 970 to 290 µm (FWHM) for photon energies of 5 to 25 keV, respectively. The X-ray beam collimation stops the beam from further expanding with increasing distance to the source point. For the collimated beam, the distribution mirror with a fixed acceptance of 1 mm allows for the reflection of the FWHM of the photon beam for photon energies $E > 5$ keV and the

reflection of 6σ of the photon beam for photon energies E > 17 keV. For smaller photon energies, the size of the distribution mirror will clip the beam.

The spot sizes obtained by direct focusing with CRL1, scheme (b), range from 260 to 160 µm (FWHM) for photon energies of 5 to 25 keV, respectively (Table 4-4). As explained in the CDR, the minimum spot size is, in all cases, limited by diffraction and not by demagnification of the source. The Rayleigh length for 100 µm spot sizes in the energy range of 5–25 keV corresponds to more than 100 m, thus covering the total length of HED-EXP.

Table 4-4. *Expected X-ray beam sizes at the sample position for various focusing schemes and three selected photon energies. Calculations have been performed for 1 nC electron bunch charge.*

CRL geometry X-ray energy	**Focal spot FWHM [µm]**	**Transmittance**	**Intensity [W/cm^2]**
(f) 5 keV	2.6	0.55	~ 1E17
15 keV	1.3	0.92	2E17
25 keV	1.1	0.93	5E17
(e) 5 keV	40	0.92	1E14
15 keV	26	0.99	1E15
25 keV	24	0.99	1E15
(b) 5 keV	260	0.97	4E12
15 keV	190	0.99	2E13
25 keV	160	0.99	5E13

In scheme (c), CRL1 will be used to pre-focus the X-ray beam such that the beam size at the positions of CRL2 or CRL3 will be reduced, thereby affecting the diffraction-limited beam size on the sample. This stepwise focusing scheme is especially important as it provides medium beam sizes of 50–100 µm, a size range that was asked for by the HED-ART members during the CDR review and was still not developed at the time of the CDR.

The schemes (d–f) create an intermediate focus to enable maximum transmission of the entire beam transport. Using CRL2 or CRL3, this intermediate focus will then be refocused on the sample location. This concept will be used, in particular, for small photon energy applications. Using the intermediate focus scheme, 6σ can be transmitted through the X-ray beam transport and various focusing optics for photon energies above 5 keV. Likewise, the photon flux on the sample can be maximized. Scheme (d) also generates different diffraction-limited spot sizes and can be used to provide beam sizes on the order of 50–100 µm at the sample position.

CRL2 has the major functionality to provide medium beam sizes in the range of 40 to 20 µm for 5 to 25 keV, respectively. This can be achieved by diffraction-limited focusing of an X-ray beam that has either been collimated (Figure 4-6(b)) or focused to an intermediate focus (Figure 4-6(d, e)) by CRL1. In addition, lenses in CRL2 can be used to focus the beam to larger beam sizes in the range of 50 to 100 µm either in a stepwise focusing scheme (Figure 4-6(c)) or by a shift of the intermediate focus position (Figure 4-6(d)). Again, the depth of focus on the sample, on the order of 5–25 m, will be large (Figure 4-7). Since CRL2 increases the divergence of the X-ray beam, in particular for scheme (a) of collimated X-ray beam, this CRL unit is positioned downstream of devices that require parallel beam, such as the split and delay unit (SDU) or the four-bounce monochromator.

CRL3 is used to provide smaller spot sizes at the sample location. It is positioned in the HED optics hutch at 962 m from the source. For the moment, two different interaction points are planned in the experiment hutch. The main experiment chamber (IA1) is planned to be 972.5 m from the source, and the IA2 zone is planned to be 977 m from the source. The distance from CRL3 to IA1 is 10.5 m and the spot size on the sample, which can be achieved in a scenario when the ideal lens configuration is available for all energies, ranges between 2.6 and 1 µm for photon energies between 5 and 25 keV, respectively (see Table 4-4). The depth of focus for these spot sizes is around 20 mm for 5 keV at a spot size of 2.6 µm. As shown in Section 4.3.2, “CRL1, 2, 3 lens configurations, transmissions”, with a reasonable number of lenses in CRL3, it is impossible to match the position of the focus with the sample position for each photon energy in the given photon

energy range. To minimize this difficulty, CRL3 can be moved ± 0.25 m along the X-ray beam axis, thereby varying the distance to focus. Larger translations will be difficult to realize due to space constraints in the optics hutch and for mechanical reasons (vacuum).

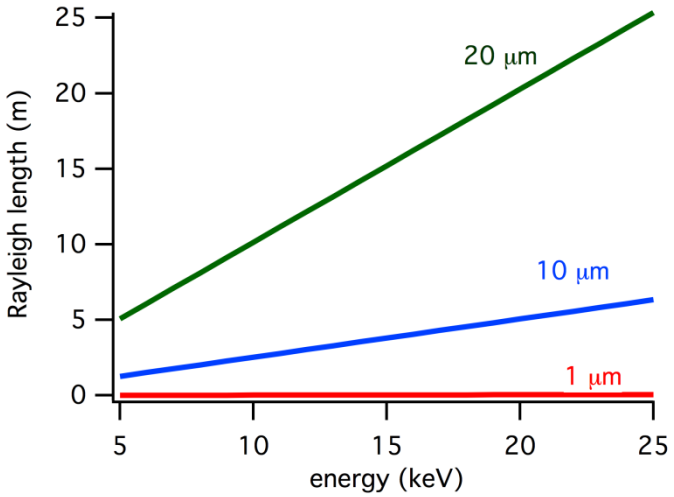

Figure 4-7. *Rayleigh length for different beam sizes. These scenarios will occur in cases when CRL2 and CRL3 are used to focus the beam.*

Focusing to the IA2 zone with foci on the order of a few micrometres will require a significantly different focal length for the CRLs when compared to the requirements for IA1. Nevertheless, focusing to the sample position can be achieved for photon energies above 6 keV using the lens set that was optimized for IA1.

4.3.2 CRL1, 2, 3 lens configurations, transmissions

Focusing using CRLs is chromatic, and focusing power depends strongly on energy. This has to be considered for the planning of lens configurations at the three different positions. The lenses at HED are planned to be made of Be for reasons of high transmittance, single-shot threshold, high thermal conductivity, and availability. The dependence of the refraction index of Be on photon energy is given in Table 4-5.

Another issue is that part of the X-ray beam is absorbed in the lenses. For this reason, as few lenses as possible should be used for focusing to guarantee maximum flux. Be X-ray lenses provided by RXOPTIC in Jülich, Germany, have a material thickness of 0.7 mm for radii > 2.5 mm and of

1 mm for radii < 2.0 mm. For CRL1, the lenses can be selected in a way that transmission is above 90% for the energy range of 5–25 keV. For the photon energy range of 3–5 keV, special focusing schemes using Be CRLs have to be applied, which are not further discussed in this report.

4.3.2.1 CRL1 lens unit at 229 m from the source

The relevant parameter to focus the X-ray beam by CRLs is the focusing power $\frac{1}{2\delta(E)f} = \sum_i \frac{N_i}{R_i}$ (with $\delta(E)$: refractive index of Be; *f*: focal length; *N*: number of lenses; *R*: radius of lens). Some numbers for the relevant *f* for HED for CRL1 and different photon energies are given in Table 4-5. Very weakly refracting lenses with large radii are required to collimate or focus the beam using CRL1 at small photon energies.

The Be lenses available by RXOPTICS have radii of 5.8 mm, 5.0 mm, 4.0 mm, 3.5 mm, 2.0 mm, 1.0 mm, and 0.5 mm. Based on these lenses, a suggestion has been made for the lens configuration in the CRL1 lens holder that fulfils the requirements for the HED and MID instruments, as those two experiments share the CRL1 unit. MID also has different focusing schemes and requires focal lengths of 229 m, 196 m, 177.4 m, or 158.9 m. With the energy range to be covered by MID (5–25 keV), the focusing power should be adjustable in the range of 0.155 to 5.763 mm^{-1}. For HED, the different focal length for CRL1 to realize all envisaged collimation and focusing scenarios varies between 0.152 and 6.19 mm^{-1} (Table 4-5). The CRL unit will provide 10 lens positions, which can be moved in or out of the X-ray beam (see Section 4.3.5, “CRL mechanics” on page 54). The proposed configuration of lenses and the resulting focusing power $\sum_i \frac{N_i}{R_i}$ is shown in Table 4-6.

With this configuration, a total of 23 lenses is needed. The maximum focusing power of 6.19 mm^{-1} can be met by putting one 5.0 mm lens (0.2 mm^{-1}), seven 2.0 mm lenses (3.5 mm^{-1}), and ten 4.0 mm lenses (2.5 mm^{-1}). However, the large variations and the small scaling in Table 4-5 show that it is difficult to meet the ideal requirements for every energy step, especially for the low energies. This problem cannot be ruled out by adding more actuators to the CRL1 holder alone, but would rather require differently shaped lenses. Nevertheless, the proposed configurations enable ideal focusing conditions

for about every 300 eV in the energy range as indicated in Figure 4-8. Since the Rayleigh length is always large in this configuration, it is expected that, even for the intermediate photon energies, near-ideal focusing conditions can be established.

Table 4-5. *Required* $\frac{1}{2\delta(E)f} = \sum_i \frac{N_i}{R_i}$ *[mm^{-1}] for collimation, direct focusing, and intermediate focusing to CRL2 (IF1) and to CRL3 (IF2) by CRL1 at 229 m from the source*

		Collimation	**Direct focusing**	**IF1**	**IF2**
E [keV]	$\delta(E)$	*f* = 229	*f* = 175	*f* = 132	*f* = 140
5	1.43E-05	0.152	0.200	0.264	0.248
6	9.95E-06	0.220	0.287	0.381	0.357
7	7.31E-06	0.299	0.391	0.518	0.485
8	5.59E-06	0.390	0.511	0.677	0.634
9	4.42E-06	0.494	0.646	0.857	0.802
10	3.58E-06	0.610	0.798	1.058	0.990
11	2.96E-06	0.738	0.966	1.280	1.198
12	2.49E-06	0.878	1.149	1.523	1.426
13	2.12E-06	1.031	1.349	1.788	1.674
14	1.83E-06	1.195	1.564	2.074	1.941
15	1.59E-06	1.372	1.796	2.380	2.229
16	1.40E-06	1.561	2.043	2.708	2.536
17	1.24E-06	1.762	2.306	3.058	2.862
18	1.11E-06	1.976	2.586	3.428	3.209
19	9.92E-07	2.202	2.881	3.819	3.576
20	8.95E-07	2.439	3.192	4.232	3.962
21	8.12E-07	2.689	3.519	4.666	4.368
22	7.40E-07	2.952	3.862	5.121	4.794
23	6.77E-07	3.226	4.222	5.597	5.239
24	6.22E-07	3.513	4.597	6.094	5.705
25	5.73E-07	3.811	4.988	6.612	6.190

Table 4-6. *Proposed filling of eight lens cassettes in CRL1. For each slot, the number of lenses and the respective lens radii (in mm) are indicated.*

Actuator	1	2	3	4	5	6	7	8
Lenses	1 x 5.8	1 x 5.0	1 x 4.0	1 x 3.5	2 x 5.8	3 x 4.0	7 x 4.0	7 x 2.0
***N/R* [mm^{-1}]**	0.172	0.2	0.25	0.286	0.345	0.75	1.75	3.5

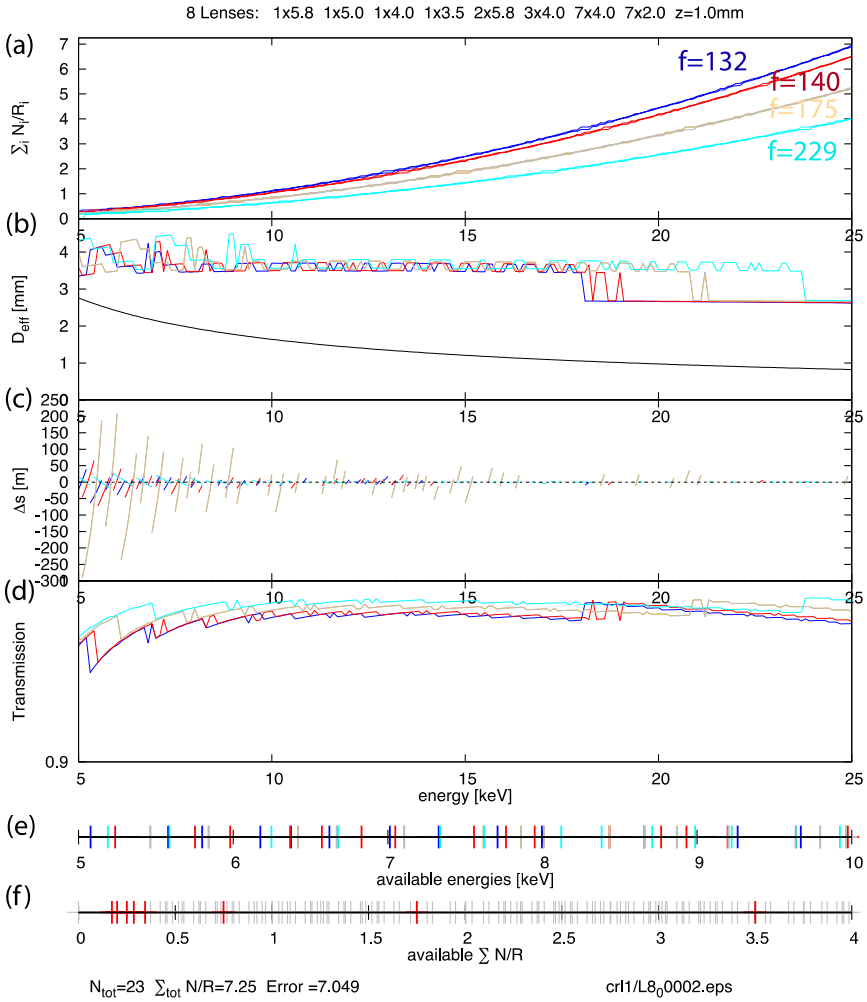

Figure 4-8. *Characteristics of the proposed lens stacks for CRL1. (a) Available and required focusing power for the different collimation and focusing scenarios. (b) Effective lens aperture. The black line indicates the effective aperture. (c) Difference between focal spot and sample position. If zero, ideal focusing conditions are met. (d) X-ray transmission for the respective lens configuration. (e) Ideal overlap of focus and sample position for the energy range 5–10 keV. For higher energies, this overlap becomes easier. (f) N/R for the individual lens configurations inside one lens holder. The calculations were performed with the software "crl" provided by Th. Roth of the MID group.*

4.3.2.2 CRL2 lens unit at 857 m

The second lens holder will be positioned at 857 m from the source and has the function of focusing the collimated, intermediately focused, or pre-focused beam at the two defined sample positions. The required *N*/*R* values for the envisaged photon energy range of 5–25 keV and the intermediately focusing schemes (d) and (e) for two different sample positions are shown in Table 4-7.

Table 4-7. *Required* $\frac{1}{2\delta(E)f} = \sum_i \frac{N_i}{R_i}$ *[mm^{-1}] for focusing to sample positions IA1 and IA2 using CRL2 in focusing schemes (e) (f = 86, f = 84) and (d) (f = 76, f = 78)*

***E* [keV]**	***δ*(*E*)**	***f* = 86**	***f* = 84**	***f* = 76**	***f* = 78**
5	1.432E-05	0.406	0.416	0.459	0.459
6	9.945E-06	0.585	0.599	0.662	0.662
7	7.307E-06	0.796	0.815	0.900	0.900
8	5.594E-06	1.039	1.064	1.176	1.176
9	4.420E-06	1.315	1.347	1.488	1.488
10	3.580E-06	1.624	1.663	1.838	1.838
11	2.959E-06	1.965	2.012	2.223	2.223
12	2.486E-06	2.338	2.394	2.646	2.646
13	2.119E-06	2.744	2.810	3.105	3.105
14	1.827E-06	3.183	3.259	3.602	3.602
15	1.591E-06	3.654	3.741	4.134	4.134
16	1.399E-06	4.157	4.256	4.704	4.704
17	1.239E-06	4.693	4.805	5.310	5.310
18	1.105E-06	5.261	5.387	5.954	5.954
19	9.918E-07	5.862	6.002	6.634	6.634
20	8.951E-07	6.495	6.650	7.350	7.350
21	8.119E-07	7.161	7.332	8.104	8.104
22	7.397E-07	7.860	8.047	8.894	8.894
23	6.768E-07	8.590	8.795	9.721	9.721
24	6.216E-07	9.354	9.576	10.584	10.584
25	5.728E-07	10.149	10.391	11.485	11.485

Table 4-8. *Proposed filling of 10 lens cassettes in CRL2. For each slot, the number of lenses and the respective lens radii (in mm) are indicated.*

Actuator	1	2	3	4	5	6	7	8	9	10
Lens	1 x 5.8	1 x 5.0	1 x 4.0	1 x 3.5	2 x 5.8	4 x 5.8	7 x 5.8	10 x 4.0	10 x 3.5	8 x 2.0
N/R [mm-1]	0.172	0.2	0.25	0.286	0.345	0.69	1.207	2.5	2.857	4

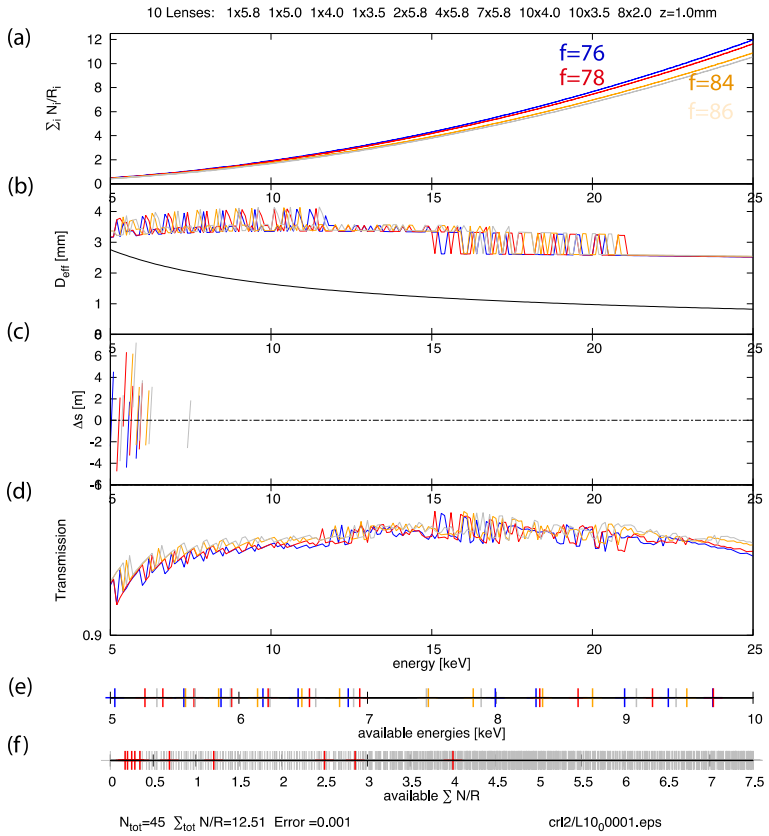

Figure 4-9. *Characteristics of the proposed lens stacks for CRL2. (a) Available and required focusing power for the different focusing scenarios. (b) Effective lens aperture. (c) Difference between focal spot and sample position. If zero, ideal focusing conditions are met. (d) X-ray transmission for the respective lens configuration. (e) Ideal overlap of focus and sample position for the energy range of 5-10 keV. For higher energies, this overlap becomes easier. (f) N/R for the individual lens configurations inside one lens holder. The calculations were performed with the software "crl" provided by Th. Roth of the MID group.*

Figure 4-9 shows the focusing capabilities of the chosen lens configuration in CRL2 for the entire energy range of 5–25 keV. The achieved focal spots are diffraction-limited and depend on the illuminated area on CRL2. For the low energies, focused beam and sample position overlap roughly every half keV.

These results hold true for the overlap of the minimum beam size. Due to the restricted number of lens radii, this result could only be improved if additional lens radii were made available. However, it has to be kept in mind that the depth of focus for 5 keV for a 20 µm spot size is approximately 5 m. As illustrated in Figure 4-10, for *f* = 78, this condition will be met for almost every energy. Transmission is always above 90%, similar to what was found for CRL1. This means that the combined transmission is 81% or better, even for the smallest photon energies.

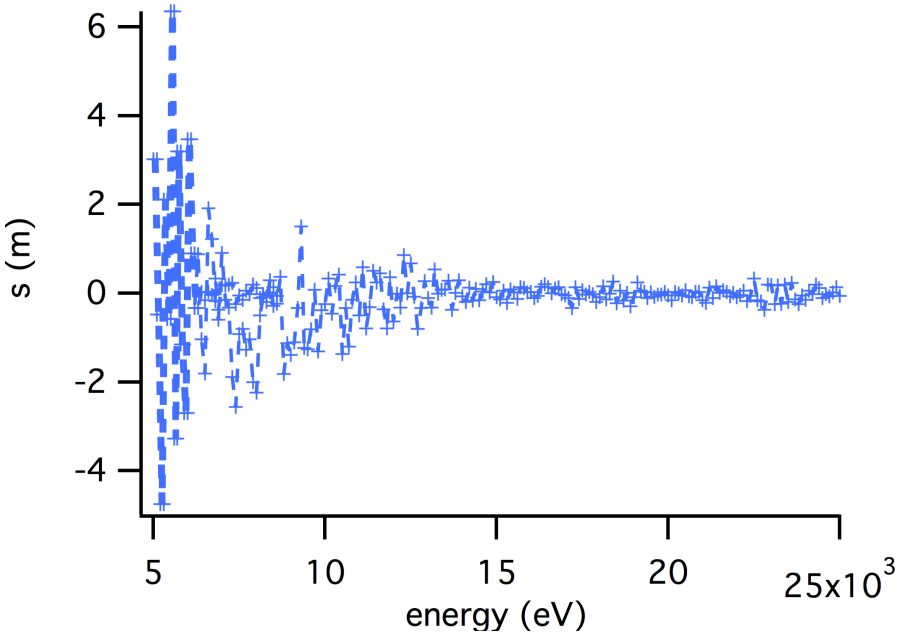

Figure 4-10. *Difference between focal spot and sample position for the configuration with 10 lens packages and f = 78. If zero, ideal focusing conditions are met; if between + 2.5 and - 2.5 m at 5 keV, the conditions fall within the Rayleigh length for a 20 µm sized spot.*

Larger spot sizes can be achieved by changing the aperture of CRL2, i.e. by a decrease of the size of the illuminated area of CRL2. This can be achieved by different degrees of pre-focusing of the beam or by a shift of the intermediate focus position using CRL1. For 5 keV and a 100 µm large spot at the sample position, the aperture of CRL2 has to be ~ 500 µm, while to achieve a 15 µm spot size, an aperture of 750 µm is required. A spot size of 50 µm at the sample position can be achieved with the stepwise focusing scheme (c). Wavefront simulations have been performed to test this concept. The simulations confirm that this scheme is feasible: using a 5 mm radius

lens at CRL1 and a 5.8 mm lens in CRL2 will produce a spot size of 60 µm at 5 keV (Figure 4-11). To enable a similar spot size of 54 µm at 15 keV, seven 4 mm radius lenses are needed in CRL1 and nine 5.8 mm radius lenses in CRL2.

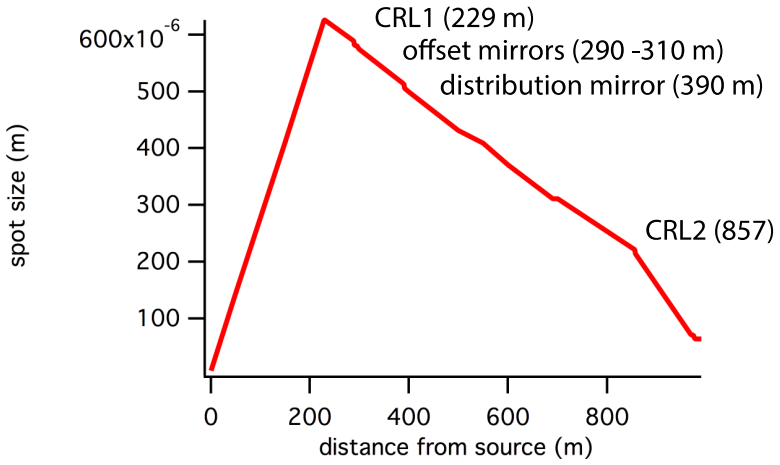

Figure 4-11. *Development of the X-ray beam size (FWHM) along the transport system from the source to a few metres behind the HED instrument (990 m) in the pre-focusing scheme using CRL1 and CRL2 at a photon energy of 5 keV*

4.3.2.3 CRL3 lens unit at 962 m

CRL3 is at 962 m from the source and has the functionality to focus the collimated or intermediately focused beam to the two sample positions IA1 and IA2. Due to the small distance, the differences of *N*/*R* values for the two sample positions are very large. The required *N*/R values for the envisaged energy range of 5–25 keV for two different sample positions are shown in Table 4-9.

To focus the X-ray beam at photon energies above 20 keV, for the sample position IA1, *N*/*R* > 60 is required, while for sample position IA2, *N*/*R* = 60 is sufficient to focus up to 25 keV. On the soft X-ray side, IA2 requires a smaller *N*/*R* leading to limited choices for photon energies smaller than 6 keV (see Table 4-9). Table 4-10 shows a lens configuration with a maximum *N*/*R* value of nearly 80. This will allow focusing of X-rays in the energy range of 5-22 keV at IA1 and of 6–25 keV at IA2.

Table 4-9. *Required* $\frac{1}{2\delta(E)f} = \sum_i \frac{N_i}{R_i}$ *[mm^{-1}] for focusing with the CRL3 unit to sample positions IA1 (f = 9) and IA2 (f = 15). Numbers in grey indicate presently not included focusing scenarios.*

E **[keV]**	***δ(E)***	***f*** **= 9**	***f*** **= 15**
5	1.43212E-05	3.879	2.328
6	9.94527E-06	5.586	3.352
7	7.30673E-06	7.603	4.562
8	5.59421E-06	9.931	5.959
9	4.42012E-06	12.569	7.541
10	3.5803E-06	15.517	9.310
11	2.95892E-06	18.776	11.265
12	2.48632E-06	22.345	13.407
13	2.11852E-06	26.224	15.734
14	1.82668E-06	30.413	18.248
15	1.59124E-06	34.913	20.948
16	1.39855E-06	39.724	23.834
17	1.23886E-06	44.844	26.907
18	1.10503E-06	50.275	30.165
19	9.91772E-07	56.016	33.610
20	8.95074E-07	62.068	37.241
21	8.11859E-07	68.430	41.058
22	7.39731E-07	75.102	45.061
23	6.76805E-07	82.085	49.251
24	6.21579E-07	89.378	53.627
25	5.72848E-07	96.981	58.189

Table 4-10. *Proposed filling of eight lens cassettes in CRL3. For each slot, the number of lenses and the respective lens radii (in mm) are indicated.*

Actuator	1	2	3	4	5	6	7	8
Lens	3 x 5.8	7 x 5.8	10 x 4.0	10 x 2.0	10 x 1.0	10 x 0.5	10 x 0.5	10 x 0.5
N/R **[mm^{-1}]**	0.517	1.207	2.5	5.0	10	20	20	20

The absorption of X-rays in the lenses leads to a reduction of the effective lens aperture as described in [10]. This effect has been implemented in the software tool “crl”, which was used to calculate the lens characteristics. More information on the used formulae can be found in “Technical Design Report: Scientific Instrument Materials Imaging and Dynamics” (MID TDR) [11]. The relation between effective aperture of the lens and beam size at the entrance of CRL3 is shown in Figure 4-12. With the large number of lenses, the effective aperture of the CRL starts to limit the spot size on the sample. For the previously discussed cases of CRL1 and two lenses, this effective aperture was always larger than the beam size. The number of lenses also has an effect on the transmission as can be observed from (d). It is above 90% for energies above 10 keV. Figure 4-12 shows which energies are realized with the proposed setup: ideal conditions can be expected for every 300 eV. The spot size is diffraction-limited and is expected to be 2.6 µm for 5 keV and 1.1 µm for 25 keV. The depth of focus at 5 keV is in the range of 11 mm. A focus at the sample position IA1 at 5 keV can be realized with 10 lenses with 4.0 mm radius plus eight lenses with 5.8 mm radius. This is a nearly perfect match in *N/R* value, but the resulting CRL-to-sample distance (*L*2) varies, depending on whether the beam is collimated by CRL1 or focused to an intermediate focus. In the first case, *L*2 equals 10.362 m. In the second case, *L*2 equals 10.217 m. Both values do not overlap with 10.5 m, which can be compensated for by moving CRL3 along the X-ray beam axis to overlap the sample and the X-ray focus.

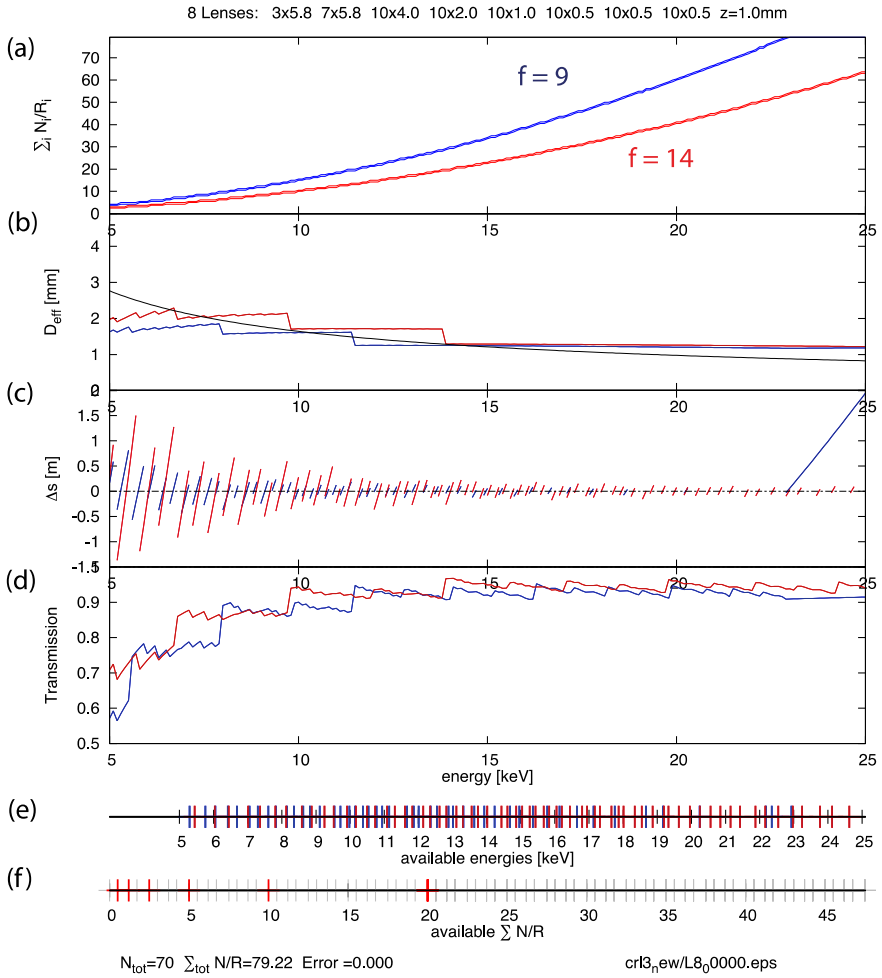

Figure 4-12. *Characteristics of the proposed lens stacks for CRL3. (a) Available and required focusing power for the different collimation and focusing scenarios. (b) Effective lens aperture. (c) Difference between focal spot and sample position. If zero, ideal focusing conditions are met. (d) X-ray transmission for the respective lens configuration. (e) Ideal overlap of focus and sample position for the energy range of 5–25 keV. (f) N/R for the individual lens configurations inside one lens holder. The calculations were performed with the software tool "crl" provided by Th. Roth of the MID group.*

4.3.3 Wavefront simulation

Wavefront simulations have been performed for selected configurations. The simulations allow all optics in the beam transport to be combined and can thus be used to estimate the properties of the X-ray spot resulting from propagation through the beam transport system. The calculations are based on a Fourier optics approach implemented in the Synchrotron Radiation

Workshop (SRW) library [12] with further extensions for specific X-ray FEL applications [13].

Several focusing scenarios have been simulated for 5 keV, and results for the beam size are shown in Figure 4-13. From the steepness of the curves at the sample location (972.5 m), one can obtain the effect of the different Rayleigh lengths for the different focusing scenarios. The simulation results for the corresponding beam profiles at the sample position as shown in Figure 4-14, Figure 4-15, and Figure 4-16. Figure 4-15, Figure 4-17, and Figure 4-18 show the beam profile results for the stepwise focusing scheme at 5, 6, and 15 keV, respectively, and confirm that focusing to beam spot sizes on the order of 50 µm should be possible in this scheme. Smallest spot sizes can be achieved with intermediate focusing and a large illumination of CRL2 (750 µm gives 15 µm). Using a lens with a bigger diameter at CRL1, the intermediate focusing point can be shifted downstream (blue curve in Figure 4-13). This results in a smaller illumination of CRL2 (500 µm) and in a larger spot size at the sample position (on the order of 100 µm).

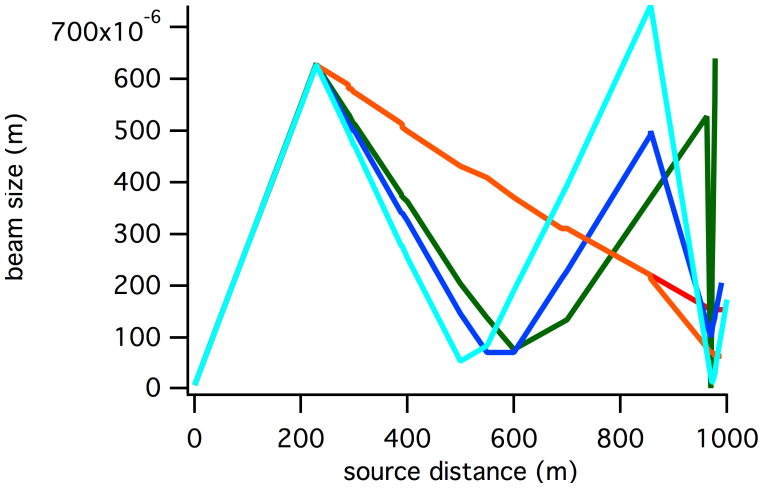

Figure 4-13. *Evolution of beam size with distance from the source for a photon energy of 5 keV. Red: Focused with CRL1. Orange: Stepwise focusing scheme with CRL1 and CRL2. Blue: Intermediate focusing with CRL1 and CRL2 to medium beam size. Turquoise: Intermediate focusing with CRL1 and CRL2 to minimum beam size for this configuration. Green: Intermediate focusing scheme with CRL1 and CRL3.*

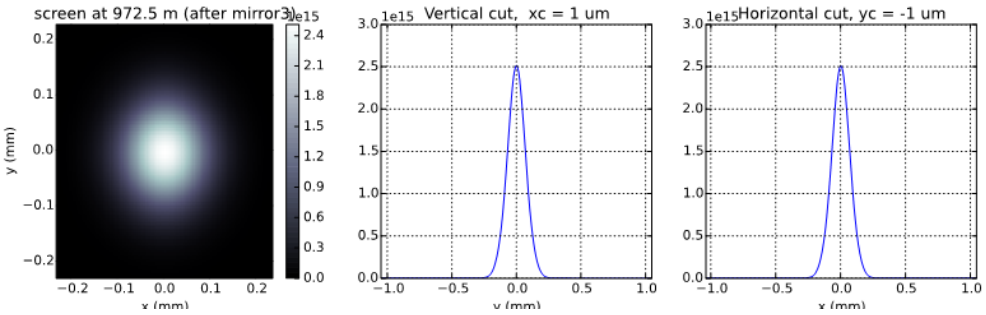

Figure 4-14. *Beam profile (FWHM) at 972.5 m from the source for focusing with CRL1 at 5 keV. The resulting spot size (FWHM) is 160 µm.*

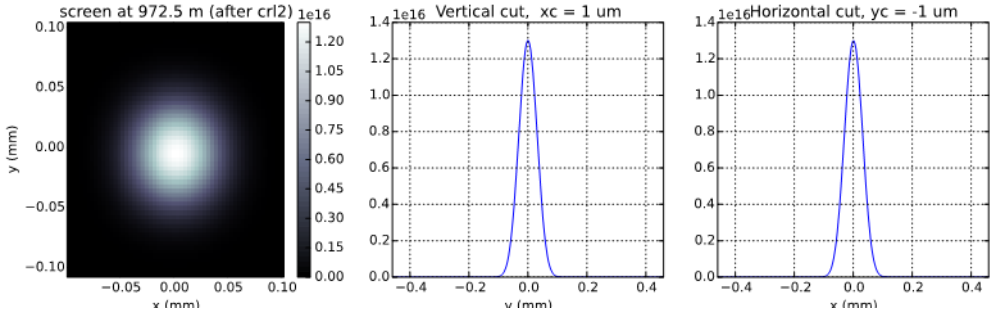

Figure 4-15. *Beam profile (FWHM) at 972.5 m from the source for stepwise focusing with CRL1 and CRL2 at 5 keV. The resulting spot size (FWHM) is 50 µm.*

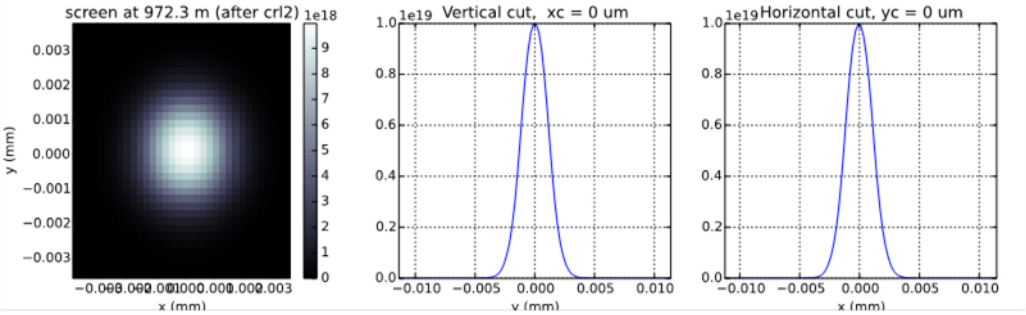

Figure 4-16. *Beam profile (FWHM) at 972.3 m from the source obtained with the intermediate focusing scheme with CRL1 and CRL3 at 5 keV. The resulting spot size (FWHM) is 2 µm.*

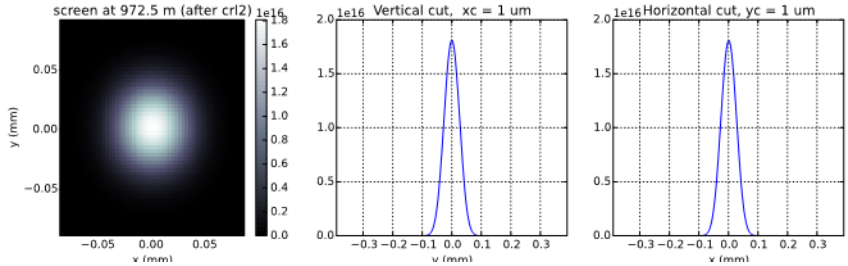

Figure 4-17. *Beam profile (FWHM) at 972.5 m from the source for stepwise focusing with CRL1 and CRL2 at 6 keV. The resulting spot size (FWHM) is 54 µm.*

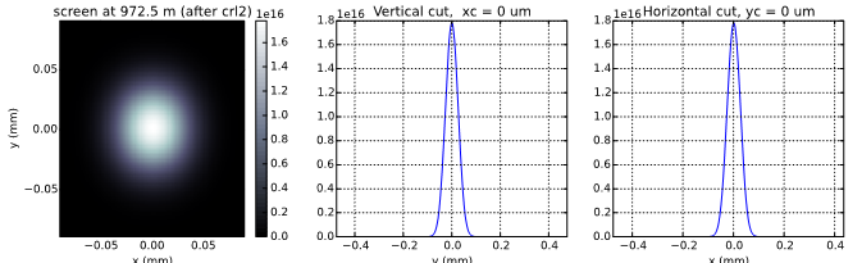

Figure 4-18. *Beam profile (FWHM) at 972.5 m from the source for stepwise focusing with CRL1 and CRL2 at 15 keV. The resulting spot size (FWHM) is 54 µm.*

4.3.4 Single-shot damage estimates and heat dissipation

Any material exposed to the intense FEL radiation will absorb energy. Too strong absorption in a single pulse will lead to damage of the lenses. To avoid such damage, the absorption per atom should stay clearly below a value of ~ 1 eV/atom. This limits the fluence of the beam (J/cm^2), which depends on the beam size. Figure 4-19 shows the minimum beam sizes of the X-ray beam as a function of photon energy with the requirement to limit absorption to less than 0.1 eV/atom.

Furthermore, during the 600 µs X-ray pulse trains, heat transport is strongly limited, and therefore the absorption of X-ray energy can lead to heating of the lenses and subsequent material distortion or even melting (see HED CDR). The X-ray spot size on the Be lenses affects the heat transport. We estimate that, for a beamsize of 70 x 70 µm^2, a photon energy of 5 keV, and 10^5 photons per pulse, a temperature jump of 30 K occurs. For Be, the absolute temperature should stay below 600 K (δT ~ 300 K), thus limiting the maximum number of X-ray pulses per 600 µs train. More details can be found in the MID TDR [11].

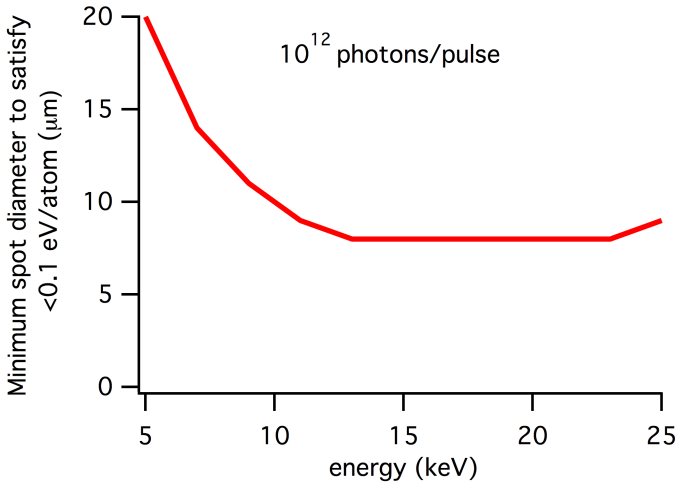

Figure 4-19. *Minimum X-ray beam size to maintain < 0.1 eV/atom (10^{12} photons/pulse)*

4.3.5 CRL mechanics

As introduced in Section 4.3.1, “Summary of focusing concept”, three CRL units are required for the HED X-ray beam transport: two inside the tunnels and one in HED-OPT. All three need to work under ultrahigh-vacuum (UHV) conditions. The CRL units will consist of a mechanical system to position and align the 10 lens holders (Figure 4-20). Each lens holder has actuators to move the lens stack in or out of the X-ray beam and to align it in the *x*- and *y*-direction. The central axis of the CRL system corresponds to the optical axis of the Be lenses when in the active position. Remote control of actuators, reading of encoders, and reading of temperature sensors will all be handled through the beam transport and instrument control systems. The Be lens cassette is contained within a removable cradle. This cradle will hold the lens cassette permitting inspection, metrology, and inter-lens alignment away from the CRL system and beamline. Each lens cradle will have a boron carbide (B_4C) aperture integrated into the upstream face with a thickness of 10 mm, an aperture diameter of 4 mm centred on the lens optical axis, and an overall minimum outer extent sufficient to cover the entire upstream face of the cradle silhouette.

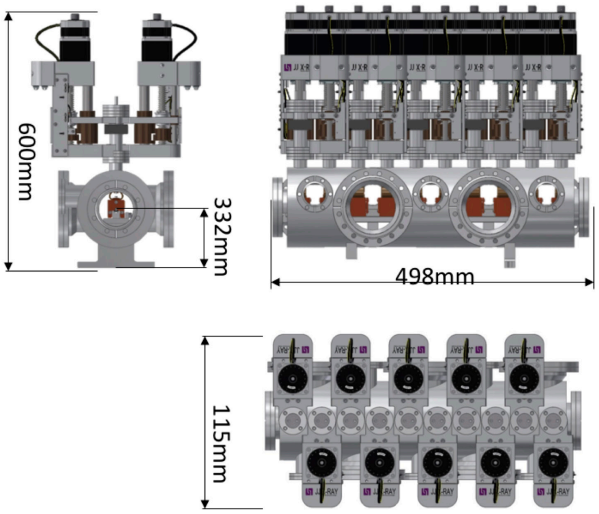

Figure 4-20. *Physical dimensions of the CRL holder with 10 lens cassettes. The technical drawing was provided by JJ X-Ray A/S in Lyngby, Denmark.*

The lens cradle interfaces with the cooling water circuit such that the heat transfer from the Be lenses to the water circuit is sufficient to absorb 20 W per system, with the potential for the entire absorbed power to be deposited in a single arm. This assumes continuous operation in Beam Mode 3 as described in Section A.1, “Operation modes at the European XFEL”, on page 183, or a lower-intensity beam configuration. Details of the mechanics have to be confirmed. There are four temperature sensors per arm. One sensor monitors the forward lens, one the second lens, and the other two are at the rear of the cassette, in proximity to the return pipe. In addition, the lens cradles should be easily detachable from the arm and cooling system, permitting them to be conveniently extracted from the system through a flange or viewport.

The CRL support must include a mounting system with six degrees of freedom, and coarse adjustment of ± 10 mm in height with a mechanical locking mechanism on a thermally and mechanically stable base. These systems allow the CRL unit to be coarsely aligned with the beam, which will facilitate coarse alignment during beamline commissioning.

During operation, the plan is to connect the CRL unit to the equipment protection system (EPS), which has the task to automatically close a shutter whenever any reconfiguration of the CRL arms is made. However, this functionality is not guaranteed; a hardware interlock will trigger the EPS

watchdog to reduce the beam intensity in order to protect any material such as lenses, cradles, or arms when they are positioned in the beam or moving through the beam position. When any arm moves off from the clear position, a normally closed limit switch will open.

The CRL unit will be pumped by an ion pump connected directly via a 6” CF flange, after initial pump-down by the pump cart (Figure 4-21).

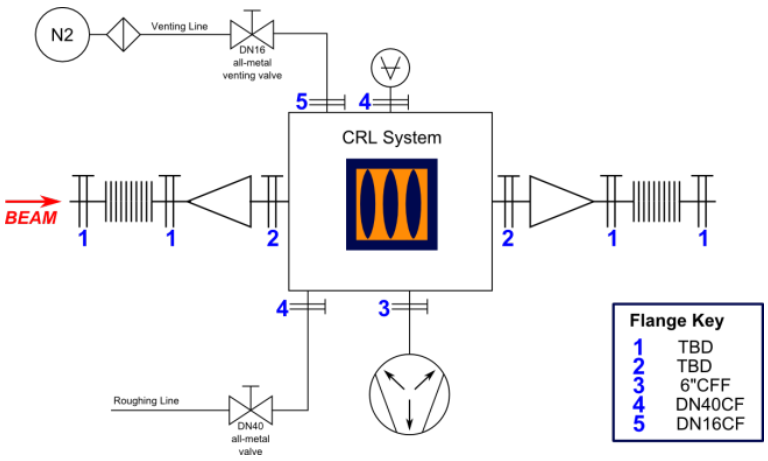

Figure 4-21. *Schematic of the vacuum layout of the CRL units. The flange sizes of the incoming and outgoing vacuum tubes differ for the three units.*

Table 4-11. *Mechanical data sheet of the CRL units*

System translation range	***x***	***y***	***z* (where applicable)**	**Pitch**	**Yaw**
	± 50 mm	**± 50 mm**	**± 25–250 mm**	**± 3°**	**± 3°**
Minimum translation size	≤ 10 µm		100 µm	0.1° / 175 mrad	
Resolution					
Encoder type	Linear absolute encoder			Rotary absolute encoder	
Encoder resolution	≤ 1 µm per count		100 µm	0.1° / 175 mrad	
Limit switches	At + 50.5 mm and - 0.5 mm	Two per arm; EPS-critical; one at “ACTIVE” (in-beam), one at “DEFAULT” (out of beam)	At both extremes of travel	At + 3.5° and - 3.5°	
Hard stop		At the “ACTIVE” position			

4.3.6 Nanofocusing setup

To achieve sub-micrometre spot sizes, a fourth CRL unit is envisaged (CRL4). With this unit, it is planned to achieve imaging of large samples in a magnifying geometry and perform sub-micrometre diffraction experiments, such as double diamond anvil cell experiments. This unit has to be installed very close to the sample, i.e. within the experiment chamber. To keep the setup in the chamber flexible, it may not be permanently installed.

For the smallest available radius of curvature of the lenses of 50 µm [10] and a fixed aperture of 400 µm, a focal spot of 40 nm can be achieved at 12 keV with 90 lenses. The corresponding focal distance is 130 mm. With the same number of lenses, nanofocusing to 70 nm can be achieved at 25 keV. The corresponding focal distance is 525 mm.

To realize a perfect overlap of beam position and sample surface, the CRL holder will be placed on a translation stage that will allow the lens to be moved along the *z*-axis. This movement is also required to shift the focus along the beam axis, which is needed to allow sample off-focus conditions as required for high-resolution magnifying imaging experiments, as have been performed in [34] (Figure 4-22).

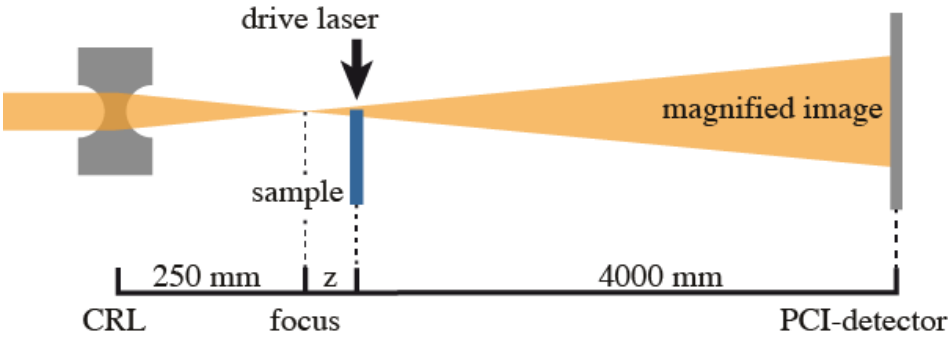

Figure 4-22. *Schematic of phase contrast imaging setup. The imaging capabilities are defined by a change in focus-to-sample distance, which has to be adjusted to the specific sample.*

For additional alignment purposes, the lenses have to be moveable in *x*- and *y*-directions and need to have the corresponding rotations. This could be realized at the required resolution by attaching the CRL unit to a hexapod placed on top of a long *z*-translation.

4.4 Split and delay unit

A split and delay unit (SDU) is planned for the HED instrument for the energy range of 5–20 keV. This unit will enable time-resolved X-ray pump – X-ray probe experiments as well as sequential diffractive imaging on a femtosecond to picosecond time scale [14]. In addition, direct measurements of the temporal coherence properties will be possible by making use of a linear autocorrelation. As a special operation mode for two-colour X-ray pump – X-ray probe experiments, the separation and delay of fundamental and third-harmonic radiation are considered. While this concept is not yet fully complete, first preparatory steps have been undertaken and were included in the SDU design.

The concept and most of the details of the SDU are outlined in the HED CDR, and the reader is referred to that document for more information. Here, integration into the beam transport, achievable delays, and further considerations for the two-colour mode will be presented.

4.4.1 Integration in the X-ray beam transport

The SDU will be positioned in the XTD6 tunnel at 846 m from the source. It will be positioned upstream of the four-bounce monochromator, the high-resolution monochromator, and the CRL2 unit (Figure 4-23). During normal operation of the SDU, the two delayed and nearly parallel beams will leave the SDU at the same height as the direct FEL beam. These beams will be overlapped on the sample. During two-colour operation, there will be an energy-dependent vertical offset between the two X-ray beams. The delayed “probe” and higher photon energy beam will be a few millimetres above the “pump” beam.

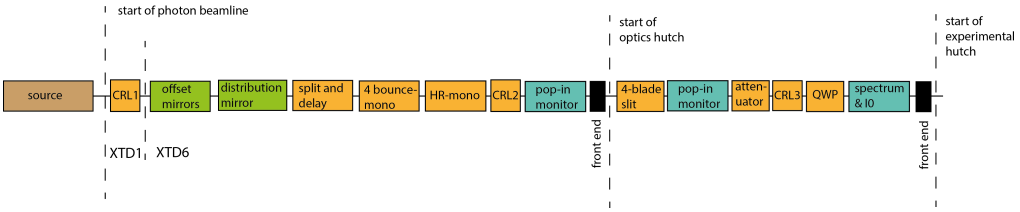

Figure 4-23. *Major optical components planned at HED in the three sections XTD1, XTD6, and optics hutch. Some essential beam monitors are also included in the sketch.*

4.4.2 X-ray scheme and achievable delays

The SDU splits the FEL beam into two beams using the sharp edge of a mirror (beam splitter (BS), Figure 4-24). Then, the two beams travel along different paths, both including two mirrors. The delay between the two beams is achieved by moving these mirrors such that their incidence angles with respect to the X-ray beam is kept constant while the path length is changed. Recombination of the two beams is achieved by a recombination mirror (RC), which reflects only one part to the last mirror, while the other beam impinges directly on the last mirror. All optical devices of the SDU are multilayer mirrors. Two different coatings have been selected to achieve a high reflectivity over the total energy range of 5–20 keV. Each mirror will have two coating stripes besides each other. By translation of the entire SDU, it is possible to change from one coating to the other. The operation angles of BS and RC are twice as large as for the other mirrors. Thus, different multilayer periods will be used for BS and RC. A promising combination is a *d* value of 1.57 nm for BS and RC, and 3.2 nm for the other mirrors. Due to the shallow incidence angles of multilayer coatings and the envisaged delays (see Table 4-12), the travel ranges of the mirrors have to be large. This results in an overall length of the SDU of 6 m (flange to flange).

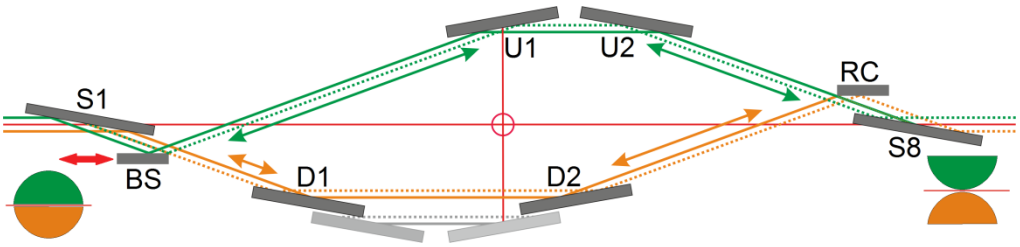

Figure 4-24. *Schematic layout of the SDU*

Table 4-12. *Total transmission and maximum delay times of the SDU*

Photon energy [keV]	Multilayer top material	Angle (BS) [°]	Maximum delay [ps]	Total transmission
5	Ni (W)	3.66	23	0.23
6	Ni (W)	3.07	16	0.33
8	Ni (W)	2.30	9	0.47
10	Ni (W)	1.83	6	0.21
10	Mo	2.28	9	0.29
12	Mo	1.90	6	0.35
15	Mo	1.52	4	0.41
18	Mo	1.27	3	0.43
20	Mo	1.14	2	0.23

The multilayer coatings have already been tested for performance. Figure 4-25 shows the reflectivity curve of a Mo-coated mirror at 18 keV, i.e. an angular scan around 0.63°. With a reflectivity of ~ 80% and a bandwidth of ~ 0.3 eV, the substrate nearly reaches the theoretical values.

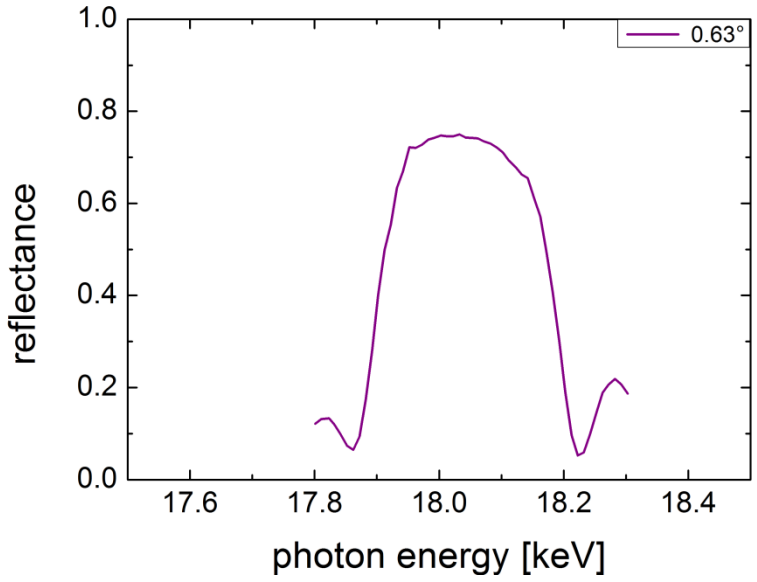

Figure 4-25. *Reflectivity curve of a Mo-coated mirror at 18 keV, i.e. an angular scan around 0.63°*

4.4.3 Alignment scheme

Alignment of the SDU will be achieved by a combination of beam monitors installed inside the SDU after each mirror. It is planned to install an X-ray generator a few metres upstream of the SDU to allow pre-alignment of the mirrors without the FEL beam. In addition, one monitor is planned at 20 m downstream of the SDU to fine-tune the alignment in the far field.

4.4.4 Special operation: two-colour experiments

As a special operation mode of the SDU, two-colour operation is being investigated. In this mode, the third harmonic is delayed relative to the first harmonic. This mode requires special tuning of the accelerator and the SASE2 undulator to enhance the generation of fundamental and third-harmonic FEL radiation, and tuning of the beam transport mirrors to propagate both photon energies. For the SDU, the S1 mirror must reflect both photon energies at high efficiency, while the four mirrors in the two arms need to reflect only one photon energy. The two beams will not be recombined at the SDU, but rather leave the device with a vertical offset as shown in Figure 4-26. This offset is energy dependent and varies between 7.47 mm for 20 and 6.7 keV and 10.33 mm for 15 and 5 keV. The corresponding delays between first and third harmonic are 250 fs and 445 fs, respectively.

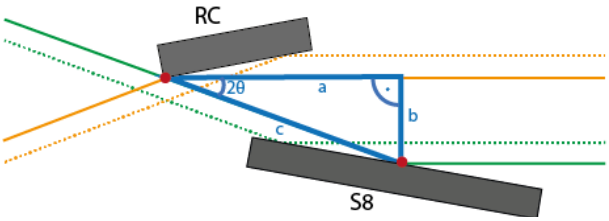

Figure 4-26. *Geometry of two-colour operation of the SDU. The RC mirror is rotated such that the "orange" part of the beam does not hit S8 but leaves the SDU parallel to the "green" part of the beam.*

The offset can be compensated by a tilt of the RC mirror such that the two beams overlap on the sample ~ 100 m downstream of the SDU. A tilt angle of only 0.06 mrad and 0.08 mrad is sufficient for 20 keV and 15 keV, respectively, and is clearly within the acceptance angle of the multilayer mirrors. This design, however, has the disadvantage that the two beams pass a different number of mirrors in the SDU, therefore making the transport of the

two beams asymmetric. Likewise, changing the delay becomes much more complex, and it would be preferable to insert an additional mirror in the path of the third-harmonic beam.

Furthermore, both the vertical offset and the different photon energies restrict the use of downstream optical elements, such as the monochromator, CRL2, and CRL3. An initial idea to use the existing monochromator in the “probe” beam for higher spectral resolution appears not feasible any longer. This is shown in Figure 4-27 for the four-bounce monochromator, where the fixed gap between the two crystals always stops one of the two beams. Most realistic at present is a scheme where both beams are transported in parallel into the HED-OPT hutch, in which a special optics setup, based on multilayer mirrors, is used to recombine and focus the two beams. This setup requires further design and will be realized as a future extension of the HED instrument.

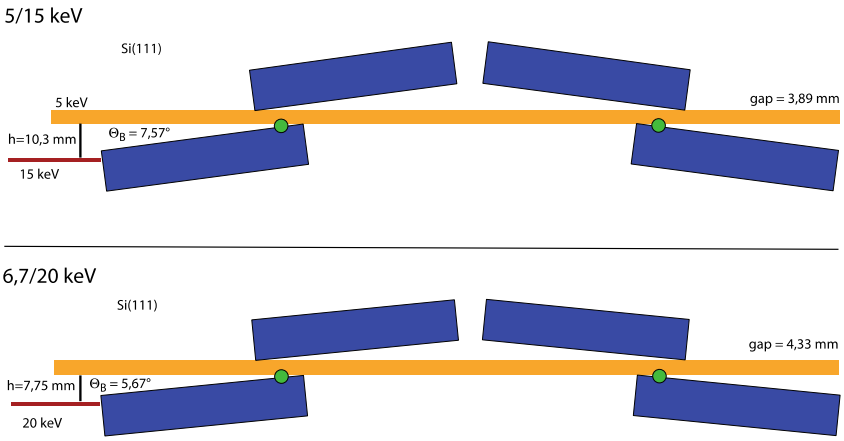

Figure 4-27. *Beam path of SDU with illustration of monochromator geometry requirements*

4.5 Monochromators

Monochromators will be installed to provide radiation of smaller bandwidths than that of the natural SASE beam or to clean the seeded FEL beam from unwanted spectral components. From the user requirements, a bandwidth of 10^{-4} over a broad energy range, as well as an energy resolution on the order of 10^{-6} for specific energies, is needed. For all applications, the photon flux

should be maximized for the selected condition. For experiments relying on an energy resolution of 10^{-4}, a four-bounce, perfect Si crystal monochromator will be available. Applications with higher energy resolution requirements will be served with an additional back-reflection monochromator, placed downstream of the first monochromator. It still needs to be clarified if this monochromator can be achieved as part of the first, baseline installation. This scenario will allow a stepwise monochromatization of the FEL beam.

4.5.1 Four-bounce monochromator

The first monochromator will be positioned behind the SDU unit and upstream of the CRL2 unit at 854 m from the source. This is about 118 m upstream of the sample. The required energy resolution for most envisaged experiments is in the range of 10^{-4}. Silicon monochromators are suitable to achieve such a value. Among the Si reflections, Si_{111} has the largest acceptance at an intrinsic energy resolution of 1.4×10^{-4} in the photon energy range of interest. Besides the energy resolution, the monochromator will allow operation in a large energy range and have extreme high stability of the output beam. A specially designed channel-cut crystal tilt stage with only a small range will provide this high stability. The principal energy range of 5-25 keV can be realized with a Bragg angle tilt range of only 20° using Si_{111} crystals. A two-crystal monochromator creates an energy-dependent vertical shift in beam position. This offset would require new alignment of the optical components downstream of the monochromator, as well as of the sample and detectors. To remove this offset, a second inverted two-crystal monochromator is introduced, thereby making the device a four-bounce monochromator (Figure 4-28). The use of four crystals instead of two reduces the flux on sample by a factor of 0.8, due to the reflectivity of 0.9 of each of the two additional crystals. Due to the extremely small FEL beam divergence, compared to the Darwin width of the Si crystals, no additional flux reduction through angular collimation is to be expected by the use of two additional Bragg reflections (Figure 4-29). The CRL1 stack can increase the X-ray beam divergence to maximum values between 4 µrad at 5 keV and 1.2 µrad at 24 keV, when used in the intermediate-focus configuration. This divergence is still below the Darwin width of Si_{111} and consequently will have no effect on the monochromator throughput.

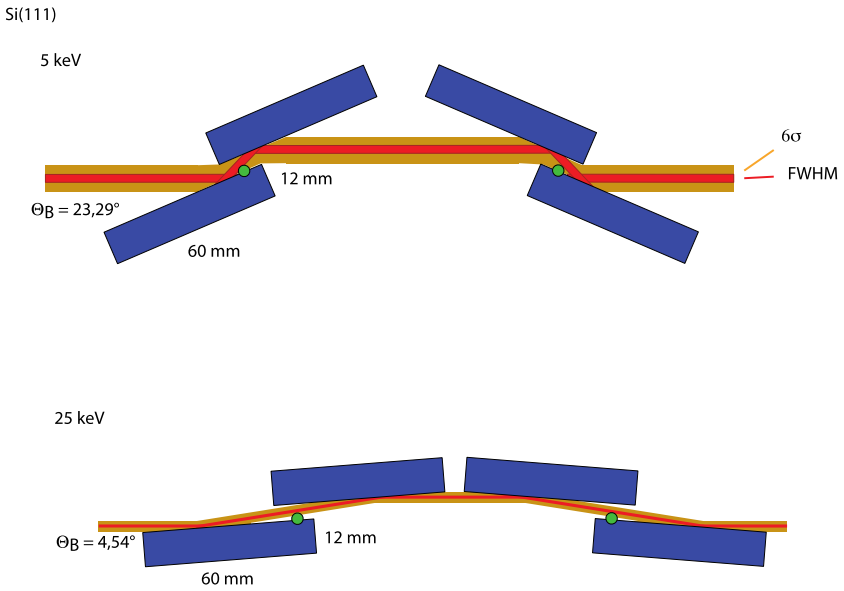

Figure 4-28. *Beam path of X-rays passing a double two-crystal monochromator for 5 and 25 keV*

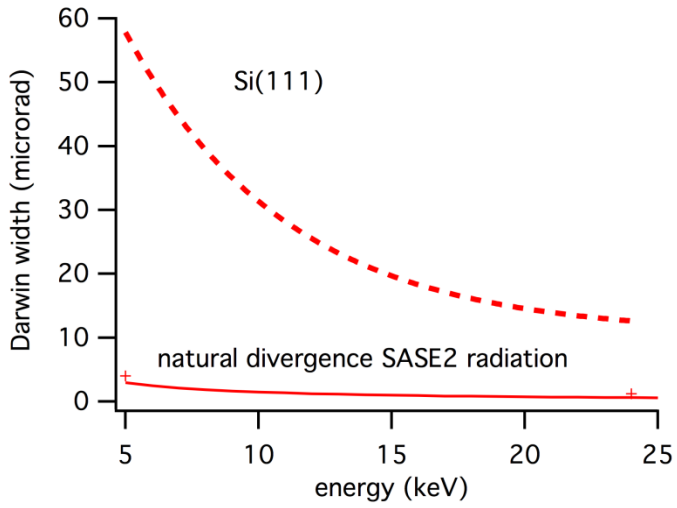

Figure 4-29. *Darwin width versus energy for a Si_{111}-reflected beam compared to the expected divergence of SASE2 radiation*

4.5.2 High-resolution monochromator

To achieve an energy resolution of 10^{-6}, we plan to have an additional channel-cut monochromator with usable Si_{444}, Si_{555}, and Si_{777} reflections instead of Si_{111} only. This can only be achieved in backscattering geometry. This device will be placed downstream of the Si_{111} monochromator. It is planned to operate this monochromator in combination with the first Si_{111}

channel-cut monochromator (Figure 4-30). The technical design for this high-resolution monochromator still has to be developed. Nevertheless, its application for energies of 7.918, 9.897, and 13.856 keV seems feasible using a backscattering angle of 87°. This fits well with the requirements for spectroscopy applications.

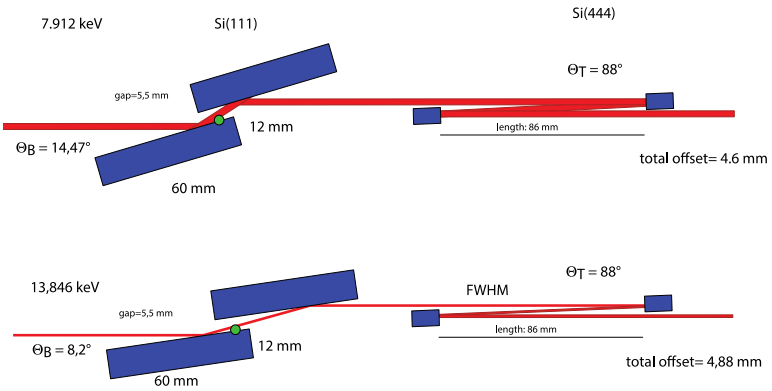

Figure 4-30. *Schematic beam path through the channel-cut Si_{111} and a backscattering monochromator placed at 88°. This corresponds to photon energies of 7.912 keV (top) and 13.84 keV (bottom).*

The high-resolution monochromator will be equipped with Si_{111} cut crystals. Likewise, the higher orders are accessible (Table 4-13). It will be operated at angles between 86° and 89°. This angular range provides some flexibility in energy but will produce a rather large beam offset. Table 4-13 shows the resulting energies and beam offsets. The energy resolution will be on the order of 5 x 10^{-6} or better, covering the requirements for inelastic X-ray scattering (IXS) experiments.

Table 4-13. *Calculations for a backscattering monochromator with a length of 85 mm*

Angle [°]	**89**	**88**	**87**	**86**
Reflection Si_{444}				
Energy [keV]	7.9083	7.9119	7.9179	7.9264
Reflection Si_{555}				
Energy [keV]	9.8854	9.8899	9.8975	9.9080
Reflection Si_{777}				
Energy [keV]	13.8395	13.8458	13.8564	13.8712
Offset [mm]	3.00	6.01	9.01	12.03

Due to the different geometries and *d* values of the first channel-cut Si_{111} and the following high-resolution channel-cut monochromators, a non-zero vertical beam offset results. Assuming a length of the backscattering channel-cut crystal of 86 mm (Figure 4-31), the offset will be smallest for reflection angles of 87° to 86° (Table 4-14).

Table 4-14. *Offset calculations for a backscattering monochromator operated with the artificial channel-cut monochromator*

Angle [°]	**89**	**88**	**87**	**86**
Reflection Si_{444}				
Total offset [mm]	7.65	4.64	1.64	-1.38
Reflection Si_{555}				
Total offset [mm]	7.78	4.77	1.76	-1.25
Reflection Si_{777}				
Total offset [mm]	7.88	4.88	1.87	-1.14

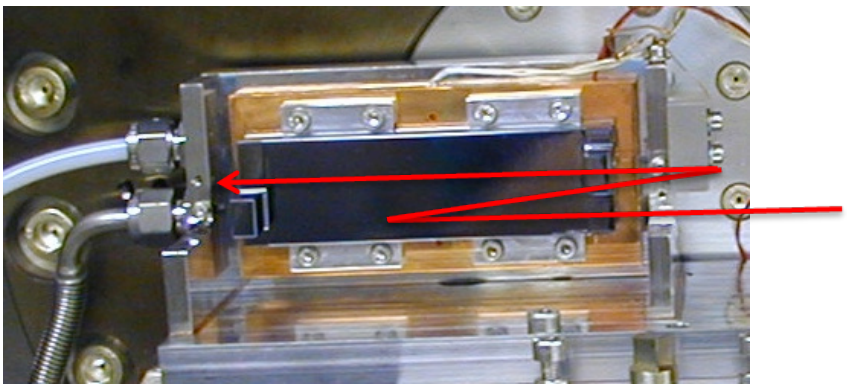

Figure 4-31. *Photograph of an example of a two-bounce backscattering channel-cut monochromator with the approximate X-ray beam path*

In summary, the following energy bandwidths will be available at HED:

- 10^{-3} for 3–25 keV (no monochromator)
- 10^{-4} for 5–25 keV (Si_{111})
- 10^{-6} for 7.9, 9.9, and 13.8 keV (backscattering monochromator)

4.5.3 Technical realization

All requirements for an energy resolution of 10^{-4} can be covered with dedicated channel-cut monochromators (Figure 4-32). The monochromator planned for HED is an in-house development based on the artificial channel-cut mechanism (ACCM) designed at the Advanced Photon Source (APS) at Argonne National Laboratory, Argonne, Illinois [15]. Details about this monochromator are described in “Technical Design Report: X-Ray Optics and Beam Transport” [16]. For HED, two units of ACCMs are planned that will be sitting behind each other on one common support table. The reason for this is to realize a fixed-exit design. Each ACCM is housed in a vacuum vessel and will be operated at UHV conditions. The vacuum vessel can be aligned with respect to the beam by a motorized support allowing five degrees of freedom (Table 4-15). Compared to a usual channel cut, the artificial channel cut has the advantage that both surfaces of the crystals can be polished in individual working steps. This will lead to a better surface polishing and thus minimizes wavefront distortions. Both channel cuts are connected by a weak link, which allows alignment of the channel-cut crystals against each other. The rotation of the crystals is performed with a sine-bar mechanism having a rotation range of 20° (Figure 4-32), which has the advantage of high stability. Bragg angles between 4.5 and 24.5° can be realized in the chosen design. Using crystal sets of Si_{111}, an energy range between 4.8 and 25 keV is covered. To allow a compact design of the channel-cut monochromator, the centre of rotation has been chosen to be on the surface of the first crystal, and the gap has been designed such that it is minimized but allows a 6σ large beam to pass the monochromator. The required gap of the two channel-cut crystals is 5.5 mm; the resulting length of the second crystal has to be 60 mm to accommodate the footprint of the beam reflected on the first crystal over the entire working range. The energy-dependent offset of the channel-cut monochromator is 10.10 mm for 4.8 keV and 10.96 mm for 25 keV. The second channel-cut monochromator has to be adjusted in height accordingly during energy changes to keep the offset fixed.

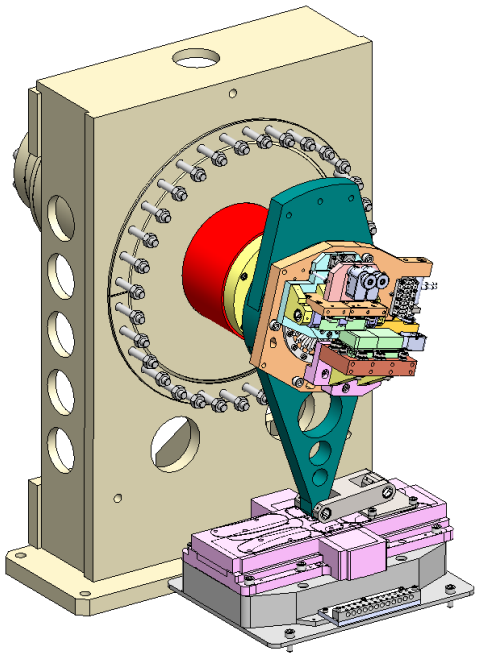

Figure 4-32. *Schematic view of the inside of the artificial channel-cut monochromator*

Table 4-15. *Planned translations for the artificial channel-cut monochromator*

Translations	**Range**
Channel cut:	
Bragg angle	4.5–24.5°
Horizontal translation (*Rx*)	-1–15 mm
Vertical translation (*Rz*)	-15–15 mm
Second crystal:	
Pitch (*Rx*2)	-0.5–0.5°
Roll (*Ry*2)	-0.5–0.5°

All monochromator crystals can be cryo-cooled to minimize X-ray beam heating effects in pulse train operation. In addition, heaters are foreseen on both crystals to adjust temperatures during operation and control the process of temperature stabilization. More information on the technical design of the monochromator can be found in “Technical Design Report: X-Ray Optics and Beam Transport” [16].

4.6 Monitors

X-ray monitors are included in the beam transport system at several places in order to obtain information on intensity, position, and shape of the X-ray beam. Two generally different types of monitors are used: “Online” monitors can be operated simultaneously with the experiments and are only minimally invasive. These monitors can be permanently installed and do not require removal from the X-ray beam path. A second category of monitors is invasive and does, in general, not allow simultaneous monitoring and execution of experiments. These monitors need to be positioned on and removed from the X-ray beam path. The invasive monitors are used for beam performance and alignment purposes, while the online monitors provide feedback on the X-ray FEL beam intensity and position used for normalization of experiment data.

The first online monitor will be an X-ray gas monitor (XGM) installed in XTD1 as close as possible to the source, i.e. upstream of the first optical element (Figure 4-33). This XGM measures photon flux and beam position. A second XGM will be positioned at the end of the XTD6 tunnel. This section between the two XGMs includes major optical components, such as the mirrors, the SDU, the monochromators, and the two CRLs. A further flux monitor will be positioned at the end of the optics hutch, downstream of any optical element, and will also be used to monitor the incident intensity (I_0).

Invasive monitors (sometimes also called “pop-in monitors”) are fluorescence screens combined with an optical system for imaging the fluorescence screen onto a remotely read charge-coupled device (CCD) camera. They will be placed after the major optical components and will allow observation of the X-ray beam during alignment. For HED, three pop-in monitors are planned so far in the X-ray beam transport inside the tunnels. The first will be installed in XTD6 downstream of the second offset mirror. The next pop-in monitor will be placed after the distribution mirror. Those two monitors are shared by MID and HED. The last pop-in monitor will be positioned at the end of XDT6, in front of the beam shutter. This monitor has the task of controlling the beam after it has passed all optical components in this section of the X-ray beam transport.

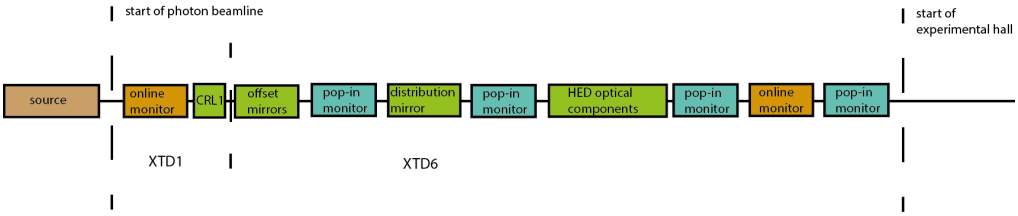

Figure 4-33. *Monitors installed in the tunnel areas XTD1 and XTD6 of SASE2*

In addition to these monitors, two more invasive monitors are required for the alignment of HED-specific optics. The first will be placed 20 m downstream of the SDU for visualization of the X-ray beam during alignment of the SDU, monochromators, and CRL2 unit. The other will be placed at the entrance of HED-OPT, behind the slit system, and will serve to visualize the collimated beam. The downstream components, attenuator, and CRL3 unit can then be aligned with a monitor placed at the sample position.

4.6.1 Online monitors

The online monitors will provide photon flux and beam position information on individual X-ray FEL pulses. More accurate data are achieved by integrating over a larger number of pulses. The online monitors are permanently installed and affect the beam properties as little as possible. For HED, they need to be operational over an energy range of 3–25 keV and be able to cope with 10^{8}–10^{12} photons per pulse and with variable beam sizes (0.2–3 mm). The design for the online monitors is a gas-based detector system (XGM). These detectors are to be filled with noble gases, which can be exchanged and adjusted to the energy range of interest. To obtain sufficient signal, the gas pressure has to be as high as 10^{-4} mbar. To connect the monitors to the beamline vacuum, a differential-pumping section is needed upstream and downstream of the monitor. The monitors are developed by K. Tiedke's group at Deutsches Elektronen-Synchrotron (DESY).

An I_0 monitor will be installed in HED-OPT upstream of but as close as possible to the sample. This monitor will measure the X-ray flux after the beam has passed all optical elements of the X-ray beam transport. This information should be available on a single-pulse basis for the entire energy range, and ideally the device should be operational up to the full load of the FEL beam. The current concept is unchanged from the HED CDR and is

based on backscattering from a thin solid foil with special measures to enable a high dynamic range. No technical design exists yet.

4.6.2 Spectrum monitor

A special type of online monitor is used for single-shot spectral diagnostics. This device will provide, on a single-shot basis, information on the spectral composition of the X-ray FEL pulses required for commissioning purposes as well as for online beam monitoring during user experiments. At the moment, it is envisaged to have this device installed in front of the distribution mirror in XTD6. This spectrometer is planned and provided by the X-Ray Photon Diagnostics group at European XFEL. At HED, the installation of additional devices is considered as required for XAS-type experiments. For the XAS measurements, two such monitors are planned: one in front of the sample, likely to be positioned inside HED-OPT, the second behind the sample, possibly to be integrated in the beam stop inside HED-EXP.

For the moment, no detailed technical design exists for the X-ray single-shot spectrometer. The concept for this monitor, however, is based on bent Si crystals as shown in [17]. The spectrum measurement is achieved by detecting the Bragg diffraction from bent Si crystals, likewise creating spectral dispersion as a function of the position on the crystal surface. The diffracted beam could be recorded with a suitable 1D detector. For a given beam cross section, the geometry has to match the spatial resolution of the detector, the photon energy, and the required energy range of the spectrum to be measured. Two geometries have been investigated so far. In [15], a 10 µm thin Si crystal with a radius of curvature down to 150 mm was used in the direct FEL beam (see Figure 4-34) and could achieve an energy resolution at 8.3 keV of 0.5 eV and 0.2 eV using Si_{111} and Si_{311} reflections, respectively. The disadvantages of this setup are an attenuation of the direct FEL beam by the crystal and, correspondingly, the subsequent heating and potential for melting of the crystals in the X-ray pulse trains of the European XFEL.

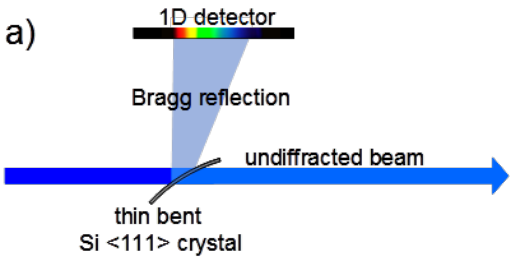

Figure 4-34. *A thin bent crystal is introduced into the FEL beam. Part of the beam will be Bragg-diffracted. This beam will be recorded on a 1D detector. The undiffracted part of the FEL beam will be transmitted to the experiment.*

An alternative setup uses a beam splitter to generate a specific, low-intensity diagnostics beam. This concept leaves the main fraction of the X-ray beam minimally affected for the simultaneous execution of experiments. One proposal is to use a thin diamond grating placed into the X-ray beam [18]. The diffracted beam hits the curved Si crystal, and the diffraction profile is imaged using a 1D detector (Figure 4-35). The diamond grating has the advantage that the absorption is low, but the availability of suitable gratings is very limited, and the possibility of placing them into the X-ray pulse trains requires further investigation.

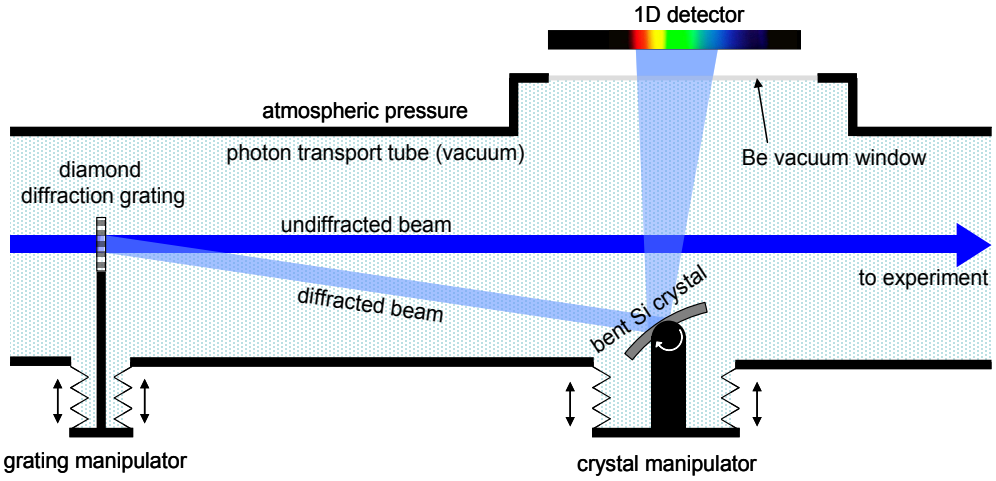

Figure 4-35. *Schematic sketch of the layout of the spectrum monitor. A diamond grating is used to diffract part of the FEL beam and illuminate a bent Si crystal. The dispersed signal from the Bragg diffracted beam is recorded in a 1D detector.*

4.6.3 Invasive beam position monitors

Removable, invasive monitors are planned at several places in the X-ray beam transport system. They are either positioned downstream of an optical element or towards the end of a section, i.e. at the end of the tunnel. They are designed for a maximum X-ray pulse delivery rate of 10 Hz and have to be removed during the operation of experiments. Design and installation are performed by the X-Ray Photon Diagnostics group. These devices are based on a removable scintillator screen, which is observed by a camera. YAG:Ce was characterized to be a good scintillator material for these monitors [19].

Two different types of monitors are envisaged for SASE2:

1 Type I is for a small field of view of approximately 35 mm at tunnel positions after the monochromators where no beam deflections occur. The scintillator is positioned at 45° to the X-ray beam axis, which degrades spatial resolution slightly in one orientation; however, it avoids having a mirror in the X-ray beam to reflect the optical image to the camera. For HED, this type will be installed at the end of XTD6, at 938 m from the source.

2 Type II for a field of view of 150 mm in the horizontal direction to observe the beam deflection after the second offset mirror. It uses a scintillator at 45° to the X-ray axis. At SASE2, this type of monitor will be installed after the offset mirrors, at 305 m and 400 m from the source.

The main difference between Type I and Type II is the field of view. It is 35 x 35 mm^2 for Type I and 150 x 150 mm^2 for Type II. The expected spatial resolution is in the range of 130 µm (Figure 4-36 and Figure 4-37).

For the additional X-ray screen monitors at HED, it has to be verified whether the above devices fit the requirements for the alignment of the SDU, monochromator, and CRL2, as well as for beam visualization inside HED-OPT. In both cases, beam offsets are fairly small, requiring a field of view of ~ 35 x 35 mm^2, but spatial resolution should be on the order of 20 µm.

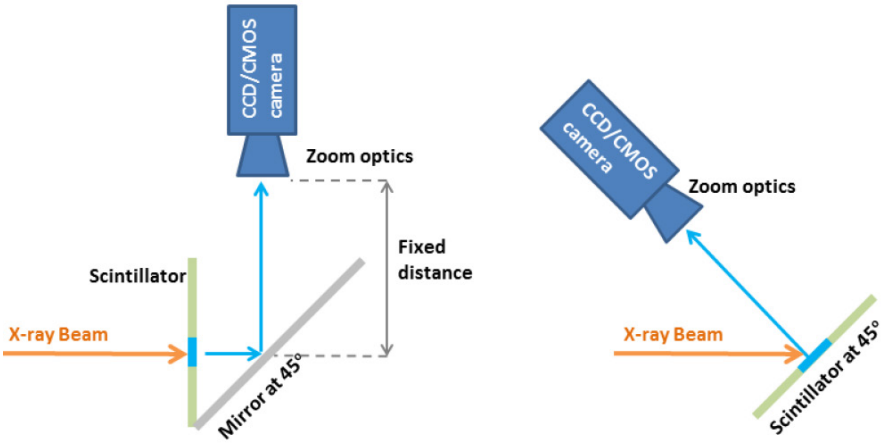

Figure 4-36. *Two different geometries of the invasive X-ray beam position monitors. In the design shown on the left, the scintillator screen is positioned at 90° to the incoming FEL beam. A mirror is required to visualize the beam on the CCD camera. The design shown on the right does not need a mirror: the scintillator screen is positioned at 45° to the incoming beam. This geometry allows the camera to be positioned in such a way that the screen is directly visible.*

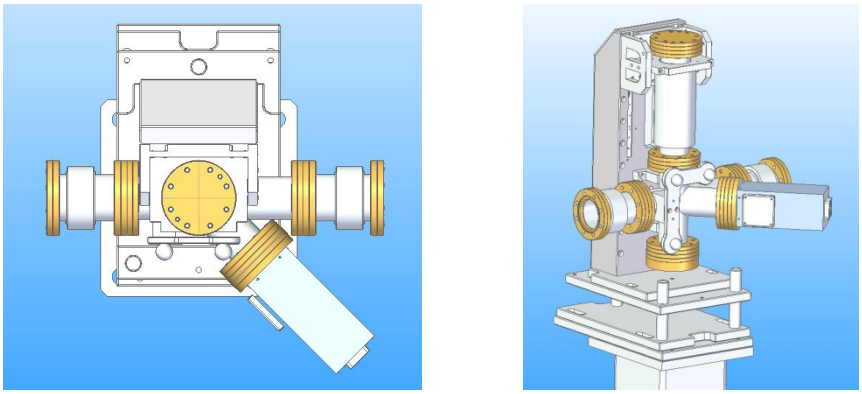

Figure 4-37. *Top view of the vacuum vessel holding the invasive beam position monitors*

4.7 Other X-ray beam transport components

This section describes the pulse picker, four-blade slits, attenuator, beam shutter, anti-scatter slit, beam stop, and vacuum system for the HED instrument.

4.7.1 Pulse picker

A pulse picker is planned at SASE2 to allow operation at reduced pulse modes. At present, selection of pulses at rates of up to 10 Hz is envisaged. In the future, higher rates may serve down-select pulses inside an X-ray pulse train. The design, which is conceptual for the moment, is based on an existing design at the FLASH free-electron laser facility at DESY (Figure 4-38). This design can be operated in single-shot mode. Motor and rotor move following a trigger by a clock signal. Continuous mode is possible by sending repeated commands. At FLASH, the pulse picker is frequently used at 10 Hz, while 20 Hz are also possible.

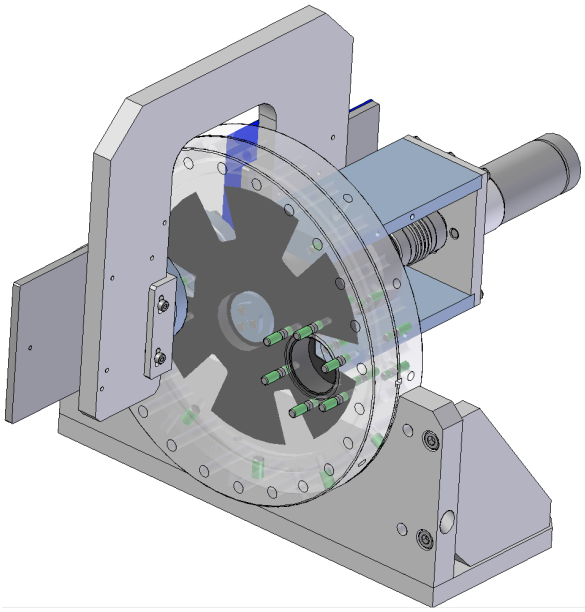

Figure 4-38. *Pulse picker used at FLASH. The rotation of the screen is either triggered by a FLASH clock signal to enable single-shot operation or is operated in continuous mode to enable 10 Hz pulses.*

The pulse picker at SASE2 will be positioned towards the end of XTD6 at 878 m from the source, upstream of the last pop-in monitor in this section and of the front end. Unlike at FLASH, the rotor will be made of a 1 mm thick aluminium rotor with a 100 µm thick tantalum backing. The aperture will be increased to 30 mm. The pulse picker is operated with a torque step motor plus gearbox. Motor and gearbox will be positioned outside the vacuum vessel and will be linked to the rotor by magnetic coupling. The rotor movement will be encoded.

A central piece of the device is the timing between the rotor movement and the X-ray FEL pulse train. The goal is to have an adjustable delay to trigger the movement. Operation at up to 50 Hz is envisaged.

4.7.2 Four-blade slits

The X-ray slits, located inside the HED-OPT hutch, will serve to define the beam size and to block the beam halo propagating with the main pulse. Trimming or shaping the X-ray beam can be done only in cases where the incident intensity does not damage the blades.

Each pair of slits is composed of two offset and opposing B_4C blocks with tungsten knife edges, which overlap when in the closed position. Both pairs are offset with respect to each other and include a translation mechanism, motor, and encoder.

The defining edges of each of the four blades, and thus the aperture, can be positioned anywhere within the translation range to accommodate beams of varying positional offsets and diameters. It is possible to position the aperture at any place where the beam can be delivered by the preceding beam transport or instrument optics. This operating range or maximum aperture is 50 x 50 mm^2 (Table 4-16). Each blade therefore has a stroke of 50 mm. Figure 4-39 shows three permutations. The rectangular aperture can be positioned anywhere within the yellow dotted footprint.

Table 4-16. *Mechanical characteristics of the four-blade slit system*

Translation range (first blade of a pair)	- 25 mm to + 25 mm (max. aperture = 50 mm) with respect to the centre of the beam
Translation range (second blade of a pair)	+ 25 mm to - 25 mm (max. aperture = 50 mm) with respect to the centre of the beam
Min./max. linear translation	≤ 1 µm / 50 mm
Repeatability	≤ 1 µm (from one side)
Parallelism of blade	≤ 0.02° / 350 µrad during pump-down or motion
Orthogonality of blade	≤ 0.02° / 350 µrad during pump-down or motion
Encoder type	Linear incremental encoder; Beckhoff-compatible
Encoder resolution	≤ 1 µm per count
Blade tilt adjustment	± 1° (17.5 mrad) port alignment adjustment

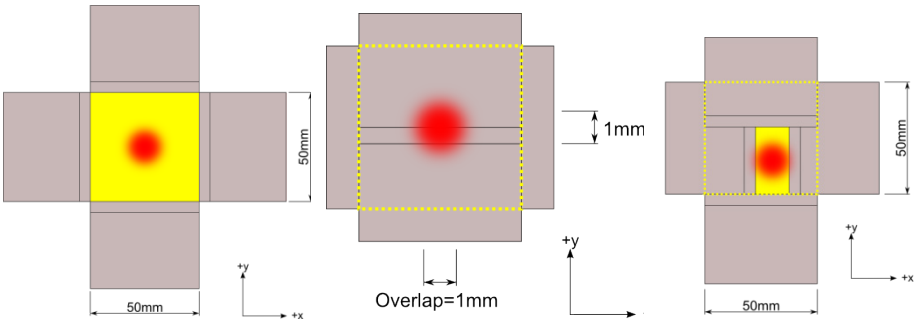

Figure 4-39. *Blade configuration in the maximum-aperture (left), closed (centre), and rectangular-aperture (right) positions*

The European XFEL beam will subject illuminated components to substantial heat loads. The cooling system is capable of rejecting 30 W continuously on a single B_4C/W blade. This is foreseen as the highest peak heat load expected with a safety margin. In all other cases, the total heat load (< 30 W) is distributed across two or more blades. To allow a precise alignment of the aperture assembly angle with respect to the beam, a tilt adjustment mechanism is required for each blade. This adjustment is accessible from outside the system while the unit is installed into the beamline and evacuated. Each blade will have a manually adjustable range of ± 1° (17.5 mrad). The two blades in a pair will remain parallel to each other during motion and evacuation cycles to ≤ 0.02° (350 µrad). The horizontal pair of blades will remain orthogonal to the vertical pair during motion and evacuation to ≤ 0.02° (350 µrad). The design will also permit the removal of each blade for inspection or blade replacement while the arms and all other parts remain in situ along with the main vacuum vessel. This will be achieved by the disassembly of a single flange or viewport, and the inspection and replacement of any blade or all of the blades while all other components remain in situ. The slit system is mounted on a three-plate manual alignment system to facilitate coarse alignment and on a thermally stable and stiff support structure to operate from. The support structure will allow the slits to be positioned at the nominal beam height of 1400 ± 10 mm.

The output from limit switches and encoders will be integrated into the local Beckhoff controller as well as the machine control and protection system watchdog.

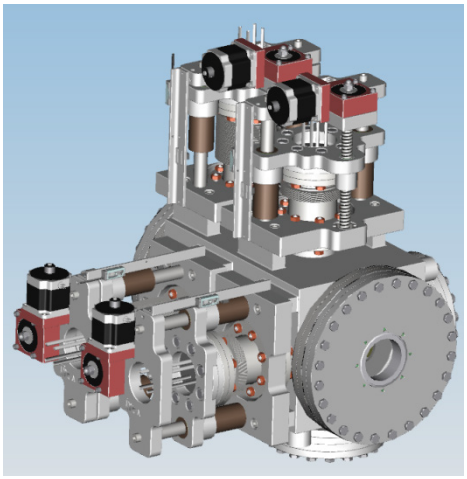

Figure 4-40. *Technical drawing of the four-blade slit system. The technical drawing was provided by JJ X-Ray A/S in Lyngby, Denmark.*

4.7.3 Attenuator

The attenuator is used to attenuate the X-ray beam in a controlled fashion as required for the experiment, for example, if the full intensity would be harmful to samples or instrumentation, or would at least create thermal distortions. The attenuator can also be used to adjust the photon flux delivered to the sample for fluence- or intensity-dependent experiments. The requirement for attenuation can be as high as eight orders of magnitude. The attenuator will be available for users to adjust photon flux, and therefore remote control is required. Detailed requirements are described in the HED CDR.

The attenuator will be integrated into the ultrahigh-vacuum (UHV) beam transport system and is capable of indefinite operation while illuminated by the X-ray FEL beam at 10 Hz up to Mode 3 (see Section A.1, “Operation modes at the European XFEL”). Full-bunch operation at 4.5 MHz will be possible with a limited machine mode delivering fluences below the melting point of the illuminated foil or absorber block. Cooling by means of water will support this mode of operation.

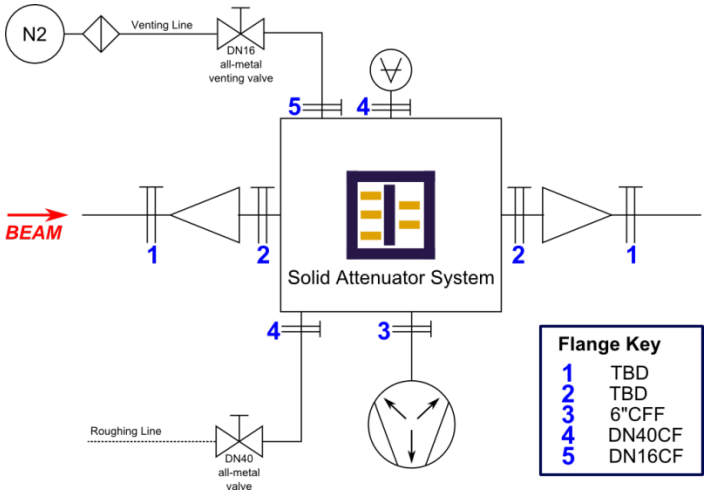

Figure 4-41. *Vacuum schematic for the attenuator unit. At HED, Flanges 1 and 2 are DN63 CF flanges.*

The technical design of the attenuator is nearly complete (see Figure 4-41). It includes four actuator arms, each having six absorber positions. A B_4C aperture will be integrated at the upstream beam entrance to protect metallic parts of the foil holder and the copper during alignment and against misdirected beams. The inner diameter of the aperture is 18 mm, centred on the X-ray beam axis. When mounted onto the actuator arm, the absorbers with thicknesses between 10 µm and 16 mm overlap with the adjacent absorber by 1 mm. Absorbers thicker than a few millimetres, such as the B_4C plates, have slanted sides so the overlapping scheme does not become too bulky to fit into a standard DN63 tube. This minimizes the range of extension of each arm along the *z*-axis, permitting efficient packaging, and a sequential step-down or -up in attenuation factor when moving to adjacent foils. The overlapping configuration ensures that material is always present when repositioning the arm during illumination with the X-ray FEL beam.

The B_4C blocks are mounted in an intermediate flanged housing to permit easy disassembly and service. Metallic components, such as cooling pipes, are not allowed to cross the beam path during any possible movement of the arm. A hard stop is integrated into the design to ensure this.

The attenuator is mounted on a thermally and mechanically stable base, which is to be bolted directly onto the laboratory floor. The active centre of the attenuator system corresponds to the beam axis, 1400 ± 10 mm from the

floor. The attenuator system will be mounted on a system that provides remotely operated fine alignment of the entire system along the *x*- and *y*axis with a range of 20 mm (± 10 mm).

The output from limit switches and encoders will be integrated into the local Beckhoff controller as well as the machine control and protection system watchdog. Two states are required to be switched electrically for this system: no material in the beam: “CLEAR”, and material in the beam: “DEFAULT”.

Table 4-17. *Mechanical characteristics of the attenuator unit*

Translation range	0 (“DEFAULT” on thickest/densest foil) to + 145 mm (edge of “CLEAR”)
Min. translation	≤ 10 µm
Repeatability	≤ 100 µm
Encoder type	Linear incremental encoder; Beckhoff-compatible
Encoder resolution	≤ 10 µm per count
Limit switches	Both directions at “CLEAR“ (no foil in beam) and the maximum extension of arm; all limit switches must be normally closed, single throw, and double pole
Hard stop	Adjustable hard stop at “DEFAULT” and “CLEAR”
Position/status indicator flags	Limit switches at extremes of travel

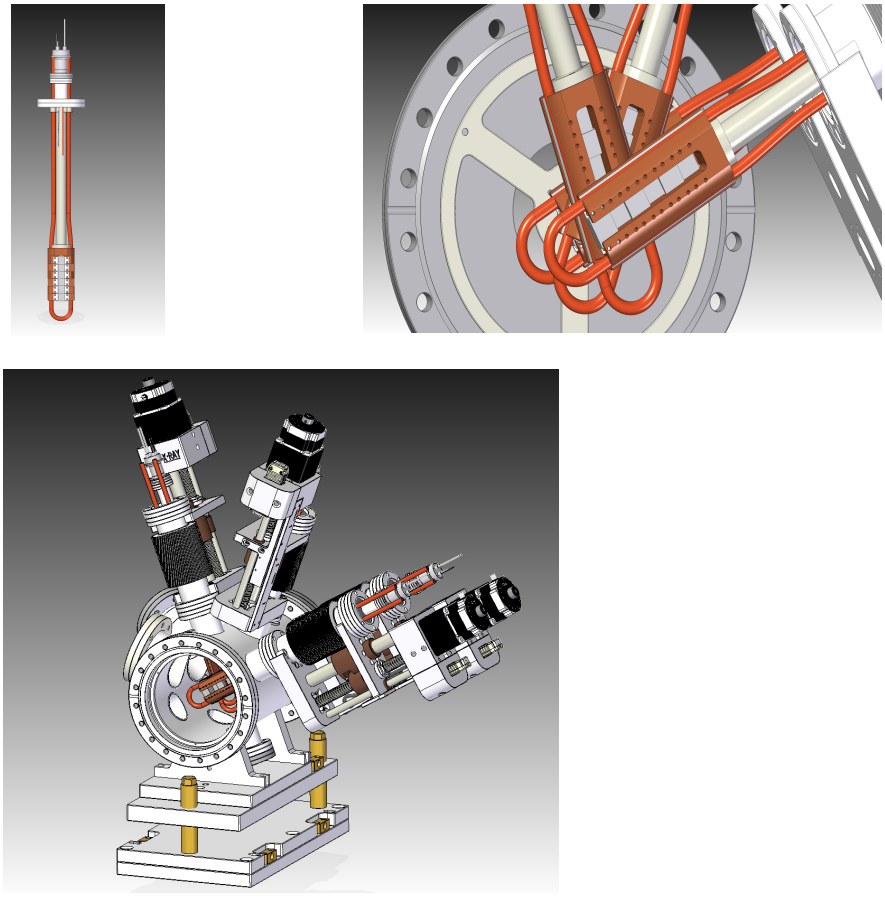

Figure 4-42. *Technical drawing of the attenuator arms (top) and the vacuum vessel (bottom) of the attenuator unit. The technical drawing was provided by JJ X-Ray A/S in Lyngby, Denmark.*

4.7.4 Beam shutter

A beam shutter will be placed in HED-OPT. It will allow the FEL beam to be blocked to enable access to HED-EXP without shutting down the FEL beam in HED-OPT. At present, we copy the design from the XTD6 tunnel provided by the X-Ray Optics and Beam Transport group. It was chosen since the radiation-shielding requirements for the two locations are rather similar. This system is equipped with a B_4C collimator, a B_4C power absorber, a tungsten collimator, and a tungsten shutter. The tungsten shutter is based on the PETRA III shutter design at DESY. The design allows the shutter to be closed up to Mode 3 of the FEL beam. In Mode 4, the machine has to be switched back to Mode 3 before the shutter can be closed. A sketch of the beam shutter components and dimensions is shown in Figure 4-43 and Figure 4-44. More information on the front-end design can be found in the technical

description of front ends as provided in [20]. The adaptation of this device to HED-OPT still has to be done.

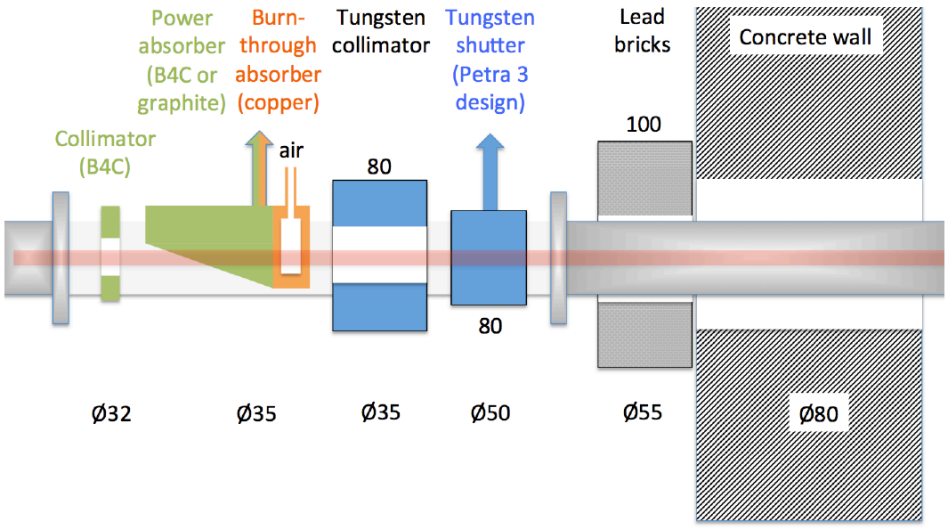

Figure 4-43. *Schematic front-end design for transition from photon tunnels to experiment hall [16]*

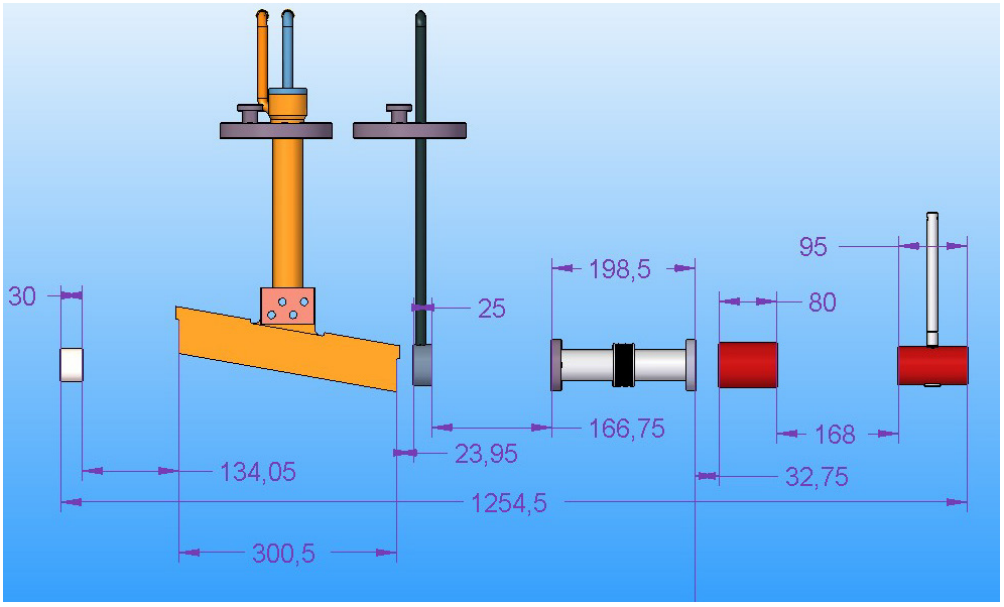

Figure 4-44. *Final design of the front end. Numbers are in millimetres. The total length of the assembly is about 1.5 m.*

4.7.5 Anti-scatter slit

An anti-scatter slit is necessary at HED. It removes unwanted parts of the beam, e.g. scattered radiation from upstream optical components. It will be positioned as close as possible to the sample, i.e. possibly inside the interaction chamber. No design for the anti-scatter slit exists at the moment. It will be evaluated whether a blade design or an aperture is better suited for this purpose.

4.7.6 Beam stop

The beam stop inside HED-EXP terminates the X-ray beam transport. It is positioned at the west wall of HED-EXP at about 978 m from the source. The beam stop has to enable the X-ray beam to be stopped under all possible configurations of X-ray delivery and X-ray optics. It is thus the defining device to limit the capability of the HED instrument to be operated at specific beam modes. No final technical design exists yet, but several concepts have been proposed and are scrutinized at present. In this section, we list the requirements that exist for the beam stop.

X-ray beam properties can range from 3 to 25 keV with pulse energies on the order of one to a few millijoule per pulse. Inside X-ray pulse trains, integrated energies of up to a few joule will be reached, this number being relevant for determining the melting threshold of the beam stop. Of further importance here is the X-ray beam size, which is smallest for configurations when CRL2 is used to focus the beam. Wavefront simulations show that the beam size can be as small as around 20 µm for energies above 10 keV, but will be significantly larger than 30 µm for lower energies. Figure 4-45 shows the limitation in energy that has to be met to avoid melting of a B_4C beam stop during exposure to the beam. The upper figure shows the single-shot limit, which is above 1 mJ for the entire energy range and spot sizes above 30 µm. This means that single-shot ablation should not happen. During a pulse train, in addition to single-shot ablation effects, heat flow into the B_4C has to be considered. This effect is most pronounced for small beam sizes and low photon energies. Assuming pulses with 1 mJ, the limit of 1 J can be reached for a beam with a diameter of 30 µm (yellow curve) at energies of 15 keV and above. This would mean that 1000 pulses could be allowed for 15 keV. For

low energies, the situation can be significantly improved by tilting the B_4C with respect to the X-ray beam, which would result in grazing-incidence geometry (dashed line).

The device has to operate under UHV conditions and, in general, will be connected to the X-ray beam transport vacuum. A valve may be useful for connection to the beam transport vacuum, maybe even including a diamond window for operation of the parts of the instrument inside HED-EXP under ambient conditions. The device should be rigidly supported close to or directly on the west wall of HED-EXP.

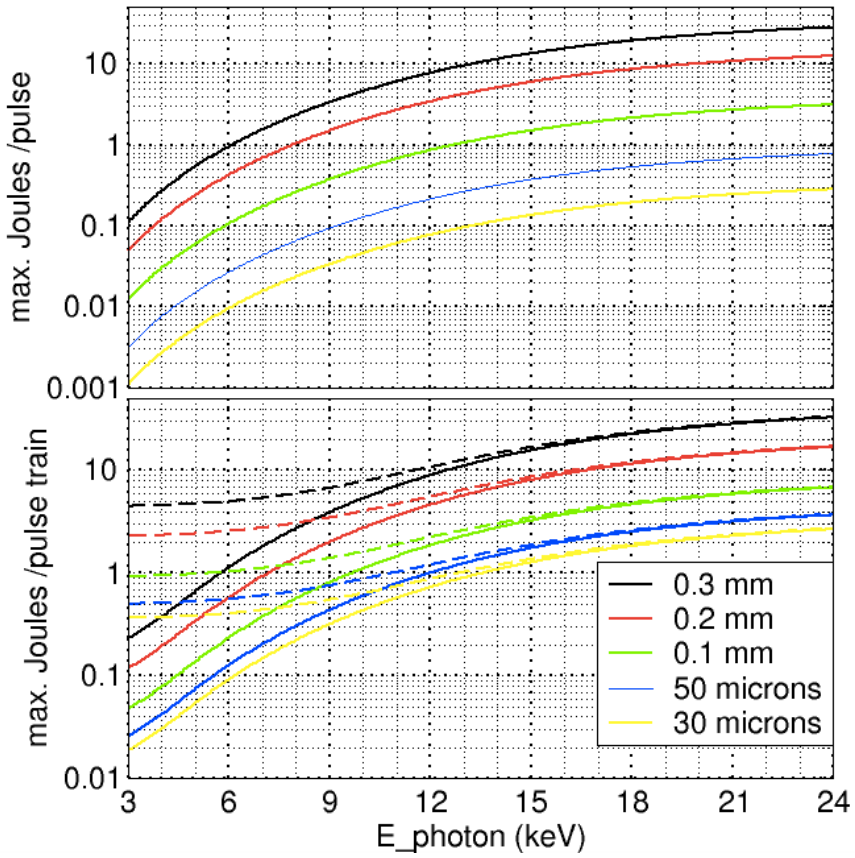

Figure 4-45. *Maximum energy of the X-ray beam for single pulse (top) or pulse train (bottom) impinging on the beam stop and avoiding its melting, as a function of photon energy and for several beam sizes. Calculations have been performed for perpendicular (solid lines) and grazing incidence (2°; broken lines) on B_4C.*

4.7.7 Vacuum system

The vacuum system of the HED instrument starts at the interface to the beam transport vacuum at the entrance to the experiment hall (XHEXP). The ~ 40 m vacuum system of the HED instrument has four major sections. Following a 20 m long transport tube without any optical elements, the installations inside HED-OPT are considered as the second section. The third section is the HED-EXP area, including several experiment chambers. Finally, the whole laser beam transport vacuum is considered as the fourth section, which is discussed in Section 5.1.3, “PP-OL beam transport” on page 92.

At the entrance to XHEXP, the vacuum has to fulfil the strict requirements defined for the UHV system in the beam transport section. This will be controlled by measuring the pressure on the instrument side of the last valve of the beam transport system. In case the vacuum exceeds a pre-set pressure level, the valve closes and operation of the instrument will be interrupted. The beam transport tube vacuum is controlled by the beam delivery vacuum system. The vacuum conditions in this section will be achieved by ion getter pumps, and pressure may not exceed 1×10^{-8} mbar. If this pressure is not exceeded, a signal will be send to the interlock system to enable the beam transport into the HED-OPT area.

Devices located in HED-OPT will be permanently under vacuum. In normal operation, the pressure in this section should not exceed 1×10^{-8} mbar. Installations in HED-OPT have a self-contained vacuum system. Initial pump-down will be achieved using pump carts. These will be removed during experiment operation, and the vacuum will then be maintained with ion getter pumps.

At the transition from HED-OPT to HED-EXP, differential pumping is required for a windowless connection of the ultrahigh vacuum in the optics section and the high vacuum inside the interaction chamber IA1. A differential-pressure step as high as four orders of magnitude will be planned for, enabling the operation of IA1 with a pressure as high as 10^{-4} mbar. The differential-pumping section should be able to cope with a possible vertical offset of the beam of up to 12 mm. Besides these requirements, the design of the differential-pumping unit has to be optimized for space. No technical design

exists so far. In normal operation, the connection to the HED-EXP section will be windowless. To enable experiments or alignment at ambient conditions, the valve connecting the vacuum sections inside HED-OPT and HED-EXP will have a diamond window. The vacuum system inside HED-EXP may change significantly, depending on the experiments performed. In general, it is foreseen to have closed vacuum up to the beam stop at the west wall of HED-EXP. This requirement follows from the high-energy X-ray beam and is amplified by the very small beam sizes in this area. Likewise, this beam leads to an extreme risk of damaging or breaking vacuum windows, no matter what kind of material they are made of. The insertion of windows into the X-ray beam will therefore be permitted only when specific and well-defined X-ray beam conditions are established. Inside HED-EXP, several large vacuum vessels may be operated, e.g. the IA1 and IA2 chambers. The vacuum conditions for these chambers still need to be defined, but, for a rapid pump-down, a huge capacity will be required. It is planned to place the vacuum pumps for these operations in a dedicated, noise- and vibration-isolated pump room. The HED pump room contains roughing pumps and backing pumps that are used in HED-EXP and ultrahigh-intensity optical laser (UHI-OL) installations. A schematic of the vacuum layout is shown in Figure 4-46. It includes details for the connections between the X-ray FEL beam transport system and the beam transport for the pump–probe optical laser (PP-OL) and the UHI-OL.

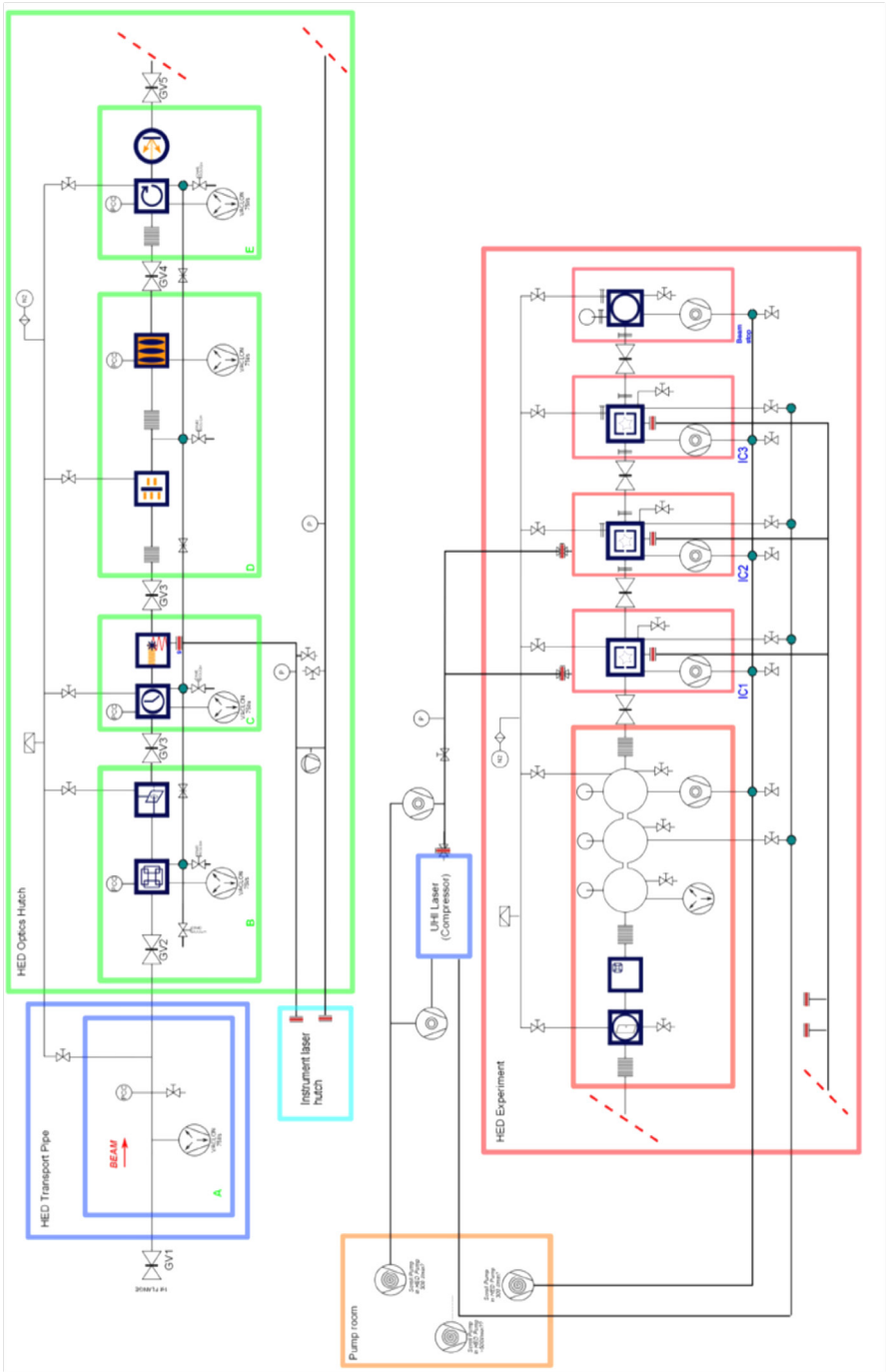

Figure 4-46. *Schematic vacuum layout of the HED beamline in the experiment hall. This sketch includes the vacuum for the X-ray beam, the pump–probe optical laser and the ultrahigh-intensity laser. The different locations are marked by coloured frames.*

5 Optical lasers

This chapter describes the integration of three optical laser systems to be installed at the HED instrument:

- Short-pulse ultrahigh-intensity optical laser (UHI-OL):
  ~ 100 TW
- Long-pulse high-energy optical laser (HE-OL):
  ~ 100 J / 10 ns
- Pump–probe optical laser (PP-OL):
  ~ 3 mJ / 15 fs and ~ 100 mJ / 0.8 ps

Table 5-1 summarizes the laser parameters for the start of operation of the HED instrument. Future upgrade plans include installing a petawatt-class UHI-OL (~ 30 J / 30 fs) and a kilojoule-class HE-OL (~ kJ / ns). The layout and design of the experiment and laser areas described in this TDR are based on the requirements for the start of operations, but in several cases room is provided to include future upgrades. The UHI-OL will be a commercial Ti:sapphire laser, while the HE-OL will be a custom-built diode-pumped laser system developed by the Central Laser Facility (CLF) operated by the UK Science and Technology Facilities Council (STFC) and installed through a UK collaboration (DiPOLE project). Both of these lasers will be external contributions to the HED instrument at European XFEL within the framework of the HIBEF UC.

Table 5-1. *Parameters of the optical laser systems to be installed at the HED instrument for the start of operations*

Laser type	Basic properties on sample	Pulse duration	Beam diameter before focus	Spot size on sample
UHI–OL	λ = 0.8 µm / 3 J / 10 Hz	30 fs	10 cm circle	3 to 10 µm Airy pattern
HE–OL	λ = 1.03 µm / ~ 100 J / 1–10 Hz	2–20 ns flat-top or t^3-ramped profile	7 x 7 cm^2 square	50–500 µm spatially smoothed flat-top profile
PP–OL I	λ ~ 0.8 µm / ~ 3 mJ / 0.2–4.5 MHz intraburst	15–100 fs	3–5 cm	3–300 µm Airy pattern
PP–OL II	λ ~ 1 µm / ~ 100 mJ / 200 kHz intraburst	0.8 ps / 500 ps	3–5 cm	3–300 µm Airy pattern

5.1 Pump–probe optical laser (PP-OL)[a]

The PP-OL system [21] is currently being developed by the Optical Lasers group (WP78) at European XFEL. The PP-OL uses an optical parametric chirped pulse amplifier (OPCPA) in a non-collinear optical parametric amplifier (NOPA) configuration [22], pumped by frequency-doubled (515 nm), 800 fs laser pulses. The pump pulse, with a fundamental wavelength of 1030 nm, can also be provided to the experiment (mode PP-OL II in Table 5-3). Such a mode of operation will require reconfiguring several mirror optics in the PP-OL beam transport in order to accommodate the transport of different-wavelength OL radiation. The PP-OL will be used for optical probing, for sample excitation, and as a timing reference with respect to the X-ray beam. The PP-OL system at SASE2 will be shared by the MID and HED instruments.

[a] G. Palmer of the Optical Lasers group (WP78) contributed significantly to this section.

5.1.1 Applications using the PP-OL

Foreseen applications using the PP-OL system at the HED instrument are summarized in Table 5-2. In brief, the PP-OL can be used to probe highly excited matter created by intense X-ray pulses or by high-power laser irradiation. The short temporal duration (15–20 fs) and precisely controlled delays allow for the probing of dynamically changing and non-equilibrium processes. The PP-OL can also be used for the direct excitation of samples and as a timing reference with respect to the X-ray beam, in case of ultrahigh time resolution experiments using the femtosecond PP-OL or UHI-OL lasers.

Table 5-2. *PP-OL parameters required for various applications*

Purpose	Laser energy	Pulse duration	Other
Reflectometry	< 1 mJ	15 fs (shortest)	*p*-/*s*-polarization ω *and* 2ω (< 0.6 mJ)
FDI	≤ 1 mJ	Shortest or chirped mode: 100 fs – 10 ps	ω and 2ω, *p*-/*s*-polarization
Excitation of solids	Up to 5 mJ	15–500 fs	
Shock compression	≥ 100 mJ	> 0.5 ps	Mode PP–OL II
Synchronization with X-rays	~ 1 µJ	Short	Supercontinuum generation

5.1.2 Operation modes

The fundamental parameters of the PP-OL for different operation modes are summarized in Table 5-3. For each operation mode, the pulse pattern can be arbitrarily chosen, selecting one or a few pulses in the burst by means of pulse pickers installed in both the 800 nm NOPA and the 1030 nm pump amplifier.

Table 5-3. Operation modes and corresponding laser parameters of the PP-OL system

Mode	Repetition rate in 10 Hz burst	Max. energy / pulse [mJ]	Pulse duration	Wave-length [nm]	Spectral bandwidth [nm]	Pulse on demand
PP-OL I-a	4.5 MHz	0.2	15 –~ 100 fs in discrete steps	~ 800 nm	~ 10–60 nm, depending on the pulse duration	Yes
PP-OL I-b	1 MHz	1				
PP-OL I-c	0.2 MHz	3–5				
PP-OL II-a	4.5 MHz	4	0.8 ps or 0.5 ns	~ 1030 nm	~ 3 nm	Yes
PP-OL II-b	1 MHz	20				
PP-OL II-c	0.2 MHz	100				

5.1.3 PP-OL beam transport

The schematic layout of the PP-OL beam transport is shown in Figure 5-1.

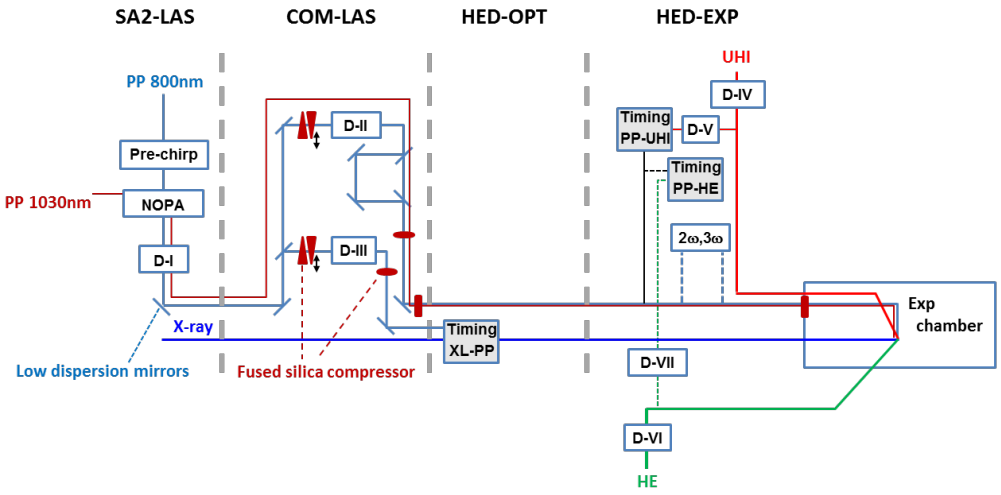

Figure 5-1. Schematic layout of the PP-OL beam transport through different hutches. SA2-LAS: PP-OL laser, COM-LAS: instrument laser configuration, HED-OPT: HED optics, HED-EXP: HED experiments. D-I, D-II, D-III, etc. denote the various optical delay lines.

5.1.3.1.1 SA2-LAS hutch

The PP-OL system (front end, amplifier, and pre-compressor) is located inside the PP-OL laser room (SA2-LAS). An ultrastable fibre seed laser is synchronized to the general European XFEL synchronization network. Following a fibre-based pre-amplifier, the beam is split into two branches: one for a chirped seed pulse and a second for amplification. The amplification pulses (λ = 1030 nm) can either be sent directly to the experiment (max. ~ 100 mJ, mode PP-OL II) or frequency-doubled to pump the 800 nm pulse through a NOPA (mode PP-OL I). Depending on the required energy and repetition rate, up to three NOPA stages will be employed.

5.1.3.1.2 COM-LAS hutch

After amplification, the PP-OL beam is transported to the instrument laser hutch (COM-LAS), which is shared by the MID and HED instruments. In COM-LAS, the OL pulses will be compressed, attenuated, and delayed according to the experimenters' specifications (see Figure 5-2).

Beam splitting into a pump–probe branch (PP line) and a timing branch (timing line) is also performed inside COM-LAS. Different energy splitting ratios are possible. At the exit from COM-LAS to HED-OPT, a radiation shielding chicane will be installed to prevent X-ray radiation leaking from HED-OPT into the laser room.

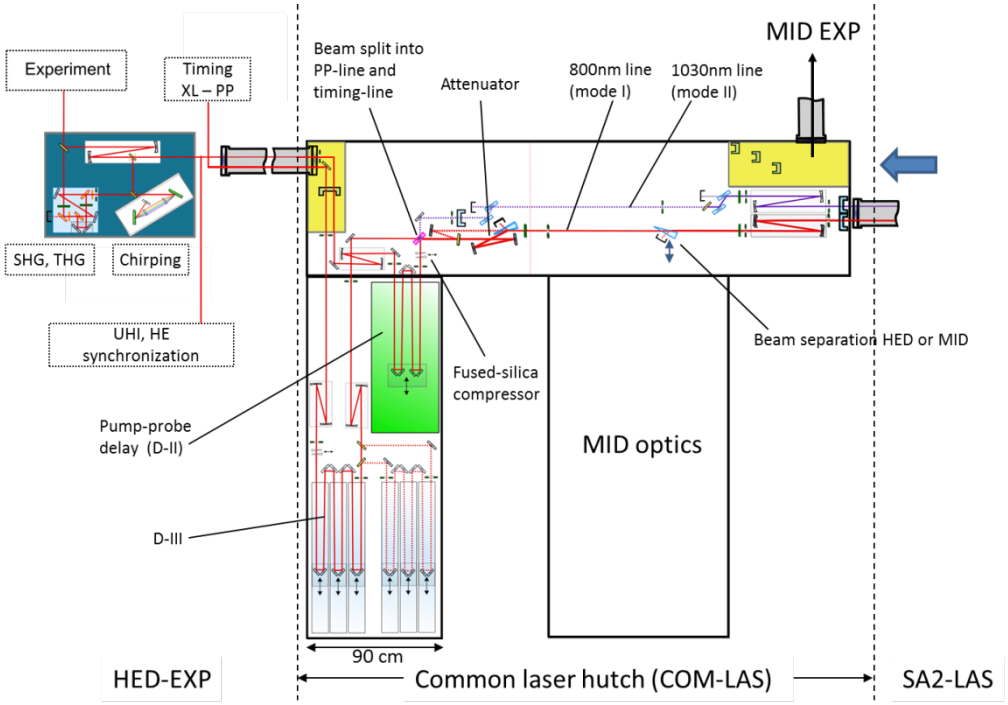

Figure 5-2. *Layout of the inside of the common laser hutch (COM-LAS). This hutch allows modifications of the pulse, e.g. compression, attenuation, beam splitting, and delay. Red beam path: 15–100 fs (λ ~ 800 nm) short pulses. Purple beam path: long pulses (λ = 1030 nm, 800 fs or 500 ps). The optical table height is 90 cm and the optical beam height is 1.05 m. The beam is split into two arms, the PP line and the timing line. At the exit of COM-LAS towards HED-OPT, the height of the timing-line beam is changed to 1.40 m by a periscope using two mirrors without angle adjustment. Reflective mirrors are equipped with low-dispersion and high-reflectivity coatings (R = 0.9975 at 45° incidence).*

5.1.3.1.3 *HED-OPT hutch*

The PP and timing lines are sent into separate OL beam transports with separate vacuum pipes. Separation is done inside COM-LAS, and both tubes cross the wall and have separate locations inside HED-OPT (Figure 5-3). The timing-line beam is brought to a setup on an optical table inside HED-OPT for arrival time and jitter measurement with respect to the X-ray beam. This permanent installation will allow the timing jitter to be recorded for each shot (for details, see Section 6.1, “X-ray–optical arrival time monitor”).

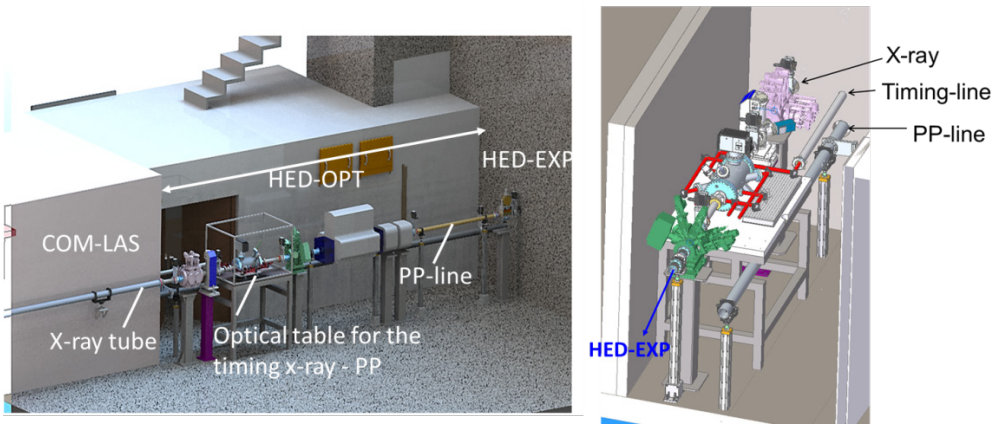

Figure 5-3. *HED-OPT room.* Left: *X-ray beam comes from the left.* Right: *X-ray beam comes from the upper right. There are two vertically separated vacuum tubes for the PP-OL transport. The upper one (timing line) is for time referencing, while the lower (PP line) transports the PP-OL pulses for pump–probe experiments to HED-EXP.*

5.1.3.1.4 HED-EXP hutch

Only the PP line enters HED-EXP. The beam height at the entrance to HED-EXP is 1.05 m. A periscope is installed to bring the beam to the height of the X-ray beam (1.40 m). A radiation shielding chicane to prevent leaking of X-ray radiation, either from HED-OPT to HED-EXP or vice versa, needs to be installed at the interface of the two hutches. Its design is under way. The PP-OL beam can be either sent directly to the experiment chamber IA1 or brought first to an optical table, where the frequency doubling or tripling setups are located. A fraction of the PP-OL energy is split off before entering the experiment chamber and will be used for timing synchronization with the UHI-OL and HE-OL.

5.1.3.2 Beam diameter and transport tube size

For the PP line, the beam diameter at highest energy mode (mode PP-OL I-c or PP-OL II-c in Figure 5-3) is expected to be ~ 30 mm, and three-inch diameter mirrors will be used. The beam is delivered via DN100 vacuum tubes to avoid dispersion and B-integral increase by air (a pressure of ≤ 1 mbar is sufficient). At the vacuum tube entrance and exit, a 4 mm thick UV-grade fused silica window with an effective aperture of 60 mm will be placed. The total length of the vacuum transport is ~ 10 m, which needs to be segmented into several tubes. For the timing line, the beam diameter is less

than 10 mm due to the low pulse energy. This beam is transported in a DN63 tube with a total length of ~ 3 m.

5.1.3.3 Pulse duration, compression, and centre wavelength tuning

For the mode PP-OL I (λ ~ 800 nm), various pulse durations in the range of 15 to ~ 100 fs (in discrete steps) can be selected by tuning the bandwidth. For each setting, the pulse will be transform-limited (lower limit of the pulse duration for a given spectrum), thus there will be no chirp. The bandwidths for the NOPA pulses are 35 nm, 20 nm, and 13 nm for 25 fs, 50 fs, and 75 fs durations, respectively. Even longer pulse durations up to > 10 ps can be provided by a chirped grating, which will be located on the optics table inside HED-EXP.

For the mode PP-OL II (λ ~ 1030 nm) with highest possible energies up to ~ 100 mJ, pulse durations of 800 fs (compressed) or 500 ps (uncompressed) are provided.

The pulse compression strategy relies on a specific dispersion management scheme, where a set of chirped mirrors imposes a negative chirp on the pulse, so that any dispersive optical component inducing positive dispersion (e.g. lenses, windows, etc.) along the PP-OL beam propagation is compensated. The expected pulse duration at the entrance of COM-LAS is 300–500 fs, and a conjugated set of fused silica wedges can be used to recompress back to the initial pulse duration before the chirped mirrors. The total thickness of fused silica required during the beam propagation will be on the order of 30–40 mm.

For the mode PP-OL II, no stringent dispersion management is required due to the narrow bandwidth. The pulse is compressed inside SA2-LAS, resulting in 0.8 ps pulse duration. Users may also need a non-compressed chirped pulse, which will have 0.5 ns duration.

5.1.3.4 Delay lines

Three optical delay lines are required to adjust the beam overlap, one before splitting into the timing and PP lines (D-I) and two after splitting for each of the lines (D-II and D-III, Figure 5-1). D-I is used to compensate the optical path

difference between the X-ray and PP-OL pulses, and will be used further for long-term drift compensation. Path differences longer than 5 ns have to be achieved electronically by phase-shifting the seed oscillator. D-II is for the PP line and will be used for pump–probe scanning during experiments. This delay is independent from the timing line; therefore, changing D-II does not affect the X-ray to PP arrival jitter measurement. The current optical layout allows delays up to ~ 10 ns. If delays longer than 10 ns are required by experiments, the entire PP-OL timing needs to be changed by means of an electronic phase shifting of the seed oscillator signal. In this case, the time reference with respect to the X-ray beam arrival will be lost. D-III is for the timing line and is required to compensate path differences between the PP and timing lines for varying experiment setups. Once this delay has been set at the beginning of an experiment, and the experimental setup is not changed, D-III does not need to be touched during operation.

For the delay lines, we plan to use linear translation stages with 150 nm steps allowing < 5 fs steps after four bounces. This value is 2–4 times smaller than the expected temporal resolution with the arrival time monitor (see Chapter 6, “Arrival time monitor”).

5.1.3.5 Attenuator

The continuously variable attenuator inside COM-LAS consists of a remotely controlled half-wave plate in combination with a polarizing prism. For the shortest pulse duration of 15 fs (i.e. the largest bandwidth), the coating must allow for a low dispersion. The current design has been tested by the Optical Lasers group, showing the contrast to be better than 100:1 (see also Figure 5-4). Pulse energy losses of ~ 15% have to be expected. To provide 100% pulse energy transmission, the attenuator will be removable from the PP-OL beam path.

5.1.3.6 Frequency conversion

In HED-EXP, before entering the interaction chamber, the beam can be frequency-doubled (400 nm) or -tripled (266 nm) by means of non-linear crystals (beta barium borate: BBO) and complementary optics. 50 x 50 cm^2 space is reserved on the optical table inside HED-EXP for this purpose.

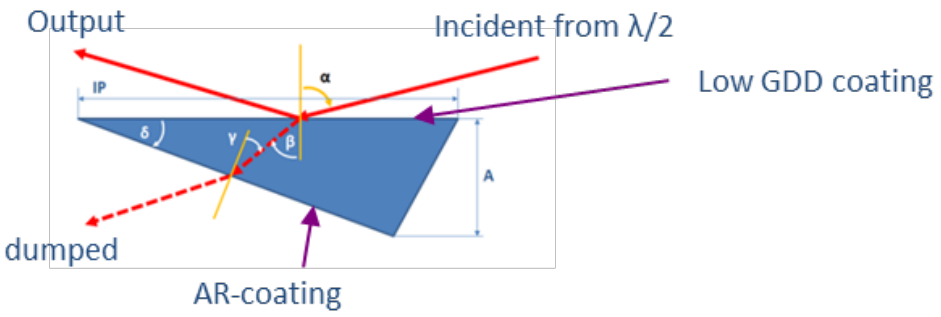

Figure 5-4. *Sketch of continuously variable attenuator design, which consists of a low group delay dispersion (GDD) polarizer with 75° angle of incidence (angle α in the figure). Working range: 700–900 nm. Courtesy of G. Palmer of the Optical Lasers group.*

5.1.3.7 Chirping

For experiments employing FDI diagnostics in chirped mode [4], it is required to provide a chirped PP-OL beam. Up to a few 10 ps pulse durations are planned to be provided, and a 50 x 50 cm^2 space is reserved for this purpose on the optical table inside HED-EXP.

5.1.3.8 Beam splitting for FDI diagnostics

FDI diagnostics using a non-chirped PP-OL beam (see Section 8.3.1, “Fourier domain interferometer (FDI)”) [5] provides better temporal resolution than the chirped-mode FDI. This mode requires beam splitting with fixed delay to generate two temporally separated collinear pulses. This beam splitting should occur after D-II.

5.1.3.9 Beam focusing

At maximum energy and shortest pulse duration (both modes PP-OL I and II), the B-integral gets close to unity following transmission through a focusing lens. Therefore, focusing is better done by means of reflective optics. On the other hand, using PP-OL as a probe in general does not require high pulse energies, thus lens focusing will be the better option as it provides higher flexibility, e.g. in choosing incidence angles. Both focusing options will be provided for PP-OL inside HED-EXP.

5.1.3.10 Online monitors

Several performance parameters of the PP-OL beam delivery will be monitored online, will be saved, and can also be used in feedback loops to adjust laser settings. One important example is long-term drifts of the PP-OL beam pointing. Some of the mirrors in the beam transport system are also remote-controlled to allow for the implementation of drift compensation, either manually or through automated algorithms. Other important parameters, like pulse energy, beam shape, and spectrum, will also be monitored online.

5.1.4 Vacuum system and chicane

The two PP- and timing-line beams are transported in vacuum to avoid dispersion and B-integral increase in air. For this purpose, a vacuum level of ≤ 1 mbar is sufficient. Due to relatively small volume to be pumped (~ 0.01 m^3) and the relaxed vacuum requirements, this vacuum section does not need to be connected to scroll pumps or turbo pumps, but can be pumped by a diaphragm pump. At least one vacuum gauge will be fitted to each transport to monitor the pressure.

The overall layout of the vacuum system for the HED instrument is summarized in Section 4.7.7, “Vacuum system”.

5.2 Ultrahigh-intensity optical laser (UHI-OL)

At the HED instrument, a 100 TW–class short-pulse laser will be installed, funded through the HIBEF UC. This system will be a commercial Ti:sapphire laser system based on the chirped pulse amplification (CPA) technique. Combined with the X-ray FEL beam, it provides users with a world-class, unique platform to study plasma physics in the relativistic regime.

In this section, we review the requirements for this laser system and provide a brief description of state-of-the-art optical laser techniques to achieve these requirements. The final implementation still needs to be defined and will occur in the course of 2014.

5.2.1 Temporal contrast control

For most experiments requiring the use of the UHI-OL, the ionization and damage thresholds are very important parameters leading to strict requirements for the UHI-OL pulse delivery, in particular in terms of temporal pulse contrast. The ionization threshold is intensity-dependent and corresponds to the ionization of the atomic species present in the target and the production of a plasma. For example, the ionization threshold is close to 10^{12} W/cm^2 for metals and close to 10^{13} W/cm^2 for dielectric materials. The generation of a plasma near the target surface due to ionization before the peak intensity of the UHI-OL pulses (pre-plasma) modifies the electron density gradient of the target. This effect will change the nature of the laser absorption processes by the target. The damage threshold is fluence-dependent (energy per surface: J/cm^2); it affects the energy absorption process and may damage or destroy the target, such as thin foils.

While the requirements for temporal contrast depend on the experiment details, the HED instrument aims at a very high temporal contrast ratio (laser pulse peak intensity to pre-pulse or pedestal intensity), ideally better than 10^{12}, which corresponds to the present state of the art (Figure 5-5).

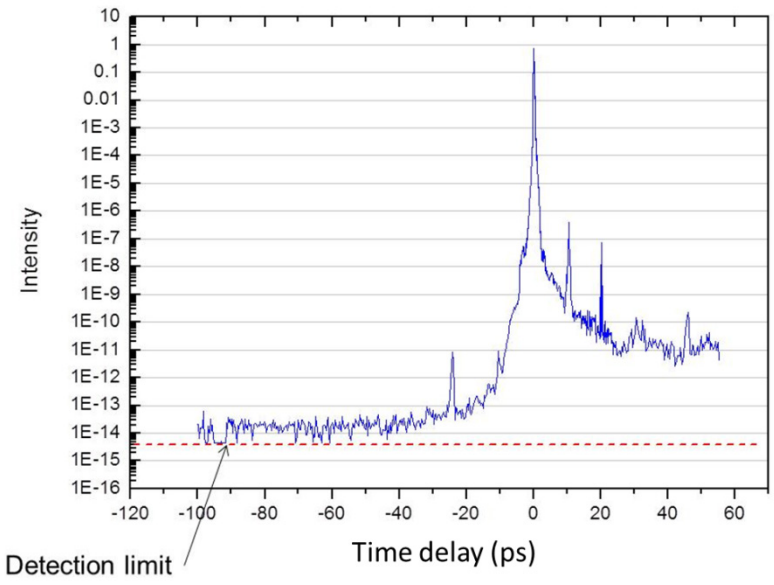

Figure 5-5. *Temporal profile of an UHI-OL pulse indicating the achievement of ultrahigh temporal contrast. Courtesy of Amplitude Technologies in Evry, France.*

The architecture of a typical laser system based on CPA technology is shown in Figure 5-6. Typically, these lasers consist of an oscillator, a grating-based pulse stretcher, several amplification stages to reach the final pulse energy, and a grating compressor to restore the short laser pulse duration. These lasers typically do not exceed a contrast ratio much better than 10^{-6} without employing additional measures (Figure 5-7). Pre-pulses on the nanosecond time scale are generated in the oscillator or a regenerative amplifier cavity. The time delay between the pre-pulses and the main amplified pulse is given by the round trip time inside the regenerative cavity (several nanoseconds); the first pre-pulse exits the cavity before the main pulse with one less round trip. The typical energy ratio between the maximum energy of the amplified pulse and the first pre-pulse is in the range of 10^{4}. Often, fast Pockels cells are implemented after the regenerative amplifiers to remove the pre-pulses (Figure 5-8). In addition, amplified fluorescence produced by the pumped crystal during the amplification process, called amplification of spontaneous emission (ASE), produces a plateau-shaped nanosecond pedestal.

For temporal contrast enhancement, several techniques were developed over the past years. In the following, we describe the methods that we intend to implement for the UHI-OL system at the HED instrument.

A first measure is to implement a saturable absorber in a specific booster amplifier. This contrast ratio booster amplifier consists of a compact multi-pass amplifier to amplify the oscillator output up to the microjoule level. The pulses are then cleaned by a saturable absorber removing the residual ASE background of the oscillator pulses before stretching and then seeding the next amplifier. This technique alone can reach a contrast ratio of 10^{-8} to 10^{-9}.

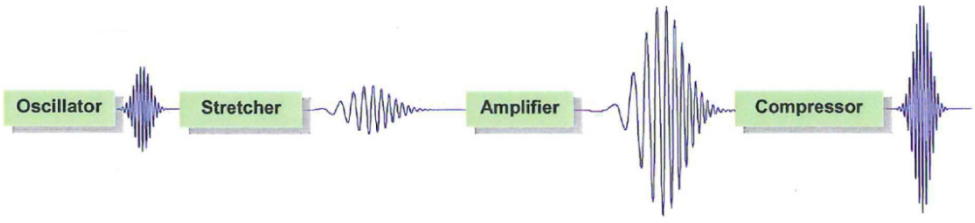

Figure 5-6. *Scheme of an UHI-OL system based on the CPA technique*

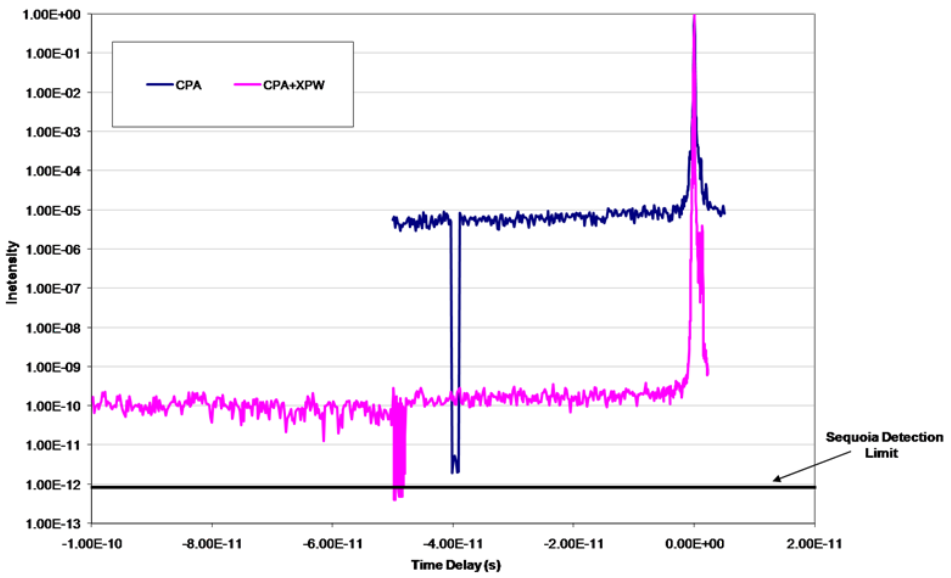

Figure 5-7. *Temporal contrast ratio measurement of a 100 TW Ti:sapphire laser, with (purple line) or without (blue line) applying the cross-polarized wave generation technique (XPW) to improve the temporal contrast. Courtesy of Max Born Institute (MBI) in Berlin, Germany.*

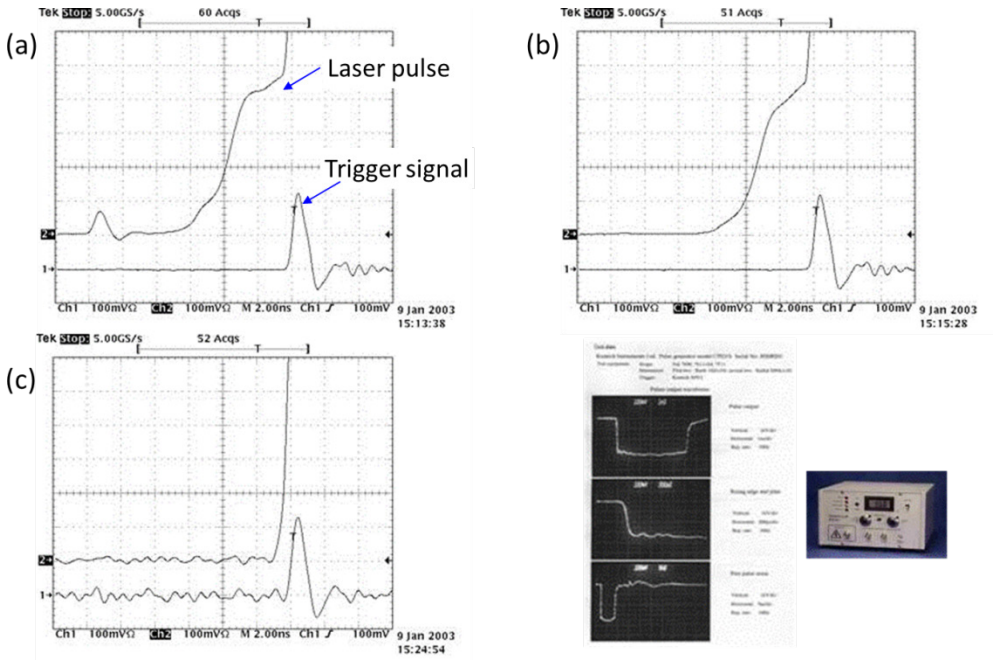

Figure 5-8. *Temporal contrast enhancement using a fast Pockels cell. From (a) to (c), the switching timing of the Pockels cell is moved towards the main pulse (the main pulse itself is saturated in the figure). From (a) to (b), the pre-pulse from the regenerative amplifier is cut. From (b) to (c), the hump in front of the main pulse is cut. Courtesy of STFC, Daresbury Laboratory, in Daresbury, UK.*

To improve this ratio, double CPA systems were introduced, where the laser pulses are stretched and amplified to the millijoule range, temporally compressed and cleaned using cross-polarized wave (XPW) generation, stretched again, and then amplified. This technique improves the contrast by a further four orders of magnitude and, additionally, broadens the spectrum (Figure 5-9). Using a combination of these methods, a temporal contrast ratio of 10^{-12} can be achieved.

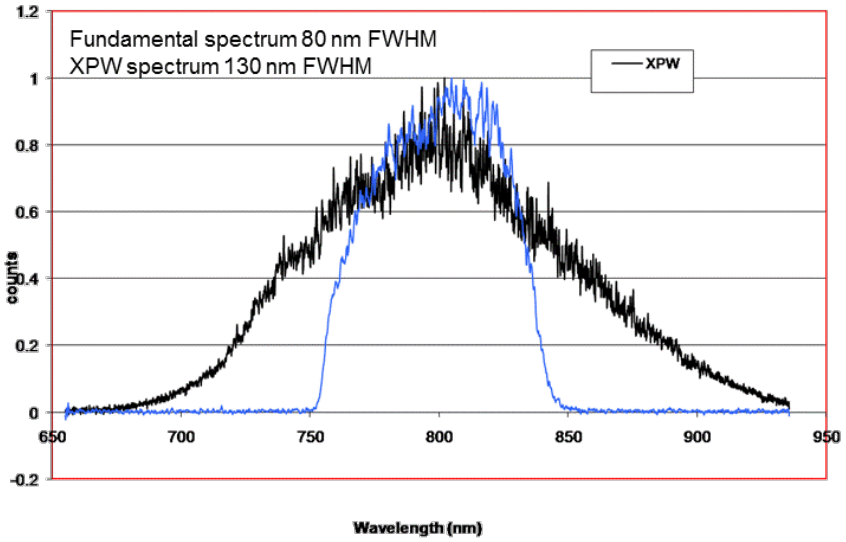

Figure 5-9. *Spectrum of the laser before and after XPW generation. Courtesy of MBI.*

To further improve the temporal contrast, one could use a plasma mirror setup, after temporal compression (Figure 5-10), where the ASE will be transmitted through a glass plate until it creates an overcritical-density plasma at the leading edge of the main pulse, reflecting the main pulse. Although the technical details of plasma mirror systems were well established in previous decades, the implementation of a plasma mirror at the HED instrument is not clear because of the instrumental complexity and space constraints. A vertically oriented design of a double plasma mirror system, as implemented at Max Born institute (MBI) in Berlin, Germany, could be one option to mitigate the space requirement (Figure 5-10, right). UHI-OL systems applying all these techniques together have demonstrated a contrast ratio better than 10^{14} (see Figure 5-5).

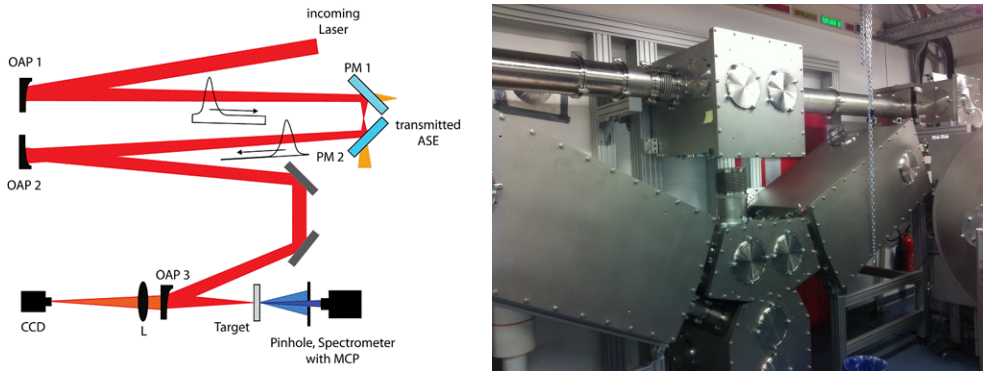

Figure 5-10. *Schematic of a double plasma mirror setup (left) and a newly developed vertical design (right, courtesy of MBI)*

5.2.2 Pulse energy

The compressed pulse energy should be on the order of 4 J on the sample, which will enable an intensity of more than > 10^{20} W/cm^2.

5.2.3 Pulse duration

An acousto-optic programmable dispersive filter (AOPDF) or an acousto-optic programmable gain control filter (AOPGCF) will be used to control the spectral phase distribution of the pulse and to compensate for gain narrowing that occurs in the different amplification stages. Routinely achieved pulse durations after the compressor are below < 25 fs.

5.2.4 Synchronization with the X-ray pulse

The UHI-OL will be referenced to the synchronization network at the European XFEL. For this purpose, the Ti:sapphire oscillator (master oscillator) of the UHI-OL will be optically synchronized to a SESAM-based mode-locked laser oscillator (Origami-15). The Ti:sapphire oscillation operates at a 81.25 MHz repetition rate, which is 1/16 of the master clock (1.3 GHz, RF) and generates the 800 nm laser pulses with typical initial pulse durations of < 10 fs and several 100 nm spectral bandwidth. The Origami-15 oscillator emits soliton pulses with a duration of 200 fs at a repetition rate of 1/6 of the master clock (~ 216 MHz) and will be distributed around the facility and inside the experiment hall. The Origami-15 itself operates at 1550 nm because, in the telecommunication wavelength range, beside standard components, dispersion-compensating optical fibres are state of the art.

The Origami-15 is synchronized to the accelerator RF oscillator with a timing jitter of less than 5 fs (rms).

5.2.5 Specifications of the UHI-OL system

Table 5-4 summarizes some of the requirements for the UHI-OL system for the HED instrument.

Table 5-4. *Specifications of the UHI-OL*

Pulse duration		< 25 fs	On sample, including active spectral phase and/or spectral control
Pulse energy		2–4 J / 10 Hz	On sample
Long-term energy stability		< 1.5% rms	1 h compressed beam at full energy
Pulse-to-pulse stability		< 1.5% rms	3 min
Contrast	< 100 ps	$< 10^{-12}$	Including measurement device
	< 10 ps	$< 10^{-10}$	
	< 5 ps	$< 10^{-8}$	
	< 1 ps	$< 10^{-5}$	
	(ns) pre-pulse	$< 10^{-10}$	
Strehl ratio after compression		> 0.7	Without adaptive mirror
		> 0.9	With adaptive mirror
Pointing stability < 1 µrad			

5.2.6 UHI-OL beam transport

Considering a planned focal spot size on sample of ~ 3 µm, a high degree of pointing stability needs to be achieved for the UHI-OL beam transport. In this context, a careful design of mirror supports has been performed.

A schematic drawing of the UHI-OL beam transport from the compressor grating chamber to the sample chamber is shown in Figure 5-11. Two motorized mirrors inside the compressor chamber (MU1, MU2) define the exit axis of the beam. The first turning mirror after the compressor (MU3) brings the UHI-OL beam down to the experiment room. The first mirror inside HED-EXP (MU4) is attached to the concrete wall and brings the beam directly

into the main experiment chamber. MU3 and MU4 are optimized for stability and do not have motorized controls. Inside the experiment chamber, there are two more motorized mirrors (UM5, UM6) before the beam impinges on the focusing off-axis parabola (OAP) mirror.

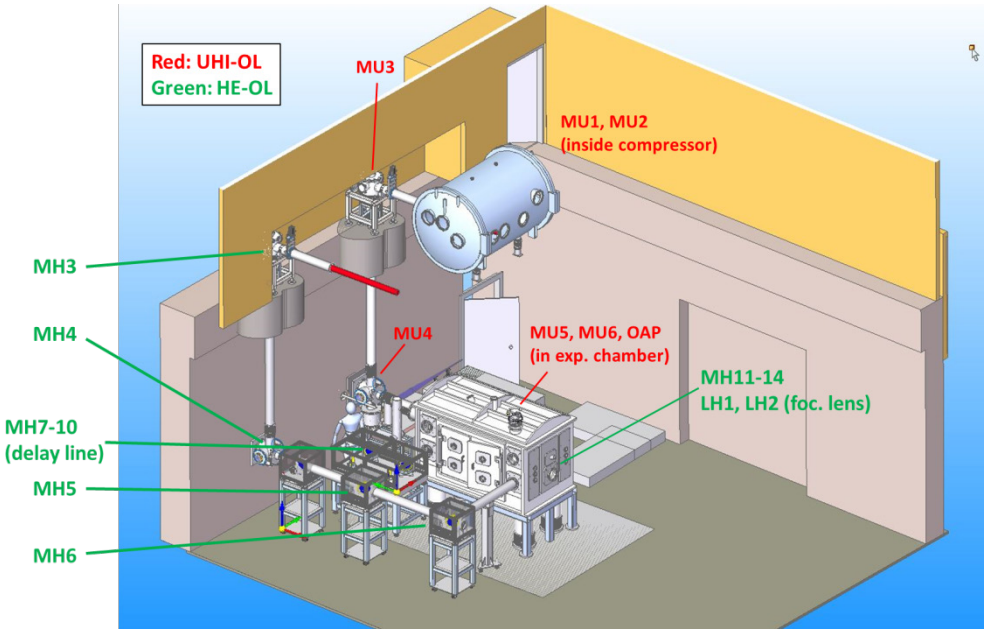

Figure 5-11. *Schematic of the HED laser transport. Red beam: UHI-OL. Green beam: HE-OL. Both beams are brought down from the laser hutch (HED-HPLAS).*

5.2.6.1 Transport mirror support design

Careful mechanical design of the mirror support is crucial to achieve the stringent pointing stability. All structures have resonance frequencies. A vibration test of the experiment hall (XHEXP) performed in 2013 found that the HED-EXP floor and roof have an extremely high level of vibrational stability (VC-E level). The resonant frequencies are around 1–30 Hz. Therefore, the mirror supports were designed such that their resonant frequencies are far higher than 30 Hz.

Figure 5-12 shows the mechanical design for the MU3 turning-mirror chamber. The resonant frequencies were simulated using ANSYS software and revealed a first vibrational mode at 150 Hz, i.e. far higher than the resonant frequency of the floor. The mirror support is mechanically decoupled from the vacuum chamber. Therefore, the deformation of the structure by vacuum pumping does not affect the mirror alignment.

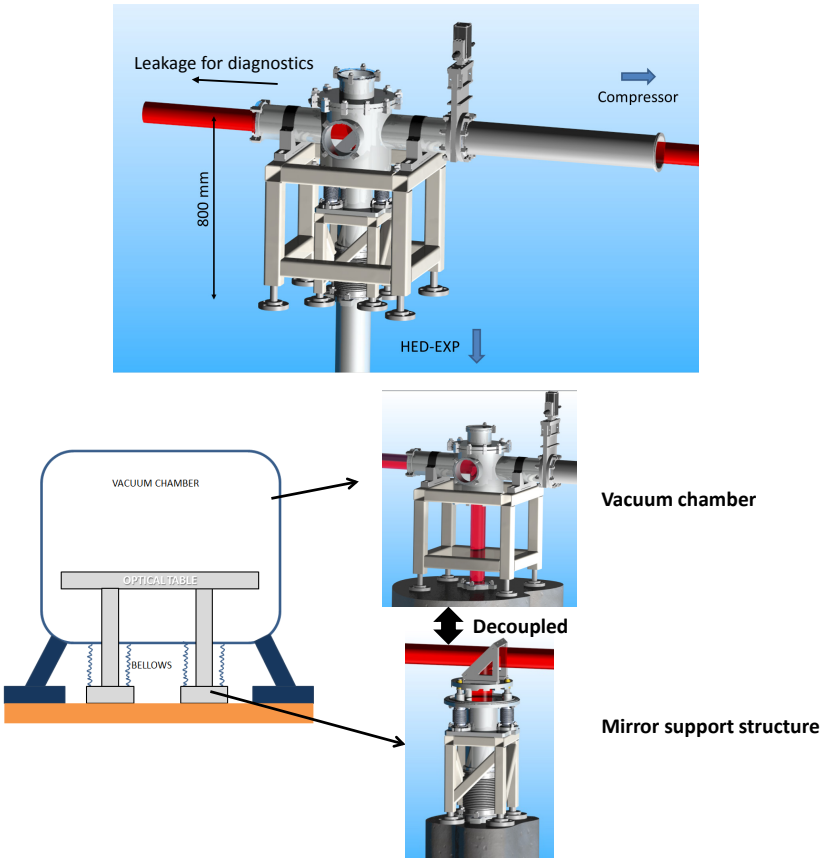

Figure 5-12. *Mechanical design for the turning-mirror support chamber right after the compressor (MU3). The mirror support itself is mechanically decoupled from the chamber. The size of the chamber is DN320 with a DN160 tube for the beam transport. The first vibrational mode is 150 Hz.*

The mechanical design of the MU4 mirror support is shown in Figure 5-13. The support is directly attached to the HED-EXP enclosure wall. The first vibrational mode is 396 Hz. The leakage through this mirror is used for beam characterization.

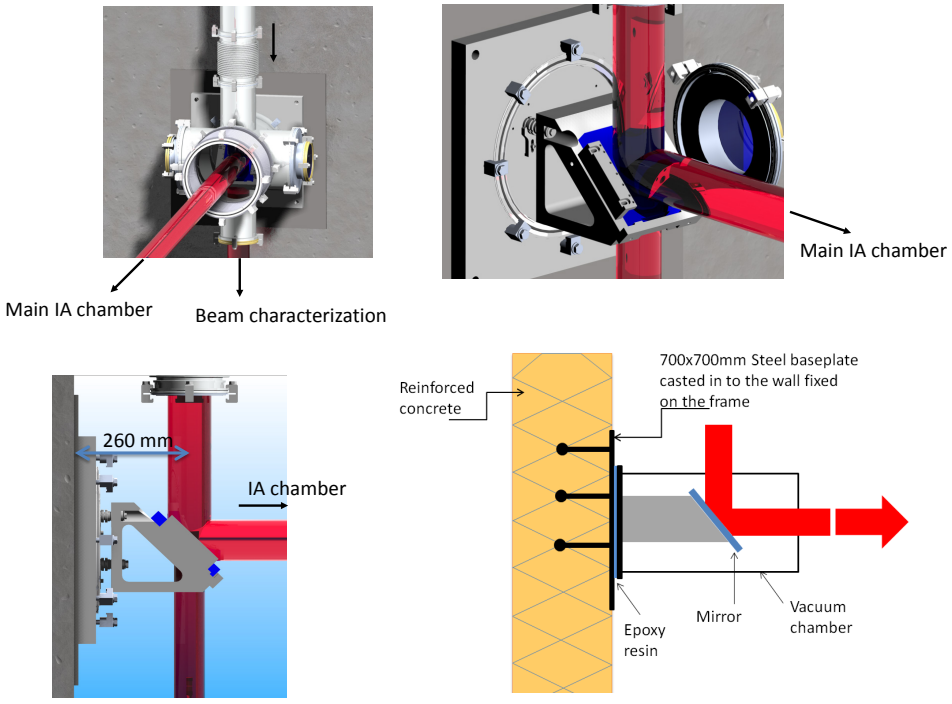

Figure 5-13. *Mechanical design for the final turning-mirror support before the main interaction chamber IA1 (MU4). The support is directly attached to the experiment enclosure wall. The first vibration mode is 396 Hz. The leakage through this mirror is used for beam characterization.*

5.2.6.2 Beam transport inside the experiment chamber

The size of the main experiment chamber (IA1) is 2.5 x 1.3 m^2, with its long axis parallel to the X-ray beam. As shown in Figure 5-14, the HED instrument provides experimenters with a choice in the focusing axis for the UHI-OL from near-collinear to orthogonal with respect to the X-ray beam. The exact collinear focusing, i.e. along the X-ray beam axis, will not be provided due to the need to use a hole for the X-ray beam in the off-axis parabola (OAP) mirror. The smallest angle of incidence is about 13° from the X-ray beam. The relative position between OAP and MU6 may be fixed and can be rotated around the sample to provide different focusing axes. This setup would allow for a minimization of the effort required to change the setup between experiments.

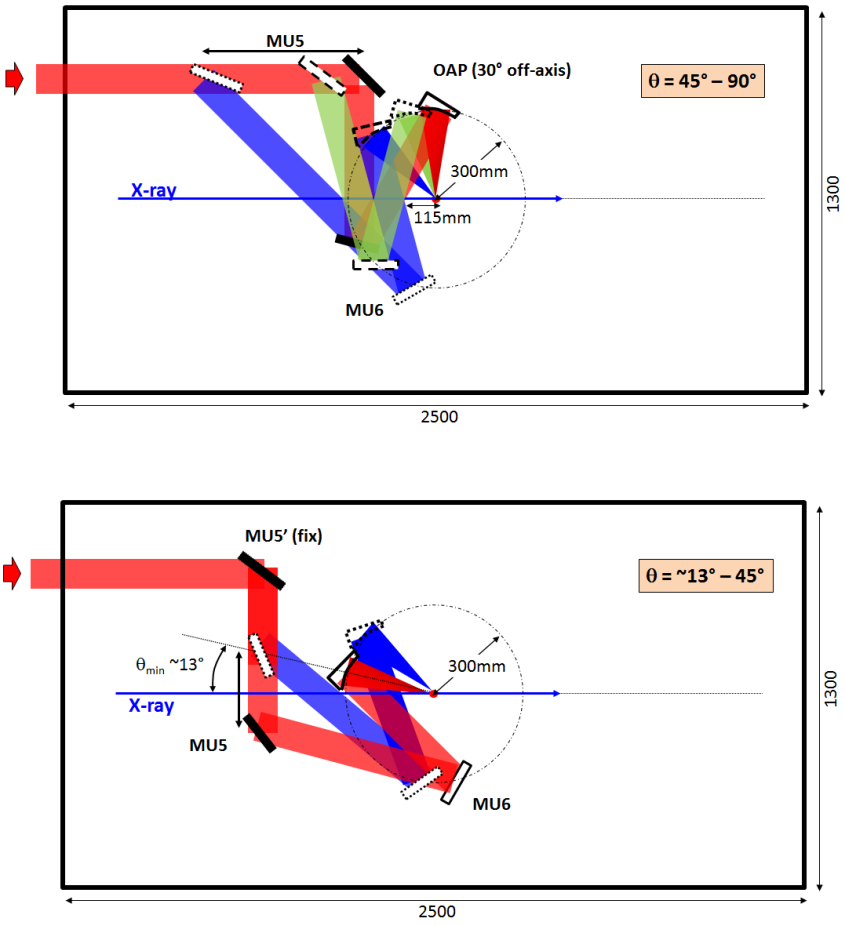

Figure 5-14. *UHI-OL transport inside the interaction vacuum chamber. The UHI-OL beam comes from the left (east) quasi-parallel to the X-ray beam. The final turning mirror (MU6) and the focusing parabola mirror (OAP) can be rotated around the sample to provide flexible choice in focusing axis angle θ. Quasi-collinear (~ 13°) to orthogonal focusing with respect to the X-ray beam is provided.*

The details of the chamber geometry and the arrangement inside will be discussed in Chapter 7, *"*Experiment chamber setups*"*.

5.2.7 Remote online control of UHI-OL parameters

Several laser parameters may need to be controlled, monitored, and adjusted during operation of an experiment. These parameters need to be remotely controllable by the laser operators and users and will be accessed through Karabo, the European XFEL's software framework.

In the following, we introduce the techniques to be employed to measure and adjust several of these parameters.

5.2.7.1.1 Pulse energy control / attenuation

The UHI-OL pulse energy needs to be remotely controlled during operation. Two methods will be used for this purpose. The first method uses an optical wave plate and a polarizer pair and can achieve an optical density (OD) of ~ 1.5. The second method uses a pair of (anti-reflection) glass plates with an OD of 1.5–3 per plate for a total of four plates. The maximum attenuation level is better than OD ~ 6 (10^6). The beam energy on sample at the maximum attenuation is at the microjoule level while the UHI-OL runs fully amplified. Using this attenuation, e.g. focal spot characterization using a microscope objective or temporal contrast measurement can be performed with all amplifiers running. Since the amplification process does affect the temporal contrast and spatial beam profile, the capability of having high attenuation is critical for adequate diagnostics of the laser performance.

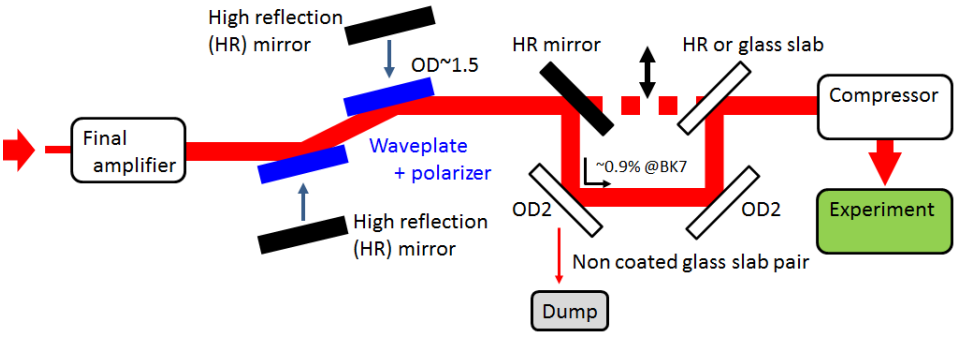

Figure 5-15. *UHI-OL attenuation scheme after the final power amplifier before the compressor*

The attenuators will be installed after the final amplifier but before the vacuum compressor to prevent accumulation of B-integral and additional high-order dispersions after compression. The attenuation setup consists of wedges, half-wave plates, and polarizers with an optical quality of $\lambda/10$, the combination of which exhibits a maximum attenuation of ~ 97% (OD 1.5) without influencing the transmitted spectrum and polarization purity. The wave plate/polarizer attenuator could be replaced with a high-reflectivity (HR) mirror setup to maximize the throughput. Higher attenuation is given by inserting non-coated BK7 glass slabs, each slab giving 0.9% reflectivity at 45° incidence angle for *p*-polarization for 800 nm. Even stronger attenuation can be achieved by slightly shifting the incidence angle toward the Brewster angle

(~ 56° from the normal). Two or three glass slabs will be installed to reach > OD 6 attenuation.

5.2.7.2 Focal-spot characterization

To characterize the focused beam quality, a microscope objective will be placed close to the sample position. The objective is fixed on high-precision *xyz* stages (see Figure 5-16) and needs to be removed from the interaction point during high-power shots.

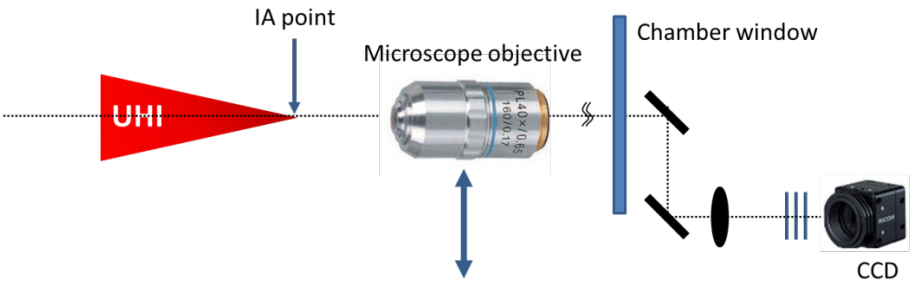

Figure 5-16. *Focal-spot characterization using a microscope objective at the sample point*

The following items describe online diagnostics that should be permanently installed and operable. The data of these monitors will be delivered and recorded automatically for each laser shot.

5.2.7.3 Pulse energy monitor

The laser pulse energy will be measured in front of and behind the compressor by leakage of a part of the pulse energy through a turning mirror. The throughput of the compressor needs to be calibrated and requires regular verification.

5.2.7.4 Wavefront monitor and focal-spot optimization

A deformable mirror setup located before the compressor in combination with a wavefront sensor can correct the wavefront error in order to achieve a Strehl ratio of better than 0.9. As a prerequisite, the commercial UHI-OL system should be designed for a Strehl ratio of > 0.7 without this adaptive mirror. The additional wavefront distortions and aberrations due to compressor gratings and beam transport optics could be corrected using a second deformable mirror.

5.2.7.5 Equivalent plane monitor

An online equivalent plane monitor will allow for the monitoring of the focal spot quality of the beam and beam pointing. We plan to use the leakage from the final mirror before the interaction chamber (MU4) with a reflectivity of 99.9%. Therefore, wavefront distortion of the transmitted beam through MU4 is not an issue (B-integral ~ 0.1). The leakage beam impinges on a receiving glass slab (Figure 5-17). Behind this glass slab, a calorimeter can be placed to monitor the beam energy. The reflectivity of the BK7 glass slab at 45° *s*-polarization incidence is about 10%. The beam energy then reaches around 0.3 mJ, allowing a reduction of the beam diameter. The reduced beam (1–2 cm ∅) is collimated by means of two lenses. The B-integral inside the lens for 0.4 mJ, 30 fs, 10 cm ∅ laser through a 2 cm thick lens is about 0.1. The beam is finally brought up onto the optical table and focused on detectors.

The long-term pointing stability is measured using the above-mentioned system and correctable using the remotely controlled mirrors MU1 and MU2. An active feedback system for long-term stability is also under consideration.

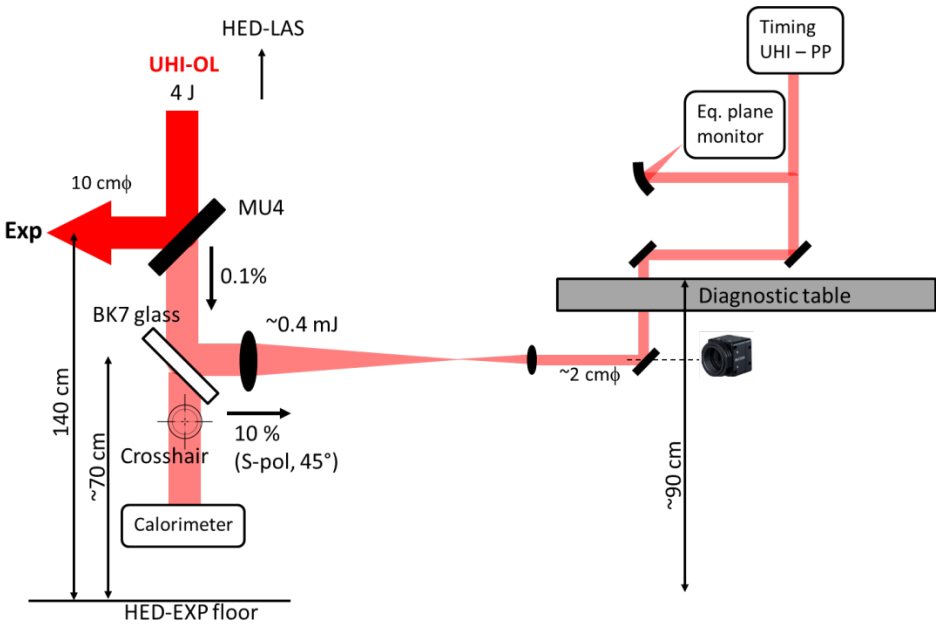

Figure 5 18. *Schematic setup of beam characterization concept using the leakage of the MU4 mirror*

5.2.7.6 Timing measurement

The timing jitter between the UHI-OL pulses and the X-ray beam will be measured online. This measurement involves two cross-correlation measurements of PP-OL vs. X-rays and of PP-OL vs. UHI-OL. Details are described in Chapter 6, *"*Arrival time monitor*"*.

5.3 High-energy optical laser (HE-OL)

The Central Laser Facility (CLF) of STFC Rutherford Appleton Laboratory in Didcot, UK, contributes a 100 J–class diode-pumped solid-state laser (DPSSL) system to the HED instrument within the framework of the HIBEF UC. This laser system is named DiPOLE (Diode Pumped Optical Laser for Experiments) and is the result of an R&D project for high-energy nanosecond high repetition rate lasers. An operational DiPOLE prototype operates with 10 J pulse energy at 10 Hz repetition rate. A first 100 J, 10 Hz system is currently being built on behalf of the HiLASE Center in Dolní Břežany, Czech Republic, and will be installed in 2015 at the ELI Beamlines facility near Prague, Czech Republic. The specifications of the DiPOLE system are summarized in Table 5-5.

Table 5-5. *Specification requirements for the DiPOLE HE-OL system for the HED instrument*

Laser energy	100 J at λ = 1030 nm (minimum), 100 J at λ = 515 nm (desirable), with an energy stability of < 1%
Beam size	75 x 75 mm^2 after the final amplifier
Wavelength λ	Standard operation mode is λ = 515 nm (second harmonic) on sample, using LBO crystals
Repetition	> 1 Hz (minimum), 10 Hz (goal)
Temporal structure	2–20 nm duration at square shape. Temporal pulse-shaping capability for ramped compression experiments (~ t^3 shape) but probably with reduced energy

The DPSSL scheme uses advanced gain media and cooling schemes to overcome the limitations of flashlamp-pumped Nd:glass technology that

exhibit, in general, poor electrical-to-optical efficiency and low repetition rates. The DPSSL technique is expected to overcome these limitations and provide reliable operation of a high-energy laser at repetition rates of 0.1 to 10 Hz. Current and previous high-energy DPSSL development projects include Mercury (Lawrence Livermore National Laboratory – LLNL in Livermore, California) with average power and efficiency values of 550 W and 7.6%, LUCIA (Laboratoire d'Utilisation des Lasers Intenses – LULI in Palaiseau, France) with 20 W and 5.7%, HALNA (Institute of Laser Engineering, Osaka University, Japan) with 213 W and 11.7%, and Polaris (Institute of Optics and Quantum Electronics of the University of Jena, Germany) with 1.2 W and 6%.

5.3.1 Specifications and description of DiPOLE technology

The DiPOLE laser is based on a scalable diode-pumped, gas-cooled, cryogenic multi-slab Yb:YAG amplifier, capable of generating up to kJ-class pulse energies. The setup of the 10 J DiPOLE laser is shown in Figure 5-17.

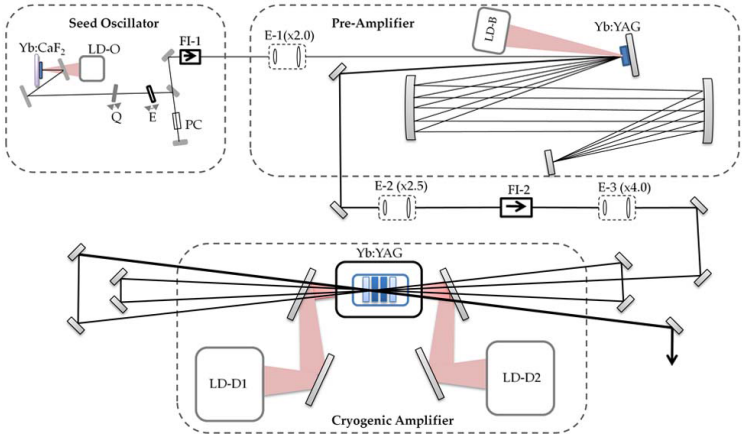

Figure 5-17. *Layout of the 10 J DiPOLE system*

A Yb:CaF_2 cavity-dumped oscillator, tuneable from 1025 to 1040 nm with a spectral bandwidth of 0.2 nm, is used as the seed source, delivering up to 180 µJ at 1030 nm and 10 Hz in a 10 ns (FWHM) pulse duration. The oscillator output is expanded to a 2 mm diameter beam and further amplified by a thin-disk Yb:YAG multi-pass pre-amplifier. This consists of a 2 mm thick, 2.5% doped Yb:YAG crystal arranged in an active mirror configuration, which is pulse-pumped by a 940 nm, 2 kW peak power diode stack for 1 ms duration. An image-relaying multi-pass architecture is used to double-pass

the gain medium seven times. The pre-amplifier delivers 107 mJ at 10 Hz with an M2 value of 1.3. The DiPOLE main amplifier head contains four ceramic YAG disks, each with a diameter of 55 mm and a thickness of 5 mm. The disks consist of a 35 mm diameter Yb-doped inner region that is surrounded by a 10 mm wide Cr_4-doped cladding to minimize amplified spontaneous emission (ASE) loss and prevent parasitic oscillations at high gain. The thickness and doping levels were chosen to maximize optical efficiency while maintaining an acceptable level of ASE loss at the amplifier's design temperature of 175 K.

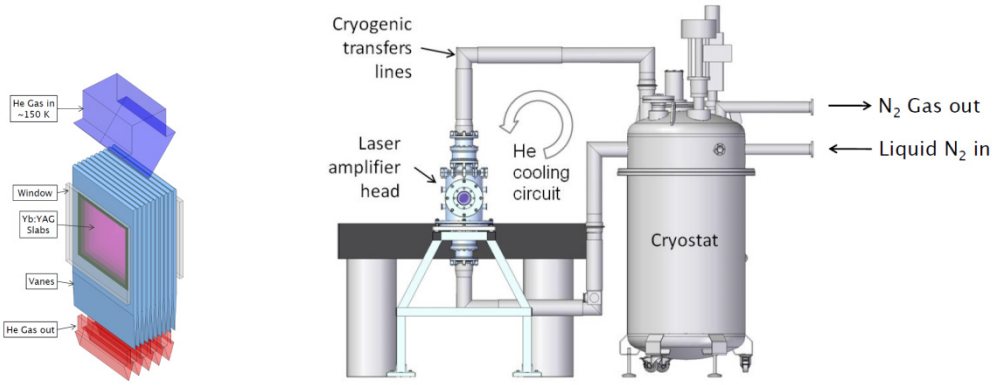

Figure 5-18. *Yb:YAG amplifier and cryo-cooling system of the DiPOLE laser system*

The disks are held in aerodynamically shaped vanes and arranged in a stack with 1.5 mm gaps in between disks. Helium gas at cryogenic temperature is forced through the gaps at a typical volume flow rate of 35 m^3 per hour and a pressure of 10 bar. The helium gas is cooled by passing it through a liquid-nitrogen heat exchanger. The amplifier is pumped from both sides by two 940 nm diode laser sources, each delivering 20 W peak power with variable pulse duration up to 1.2 ms and repetition rate up to 10 Hz. The pump sources produce a 20 x 20 mm^2 square, flat-top beam profile at their image plane, which is arranged to lie at the centre of the amplifier head.

So far, 10 J at 10 Hz was demonstrated from the diode-pumped, gas-cooled, cryogenic multi-slab Yb:YAG amplifier. This confirms the viability of the multi-slab cryogenic amplifier concept, which is scalable to the kilojoule level. Further increases in average power to greater than 100 W and optical-to-optical efficiency greater than 25% are expected at the design temperature of 175 K. The required footprint for the 100 J system is shown in Figure 5-19.

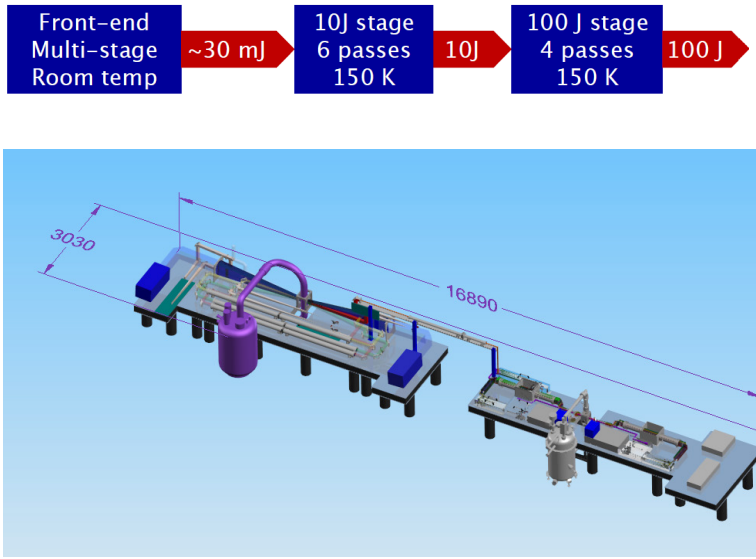

Figure 5-19. *Footprint for the 100 J DiPOLE system*

5.3.2 HE-OL beam transport

Due to the long pulse duration of the HE-OL, non-linear interaction with air is not an issue even after the final amplifier. Therefore, the HE-OL beam can be transported at atmospheric pressure through a DN160 tube to avoid potential wavefront distortion due to air flow.

The required spot size on sample varies from 50 to a few 100 µm with a top-hat profile and uniform intensity distribution. Such spatial profiles can be achieved using an appropriate phase plate. For focusing, *f*/4 or larger optics will be employed. The large beam size on sample relaxes the requirements for the pointing stability compared to the UHI-OL case. Although the mirror support design is not fully developed, a simplified design derived from the UHI-OL transport mirror can be employed.

As seen in Figure 5-11, the HE-OL beam can be split into two beams with an additional delay line for one arm. This capability is required in particular for two-side irradiation experiments. The input ports for the two beams are located on the north side of the IA1experiment chamber. The arrangements of mirrors and focusing lenses inside IA1 are summarized in Figure 5-20. A high flexibility of incidence angles (-20° – 200°) with respect to the X-ray beam will

be provided. One specific requirement is the collinear geometry when using a diamond anvil cell (DAC) due to its geometrical constraints. Absolute 0° incidence is provided using a mirror and lens with a clearance hole at the centre. Potential optics damage due to diffraction made by the hole needs to be evaluated properly.

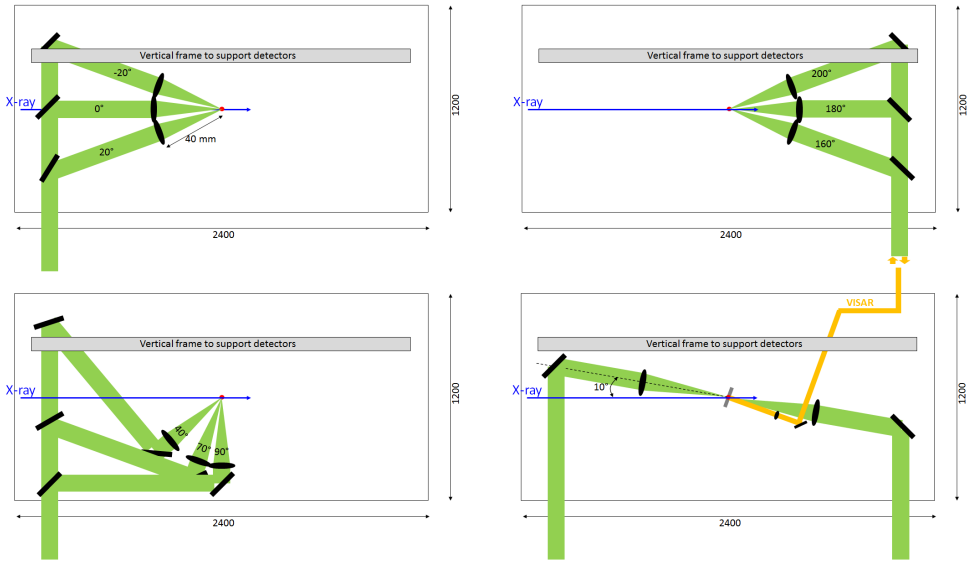

Figure 5-20. *Possible arrangement of mirrors and focusing lenses for HE-OL inside the experiment chamber. Various choices of incidence angles with respect to the X-ray beam are provided. Simultaneous use of two split HE-OL beams with adjustable delay is also provided.*

6 Arrival time monitor

Determination of the relative arrival time between the optical laser pulses and the X-ray pulses is one of the most crucial elements of an experiment requiring highest time resolution on the level of tens of femtoseconds. The measurement should be minimally invasive, and the data should be recorded on a shot-to-shot basis. The information may be used for time sorting and binning after data acquisition, and can also serve to deselect detector recordings when the recorded timing is outside the time window of interest.

The design of the arrival time monitor for the HED instrument is optimized for 10 Hz operation, but 4.5 MHz intraburst repetition capability will also be provided with some limitation in operation.

A particularity of the HED instrument is that different optical lasers need to be synchronized with respect to the arrival time of the X-ray pulses. The pump–probe optical laser (PP-OL) arrival time and its jitter are correlated directly to the X-ray pulses. The arrival time of the 100 TW UHI-OL and the 100 J HE-OL will be correlated to the PP-OL, not directly to the X-ray pulse. For this scheme, additional delay lines are required beyond those introduced in Section 5.1.3. A list of all delay lines is found in Table 6-1. The layout of this optical scheme was already provided in Figure 5-1.

Table 6-1. *List of delay lines*

Delay	Description
D-I	Optical path compensation PP-OL – X-ray
D-II	Pump–probe timing scanning
D-III	Pump–probe path compensation (with respect to the timing line)
D-IV	UHI-OL timing scanning
D-V	UHI-OL path compensation
D-VI	HE-OL timing scanning
D-VII	HE-OL path compensation

The following section gives an overview and details of the current status.

6.1 X-ray–optical arrival time monitor[b]

The X-ray to PP-OL arrival time jitter measurement station is installed permanently ~ 10 m upstream of the sample inside the X-ray optics room (HED-OPT). This location upstream of the X-ray attenuator and the final X-ray focusing optics (CRL3) allows the measurement to be much more independent from the specific experiment conditions.

The present design for this monitor is based on the principles of spatial and spectral encoding, recently developed at DESY and at the Linac Coherent Light Source (LCLS) at SLAC National Accelerator Laboratory in Menlo Park, California.

6.1.1 Requirements

Temporal resolution: 15 fs (goal), no worse than 100 fs
Optical laser energy: 1 µJ or less
X-ray photon number: 10^{10}–10^{12}
X-ray spot size: 30–1000 µm at 5 keV, 15–250 µm at 20 keV
X-ray energy range: 5–25 keV
Non-invasiveness: Properties such as intensity, spectrum, wavefront, and coherence need to be preserved. Targeted transmission: 90%.

6.1.2 Method

The measurement is based on the X-ray–induced change of the refractive index inside a solid material, which is used for time stamping. The current capability yields ~ 10 fs measurement precision, which has been achieved at < 10 keV photon energy range using SiN_4 as material.

Spectral encoding [23][24][25] uses a chirped broadband laser pulse ($\Delta\lambda$ ~ 80–200 nm) such that the different frequency components of the optical pulse arrive at the interaction point at different times. To generate a large broadband pulse, supercontinuum generation using a ~ 1 mm thick sapphire

[b] This section was written including the results of discussions with N. Medvedev and B. Ziaja of Deutsches Elektronen-Synchrotron (DESY), Germany.

can be employed. A nearly linear chirp in the continuum directly relates arrival time to frequency. Insertable dispersive glass plates enable chirping of the PP-OL pulses. One of the advantages of this method is the simple adjustment of the temporal window by changing the chirp.

Spatial encoding [26] relies on the interaction of the X-ray beam with a transparent sample at a certain angle. Depending on the angle, the arrival times at the different positions of the sample differ and thus generate temporal information.

6.1.3 Issues

A major difficulty is that for very high photon energies (larger ~ 10–20 keV), the cascading time for photo-excited electrons becomes much longer [27]. This leads to poor temporal resolution for high photon energy operation at the HED instrument. In addition, the photon energy–dependent absorption cross section suggests that different sample materials need to be employed for different photon energy ranges. At ≤ 10 keV, SiN_4 or chemical vapour deposition (CVD) diamond can be used. The best choice of sample material for hard X-rays > 10 keV is still open. However, preliminary theoretical analysis shows that, at 24 keV photon energy and a relatively small X-ray flux (250 µm spot, 0.6 J/cm^2), enough carrier density electrons can be excited using high-*Z* materials, such as Ga_2O_3 [28].

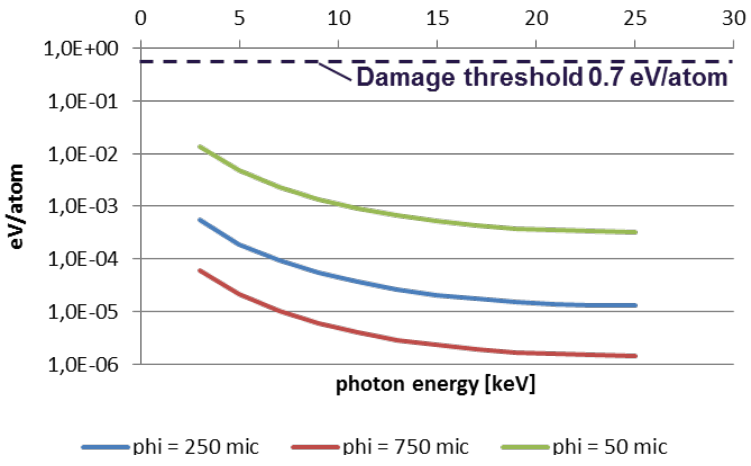

Figure 6-1. *Energy deposited per atom in diamond irradiated by the X-ray beam. 10^{11} photons/pulse is assumed for 5–25 keV X-rays. Single-shot damage is ~ 0.7 eV/atom. Calculations for X-ray beam diameters of 50, 250, and 750 µm are shown.*

Concerning the single-shot damage, it turns out that even for the smallest X-ray beam size at this location, the deposited energy is small enough so that the sample may withstand the X-ray pulse. Figure 6-1 shows the energy deposited per atom for a diamond sample at 10^{11} photons/pulse. The phase transition threshold is 0.7 eV/atom [29].

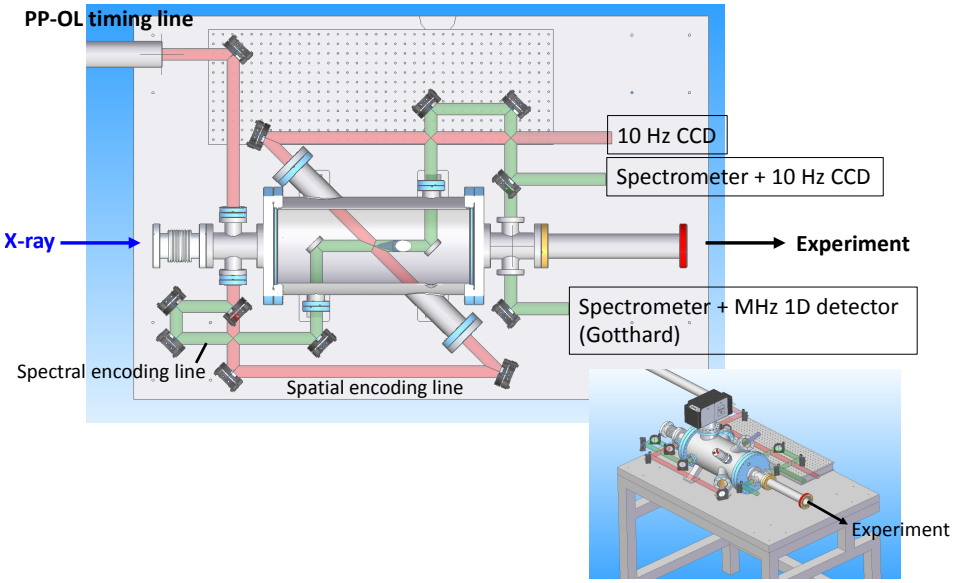

Figure 6-2. *Schematic layout of the timing jitter measurement station. The X-ray beam comes from the left. Red and green beams represent the optical laser (PP-OL).*

6.1.4 Mechanical design

The proposed mechanical layout is shown in Figure 6-2. It consists of a ~ 50 cm long vacuum vessel with a few laser ports attached to it. The PP-OL timing line is propagated through a DN63 vacuum tube to the setup, where the beam is split for the parallel setup of spatial and spectral encoding techniques.

6.1.5 Detectors

For most high-energy laser applications, a 10 Hz readout, using standard CCDs, will be sufficient. This can be done for both spectral and spatial encoding lines. In addition, a 1D detector with MHz readout (Gotthard-V2, developed by Paul Scherrer Institut (PSI) in Villigen, Switzerland) may be installed in the spectral encoding line.

6.2 Optical–optical arrival time monitor

As mentioned above, the arrival time of the UHI-OL and HE-OL will be measured with respect to the PP-OL. The arrival time measurement down to a few picoseconds precision can be done using photodiodes. This precision should be sufficient for the HE-OL arrival determination. The UHI-OL arrival measurement requires a precision better than a few 10 fs and will use a balanced cross-correlator [30] currently under development by J. Wang of the Optical Lasers group. Implementing an active feedback system is also currently under consideration. The detected signal could be fed back via an electronic control loop to keep the two lasers synchronized. This method results in a drift-free and temperature-independent synchronization between these two lasers with very high (~ fs) precision.

In addition to the arrival time monitor, measurement of the absolute time zero at the sample position is required. This measurement of the X-ray and OL pulses arriving at the sample is required to maintain the spatial and temporal overlap with high accuracy. The design of this monitor is still under consideration.

7 Experiment chamber setups

On 11 March 2013, the HED advisory review team (HED-ART) met to discuss and review the HED conceptual design. One of the important suggestions at this review was to develop detailed experiment plans for selected key experiments. The HED group has subsequently selected specific users covering a range of specific and prototypical scientific applications, and has asked them to analyse the specific requirements of these applications and to put these down in experiment plans. These plans now served as a guide for the layout of the instrument, as introduced in this chapter.

7.1 HED-EXP room arrangement

Figure 7-1 shows the current concept for the room arrangement of HED-EXP. This room is 11.4 m long and 9 m wide internally. (For a description of the room, see Section 3.5, “Experiment hutch (HED-EXP)”). One main interaction chamber (IA1, 1.3 x 2.5 m^2) is designed for a large number of experiments requiring both the X-ray beam and the high-energy optical lasers. Additional setups (IA2a, IA2b) at a second interaction point are dedicated to specific experiments, with limited possibilities to use the optical lasers. The IA2 setups will be mounted on a rail so they can be moved in the north–south direction in and out of the X-ray beam. Another translation from IA1 up to the beam stop is required for placing an area detector along the X-ray beam axis and at different distances to the sample. Likewise, the maximum distance from the sample to the detector will be ~ 6.7 m. On the east side of the room, space is reserved for optical beam characterization. There will be several optical tables around the chamber for optical diagnostics.

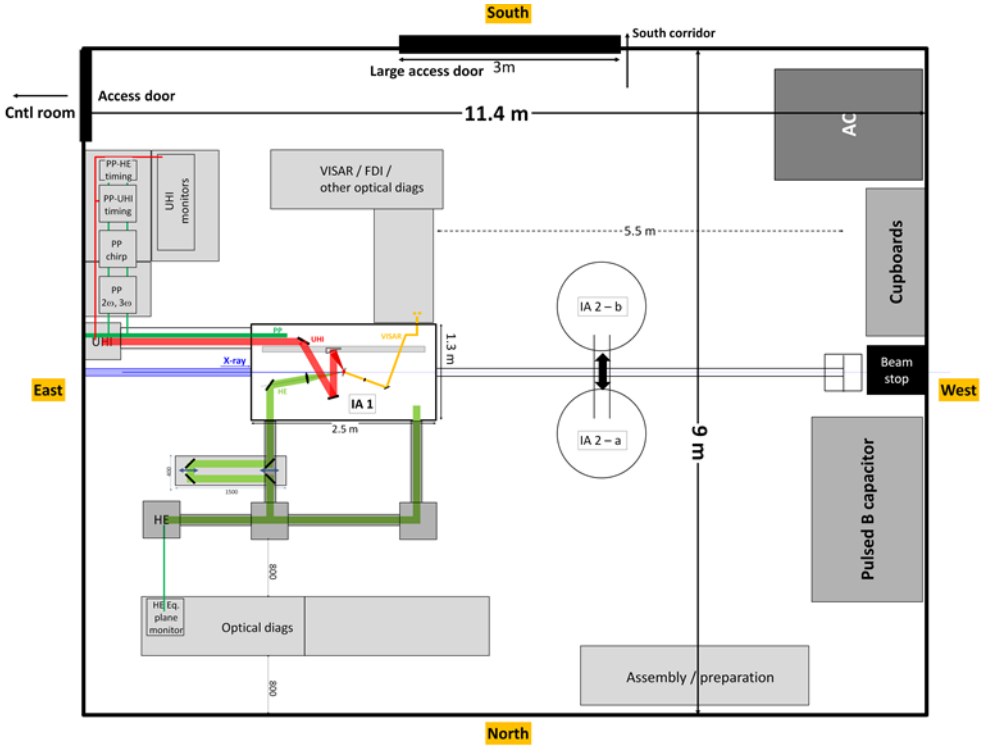

Figure 7-1. *Arrangement inside HED-EXP. The X-ray beam and all optical lasers come from the east (left) side of the room. The interaction point of the main interaction chamber (IA1) is located 3.5 m from the east wall. There are additional setups foreseen at the interaction point 2 (IA2). The size and position of the pulsed magnet capacitor bank has not been refined yet and is subject to change. AC = air conditioning.*

7.2 X-ray scattering geometry

The X-ray beam is polarized in the horizontal plane. X-ray scattering has a polarization factor, $1 - \sin^2\theta\cos^2\varphi$, where θ denotes the scattering angle and φ denotes the azimuth angle. Thus, the scattering signal in the horizontal plane goes to zero as θ approaches 90°. For this reason, the X-ray scattering diagnostics should be mounted in the vertical plane. For the same reason, the detector for self-emission is better placed at $\theta = 90°$ and in the horizontal plane, likewise eliminating the background due to scattering.

7.3 Interaction chamber IA1

This section describes the requirements, proposed realization, vertical optical breadboard, OL beam delivery, and UHI-OL leakage beam for the interaction chamber IA1.

7.3.1 IA1 requirements

The interaction chamber IA1 has to provide sufficient space to place samples and to enable illumination by the X-ray beam and the UHI-OL, HE-OL, and PP-OL beams. In addition, scattering diagnostics and detectors should fit inside this vacuum chamber. Only in this way is great flexibility for spectrometer and detector arrangement possible. We envision an optimal experiment chamber geometry with an inner size of 2.5 m along the X-ray beam and 1.3 m across. The inner height should be 1.4 m. The mass of such a chamber is ~ 3 t.

The reasons for this choice are as follows:

- The spectrometer for high-resolution inelastic X-ray scattering (hr-IXS) requires a quasi-continuous selection of the scattering angle and the scattering vector q, respectively. It is therefore better located inside the vacuum chamber. The chamber length and height are determined by the spectrometer length of ~ 1 m.
- In order to provide users with a great amount of flexibility for the geometry under which the optical laser beam impinges on the sample (and relative to the X-ray beam), and to minimize transition time when changing from one experiment setup to the other, sufficient space for OL transport must be provided inside the chamber. For the 100 TW UHI-OL beam in particular, focusing uses reflecting optics that require space. The laser transports for both the UHI-OL and the HE-OL are discussed in Section 5.2.6, “UHI-OL beam transport” (see e.g. Figure 5-14).

While a large interaction chamber has the advantage of flexibility, it also leads to a few issues that need to be resolved.

The two most important issues are:

- **Access and time to establish operating conditions**

  Access and the time to establish operating conditions following access. Most relevant here are the vacuum conditions required to operate the chamber with window in the X-ray transport beamline. For a large chamber, it may be difficult to achieve very good vacuum conditions and pumping time may be long. We aim for a pumping time of 15 min and 20 min (minimum). This will require the appropriate design of parts, flanges, access ports, and the pumping system. We further propose to employ an automated sample frame exchanger, which will allow the execution of a large number of shots without breaking the vacuum (see Section 7.6.5, “Sample positioning and replacement”).

- **Complex detectors not designed for vacuum conditions**

  Placing detectors of high complexity inside the chamber that are often not designed to operate under vacuum conditions. Due to the large chamber, most detectors need to be mounted inside vacuum or using specially design flange assemblies. Placing detectors inside vacuum is often not possible, either because the detectors— especially their electronics—are not vacuum-compatible or because these detectors require direct access by an operator. Such detectors could be placed only outside the vacuum chamber, but then they would have a large distance to the sample and therefore a small solid angle and efficiency. So-called “re-entrant flanges” may allow the vacuum interface to be moved from the chamber wall towards the sample, likewise mitigating the distance issue. However, these types of flanges are often complex and require specific design. Another issue with having the detectors inside the vacuum chamber arises from the electromagnetic pulse (EMP) generated by the high-intensity laser pulses, which can damage detector electronics temporarily or permanently. As the strength of the EMP decays with distance to the sample and it is partly shielded by the metallic vacuum chamber wall, the EMP issue is much more important inside the chamber than outside. More discussions on the EMP issue are found in Section 8.1, “X-ray detectors”.

7.3.2 IA1 proposed realization

The proposed design for IA1 is shown in Figure 7-3. The interaction point is at the midpoint of the chamber, 1400 mm from the floor and approximately 325 mm above the optical table, allowing for a symmetrical arrangement of components inside the chamber or fixed to external ports. The chamber is designed with two large access doors (with a 60 cm width) on both long sides to facilitate access to the entirety of the chamber. The roof is removable to facilitate moving large items in and out of the chamber using the lab crane.

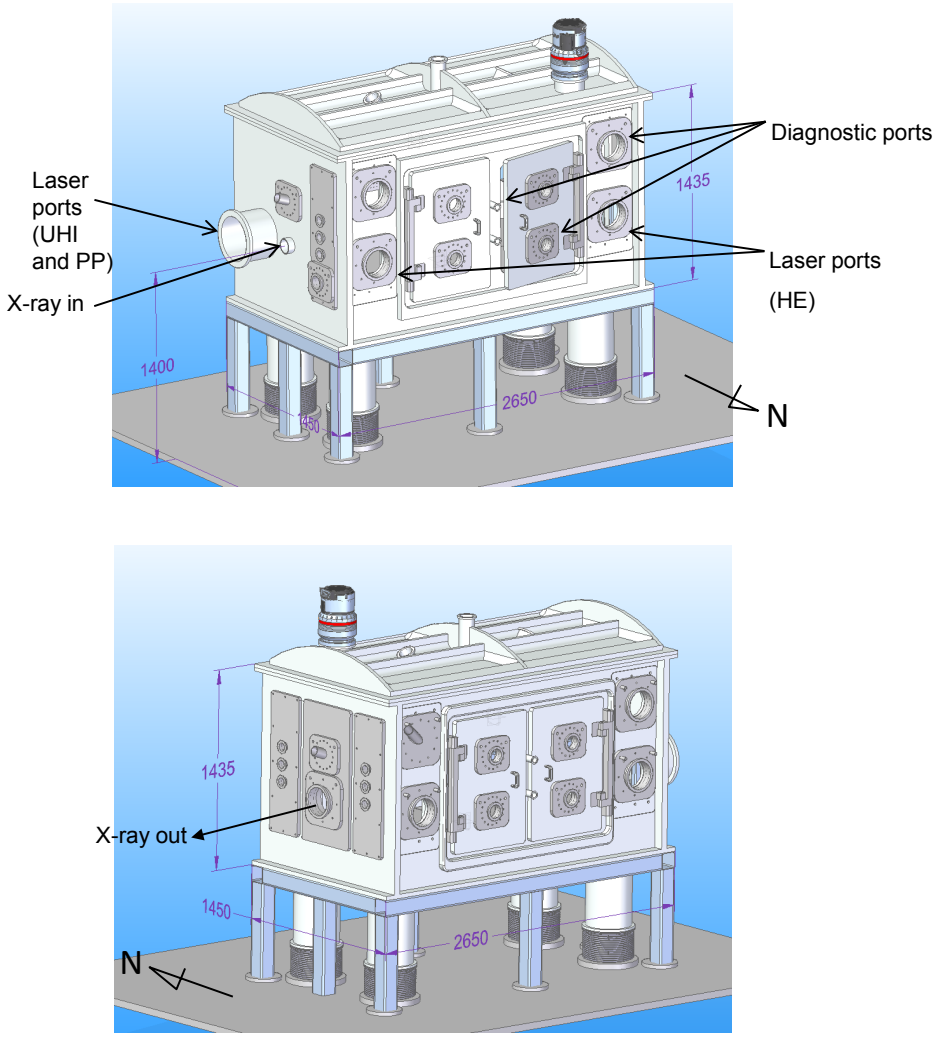

Figure 7-2. *Proposed design of the interaction chamber IA1. The upper panel shows a view from the front (north), the lower panel from the back (south).*

There are four main ports for optical laser transport on each side of the chamber, fixed to large removable panels. This design allows for high

flexibility in arranging specific user requirements. The two lower ports on each side are reserved for optical lasers; the remaining ports can be used for user-defined equipment. These ports are mounted on standard ISO-K flanges. These setups, or the entire panel, can be removed from the chamber to accommodate various requirements.

Additional viewports are also positioned on the chamber doors for non-critically positioned equipment. Two small ports might be positioned on the vertical bar between the doors, as only these ports offer a view of the sample in a direction perpendicular to the X-ray beam. Further flanges can be arranged on the entrance and exit sides of the chamber, again making use of large panel designs for simple customization to user requirements.

There are three fixed diagnostic ports positioned on the roof of the chamber and an additional port at each end of the chamber. These ports are placed on a radius of 1115 mm, at angles of 60°, 90°, and 120° relative to the incident X-ray beam, and are pointing to the interaction point (Figure 7-3).

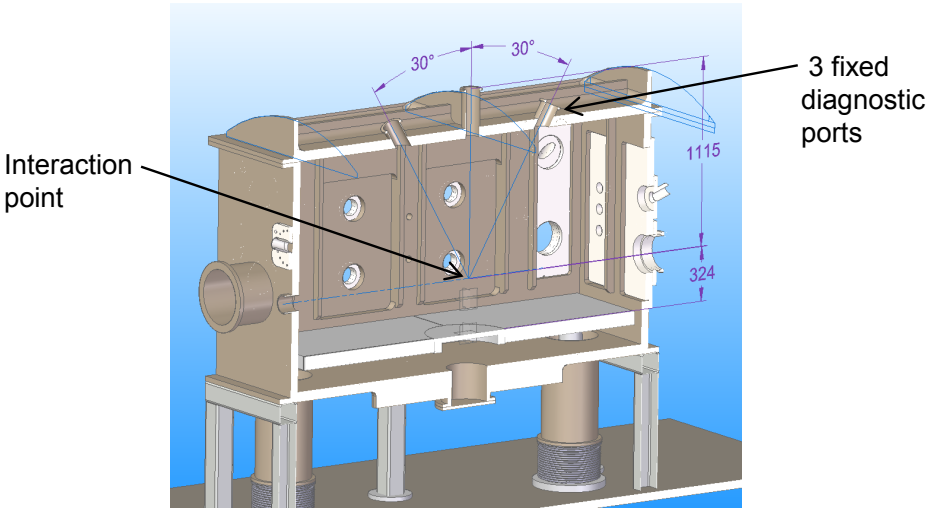

Figure 7-3. *Cross section of IA1 showing three fixed diagnostic ports on top. The X-rays come from the left.*

The horizontal optical table is mounted directly onto the lab floor in order to decouple it from vibrations and movements of the vacuum chamber (Figure 7-4). The vacuum interface for the legs is achieved by means of vacuum bellows. The chamber is separately supported on a rigid steel frame designed to minimize vibration passing into the chamber. The optical table

may be split into five segments to minimize distortion from heavy loads and to allow the separation of the sample mount (Figure 7-4). In particular, the sample mount could be a source of vibration due to the relatively high speed at which samples need to be rastered and exchanged.

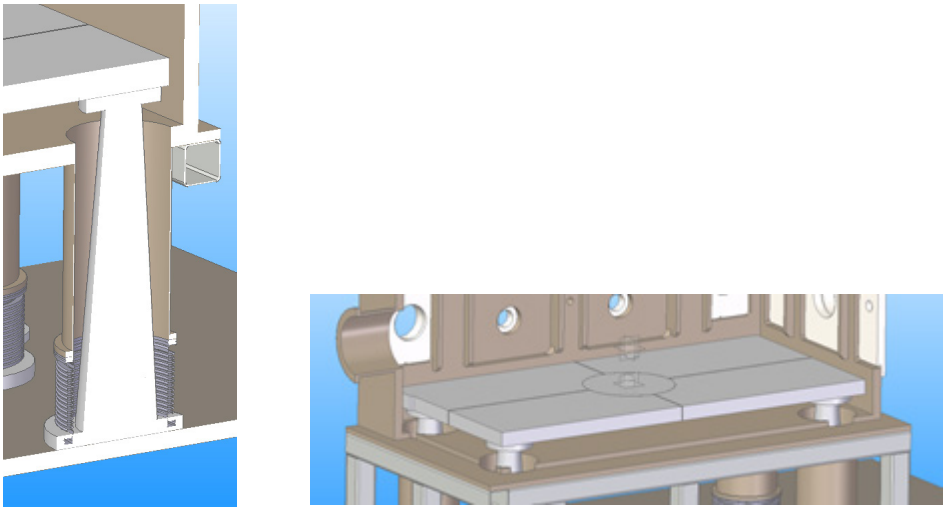

Figure 7-4. Left: *IA1 chamber. Optical table legs are decoupled from the chamber itself.* Right: *Segmented optical table.*

7.3.3 Vertical optical breadboard

A second optical breadboard (Figure 7-5), measuring 600 mm (height) x 2200 mm (length), will be installed inside the chamber for mounting detectors or other equipment in the vertical scattering plane (see Section 7.2, “X-ray scattering geometry”). In order to allow access to and work on this breadboard, it is mounted on a rail enabling it, including all mounts, to be moved from its nominal position towards the chamber access (north side doors). To ensure a high repeatability of the positioning of the breadboard in its nominal position, we propose to locate it on studs in this position. So far, no designs exist for the mounts on this vertical optical breadboard or the interfaces to X-ray spectrometers and detectors.

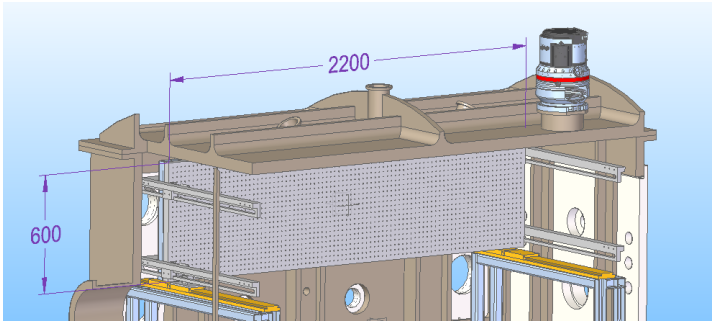

Figure 7-5. *Vertical breadboard in the IA1 chamber*

7.3.4 OL beam delivery to IA1

IA1 has permanent vacuum connections to the X-ray, PP-OL, and UHI-OL beam transports. The PP-OL and UHI-OL beams enter on the same side and at the same height as the X-ray beam. The same, large flange is used for both beams. The HE-OL beam enters on the north side, using either one or two beams. Again, the beam height is the same as that of the X-ray beam. Likewise, inside the vacuum chamber, the OL beams do not require any adaption of beam height, other than minimal beam movements due to the use of special X-ray optics (see Chapter 4, “X-ray beam transport”). Outside and around IA1, several optics tables and installation are required for diagnostics and preparation of the OL beams.

The PP-OL delivery tube runs through the HED optics hutch at a height of 1050 mm from the floor and is offset by 500 mm from the X-ray beam (Figure 7-6). The beam transport enters HED-EXP through the east wall and immediately below the UHI-OL laser beam delivery mirror MU4 (Figure 7-7). UHI-OL uses leakage through MU4 for diagnostics. This leakage radiation is sent to an optical table next to this mirror. The PP-OL beam has to pass through this transport as shown in Figure 7-7 and is directed to the same optical table. Behind the turning mirror, PP-OL is transported in air, directed towards a variety of OL devices mounted on the optical table (as described in Chapter 5, “Optical lasers”), and finally steered back into IA1. When the PP-OL beam leaves the optical table, it is brought to a beam height of 1400 mm and steered into the UHI-OL beam delivery tube, where it runs parallel to the UHI-OL beam entering IA1.

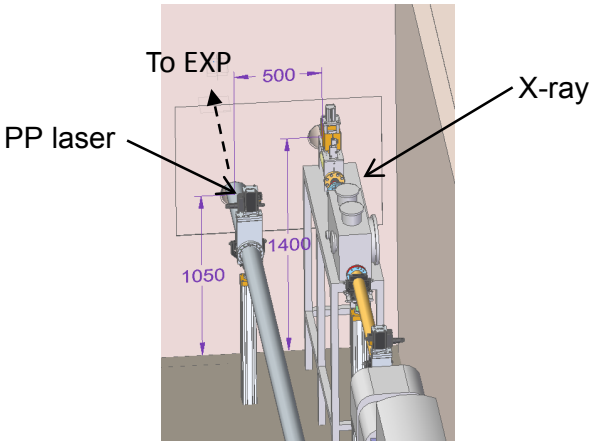

Figure 7-6. *X-ray and PP-OL delivery from X-ray optics hutch (HED-OPT) to the experiment hutch (HED-EXP), as shown from inside HED-OPT.*

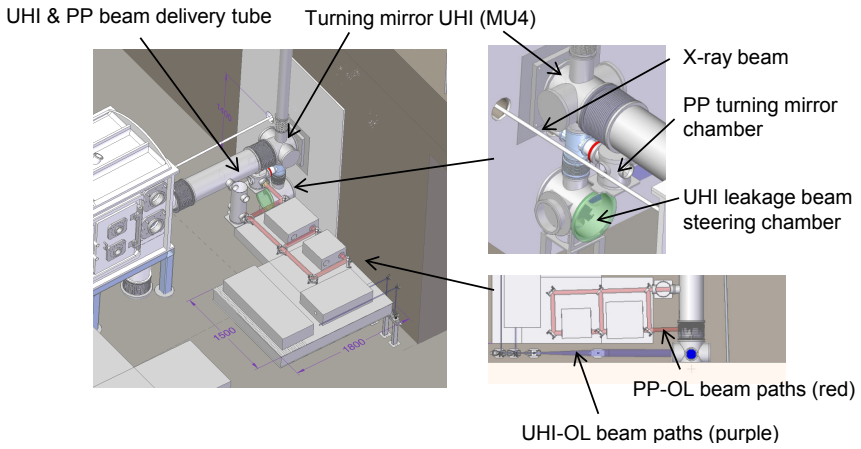

Figure 7-7. *PP-OL and UHI-OL delivery at the entrance of HED-EXP*

7.3.5 UHI-OL leakage beam

The use of the UHI-OL leakage beam for beam characterization is discussed in Section 5.2.6, “UHI-OL beam transport”. The UHI-OL beam coming from HED-HPLAS leaves the vacuum system after the turning mirror (MU4) and passes under the optical tables, where it is reduced in size. The beam is then brought back to the optical table with periscopes and directed to several diagnostics devices. For convenience, Figure 5-17 on page 114 and its 3D view are shown again in Figure 7-8.

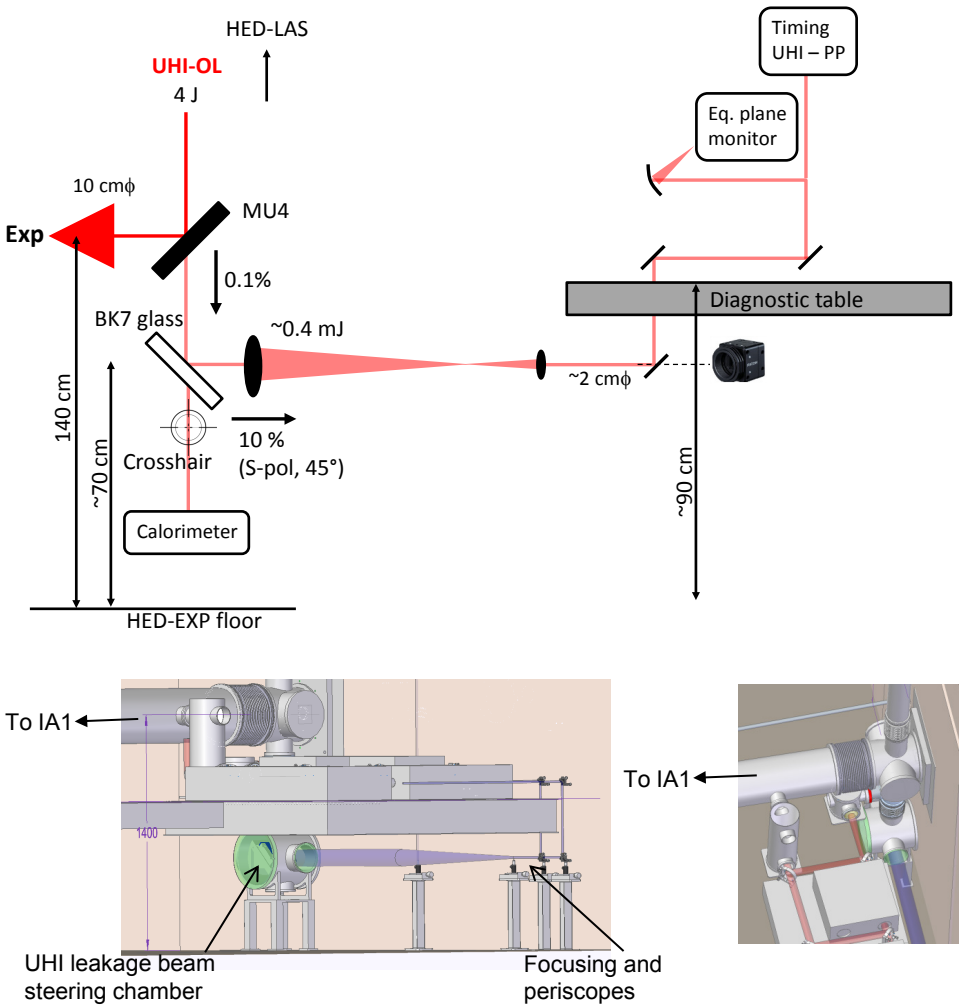

Figure 7-8. *Leakage from the MU4 mirror for UHI-OL beam characterization*

7.4 Interaction area IA2

In the interaction area IA2 inside HED-EXP, space is provided to build up specific instruments dedicated to specific types of experiments. As of now, we do not foresee delivering any of the laser beams to this location. It is proposed that these setups are mounted on a rail, moving perpendicular to the X-ray beam transport (north–south) and allowing the setups in the beam to be exchanged. Ideally, these setups would be removable in order to provide flexibility towards a multitude of instrumentation. However, due to their complexity and weight, this might not be easily achievable. Through the

experiment detail reports, we already identified two setups that should be located here.

7.4.1 Interaction area IA2a

Interaction area IA2a could be dedicated to pulsed high-field magnet experiments. It likely will require a magnet coil, sample mounts including UHV vacuum and helium cryostats, and a diffractometer arm for the detection of Bragg spots. Different geometries have been proposed, and the exact designs of vacuum chamber and cryostat, pulsed magnet system, and diffractometer with detector still have to be clarified.

7.4.2 Interaction area IA2b

Interaction area IA2b could be dedicated to high-energy, in-air, diamond anvil cell (DAC) experiments. These experiments would make use of the high peak brilliance and average flux available within the X-ray pulse train. The setup will include a dedicated optical laser for pulse heating of the samples inside the DAC. The design of this setup still has to be clarified.

7.5 Implementations of X-ray techniques

This section describes implementations of the following X-ray techniques: X-ray diffraction (XRD) and wide-angle X-ray scattering (WAXS); small-angle X-ray scattering (SAXS); X-ray Thomson scattering (XRTS); high-resolution inelastic X-ray scattering (hr-IXS); near-edge X-ray absorption spectroscopy (XANES) and X-ray emission spectroscopy (XES); and X-ray imaging (XI).

7.5.1 X-ray diffraction (XRD) and wide-angle X-ray scattering (WAXS)[c]

7.5.1.1.1 Requirements for optical lasers and their applications

- HE-OL and VISAR
  - — High-pressure studies of shock or ramped laser-compressed matter
  - — High-pressure studies combined with HE-OL and diamond anvil cell (DAC)
- PP-OL
  - — Laser-excited materials under laser processing conditions, ultrafast phase transitions
  - — WDM generation and study
- Optical laser incidence angle with respect to the X-ray beam: collinear (0°) to ~ 45°

7.5.1.1.2 Requirements for X-ray delivery

- X-ray photon energy: 10–25 keV

  Typically, high photon energy is preferred. In particular, DAC experiments require the highest possible photon energy (~ 25 keV) to avoid absorption and heating of the diamond.
- X-ray bandwidth: 10^{-4}–10^{-3}

  The Si_{111} monochromator located at a distance of 118 m upstream of the sample can be used to provide $\Delta E/E = 10^{-4}$.
- X-ray beam size on sample: few µm – ~ 100 µm
  - — X-ray beam size on sample should be smaller than the pump optical laser spot size.
    - – Laser compression experiment: < 100 µm
    - – Laser processing: < few 10 µm
    - – DAC experiment: ≤ few µm

[c] This section is based on experiment detail descriptions provided by A. Higginbotham, K. Sokolowski-Tinten, Z. Konopkova, E. McBride, and H.-P. Liermann.

- — Beam divergence at sample position: ≤ 0.1 mrad (should be smaller than the required resolution)
- — 0.1 mrad divergence corresponds to ~ 1 µm focusing at 10 keV

- Repetition rate: < 10Hz or pulse on demand

7.5.1.1.3 Requirements for diagnostics and detectors

The crucial parameter here is the distance between the sample and the detector. This value, the pixel size, and the number of pixels determine the angular resolution and the angular coverage. Figure 7-9 (top) shows the relationship between the detector distance, the pixel size, and the angular resolution. From the requirement for angular coverage (2θ), the required number of pixels can be determined (Figure 7-9 (bottom)). For a WAXS experiment, the typical sample–detector distance will be < 1 m, and a 1k x 1k (Mpx) detector will ideally be used. A selection of possible detector types for WAXS experiments is discussed in Section 8.1, “X-ray detectors”.

Other important remarks are summarized as follows:

- Detectors need to be located in the forward direction and on the side (~ 90°) with respect to the X-ray direction
- Angular resolution: 0.1–1 mrad
- Angular coverage (for forward scattering): 2θ = 10°–70° (0.17–1.2 rad)
- Dynamic range: 10^3–10^4
- In the forward direction, the detector needs a hole or beam stop on the X-ray axis to prevent X-ray damage. Approx. 1 mm around the beam axis on the detector must be protected from X-ray irradiation.

A prototypical layout for such experiments is shown in Figure 7-10. The SAXS C detector is not shown and is discussed in Section 7.5.2, “Small-angle X-ray scattering (SAXS)”.

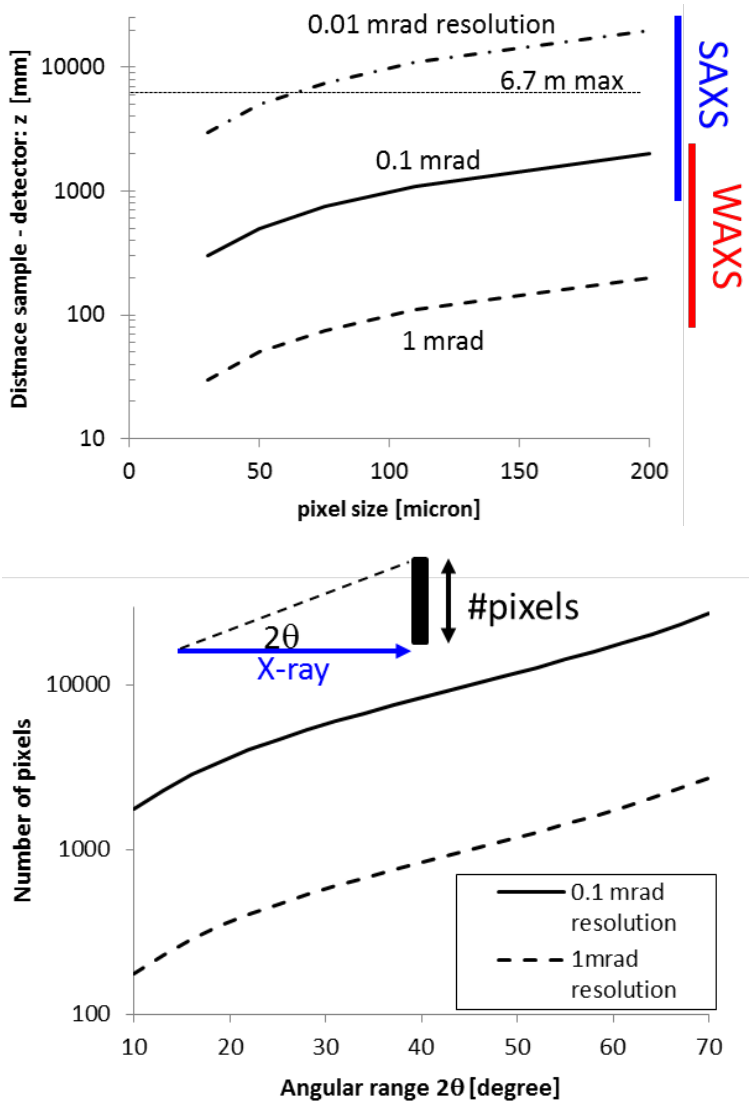

Figure 7-9. Top: *The optimum sample–detector distance is determined by angular resolution and detector pixel size. Specifications of detectors are summarized in Figure 8-2.* Bottom: *The relation of pixel number to angular range 2θ (in 1D) is determined by the sample–detector distance and the pixel size, which can be expressed by the angular resolution. To cover -2θ to $+2\theta$, twice as many pixels are required.*

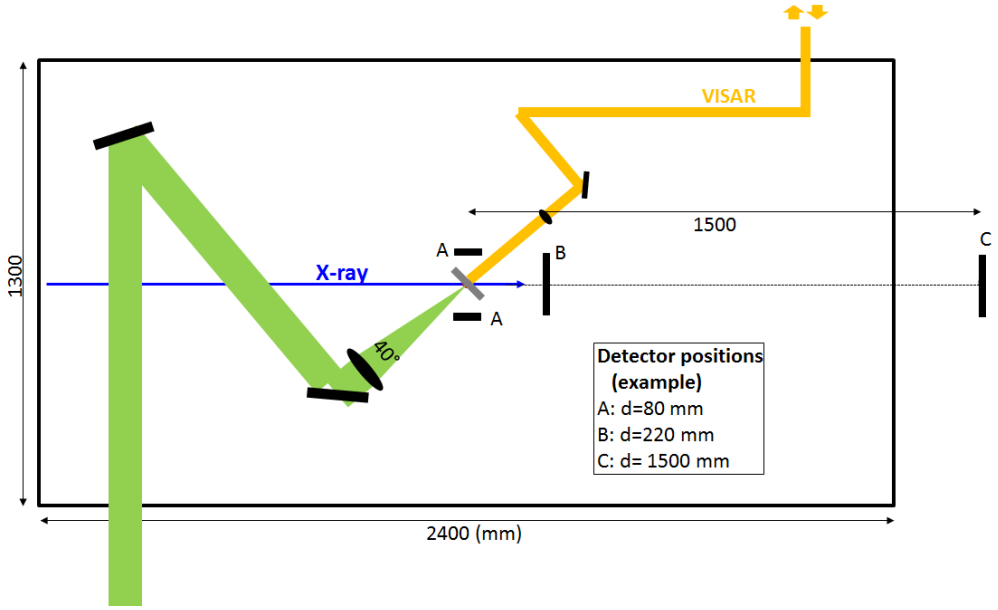

Figure 7-10. *Sketch of prototypical setup for XRD experiments, e.g. for high-pressure studies of laser compression. HE-OL generates a shock or a ramp compression wave within the system, whose breakout is optically probed using VISAR diagnostics. The sample is oriented at ~ 45° with respect to the X-ray beam. X-ray diffraction is measured using several area detectors. Small detector panels are placed close to 90° to the X-ray beam, allowing the measurement of strength (Detectors A in the figure). A large-area detector (B) in the forward direction detects Bragg and power diffraction. A SAXS detector, several metres downstream, provides information on the microstructure formed upon compression (not shown).*

7.5.2 Small-angle X-ray scattering (SAXS)[d]

Small-angle X-ray scattering (SAXS) provides information about structural order and dynamics on nanometre to micrometre length scales. The scattering is recorded typically for an angular range covering several 10s of mrad, up to ~ 70 mrad.

7.5.2.1.1 Requirements for optical lasers and their applications

- HE-OL and VISAR

  High-pressure studies of shock or ramped laser-compressed matter. SAXS allows measurements of the microstructure upon compression.

- PP-OL
  - Laser-excited materials under laser processing conditions, ultrafast phase transitions
  - WDM generation and study

- UHI-OL
  - Density modulation driven by very intense optical field interaction with solids
  - Relativistic high-density electron beam (> MeV, ~ 10^{21} cm^3) generation and filamented transport inside solid-density plasmas

7.5.2.1.2 Requirements for X-ray delivery

- X-ray photon energy: 5–25 keV
- X-ray bandwidth: 10^{-3}–10^{-2}
- X-ray beam size on sample: sub µm – few 10 µm
  - Sub-µm to few µm for UHI-OL and PP-OL pump
  - Up to few 10 µm for HE-OL pump
- Repetition rate: in most cases, < 10 Hz or pulse on demand
- Beam divergence at sample position: smaller than required resolution

[d] This section is based on the experiment detail descriptions provided by A. Pelka and K. Sokolowski-Tinten.

— Extreme resolution (0.01 mrad) means one has to work with a collimated beam, not with a strongly focused beam. The divergence is related to the X-ray wavelength $\lambda_{\text{X-ray}}$ and the diffraction-limited focal size ϕ_{diff} through $\sim \lambda_{\text{X-ray}}/\phi_{\text{diff}}$. 0.01 mrad divergence corresponds to a ~ 10 µm spot at ~ 10 keV.

7.5.2.1.3 Requirements for diagnostics and detectors

- Detectors are located in the forward direction at a relatively large distance, typically a few metres from the sample:
  - The relationship between the angular resolution and the sample–detector distance is shown in Figure 7-9(a). The maximum distance is ~ 6.7 m, limited by the HED-EXP room size and other instrumentation.
  - The detector and interaction chambers need to be connected by a vacuum pipe. Variable distances need to be enabled.
- Angular resolution: 0.01–0.1 mrad
- Angular coverage: diffraction angle 2θ = 0.01°–4° (0.17–70 mrad)
  - This angle provides access to *d*-spacings of 1.5 nm – 0.6 µm at 12 keV
  - Corresponding *q*-range of 0.002–0.84 $Å^{-1}$ at 12 keV
- Number of pixels: depends on *q*-range and required resolution
- Dynamic range: ≥ 10^4
- Detector needs a hole or beam stop on the X-ray axis. That is, ~ 1 mm around the beam axis on the detector must be protected.

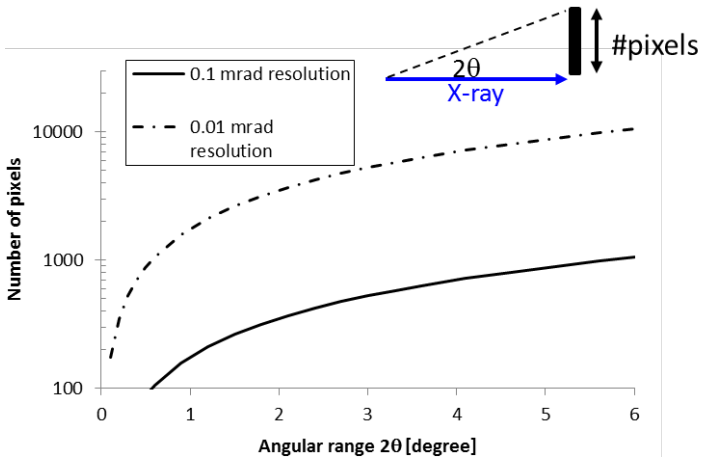

Figure 7-11. *Relation between number of pixels, angular range, and angular resolution for SAXS experiments*

The smallest accessible *d*-spacing (largest *q*) is limited by the numerical aperture covered by the detector. The largest accessible *d*-spacing is determined by the central hole / blocked area and the maximum distance (6.7 m) from the sample. Another parameter determining *q* is the photon energy. Table 7-1 lists the *q*-range and *d*-spacing for 5, 12, and 24 keV at two extreme sample–detector distances. This range satisfies the above-mentioned *d*-spacing requirement. The prototypical setup for SAXS experiments is shown in Figure 7-12.

Table 7-1. *q-range and d-spacing range for SAXS. Assumptions: short/large detector distances are 500/6700 mm; an area with a radius of 1 mm around the X-ray beam is blocked; and the detector radius is 40 mm.*

Sample–detector [mm]	**Diffraction angle 2θ [°]**	**Photon energy [keV]**	***q*-range (2k sinθ) [Å^{-1}]**	***d*-spacing range [nm]**
500	0.11–4.6	5	0.005–0.2	3.1–126
		12	0.012 –0.48	1.3–52
		24	0.024 –0.96	0.65–26
6700 (max)	0.009–0.34	5	0.00037–0.015	42–1680
		12	0.0009–0.036	18–700
		24	0.0018–0.072	8.8–350

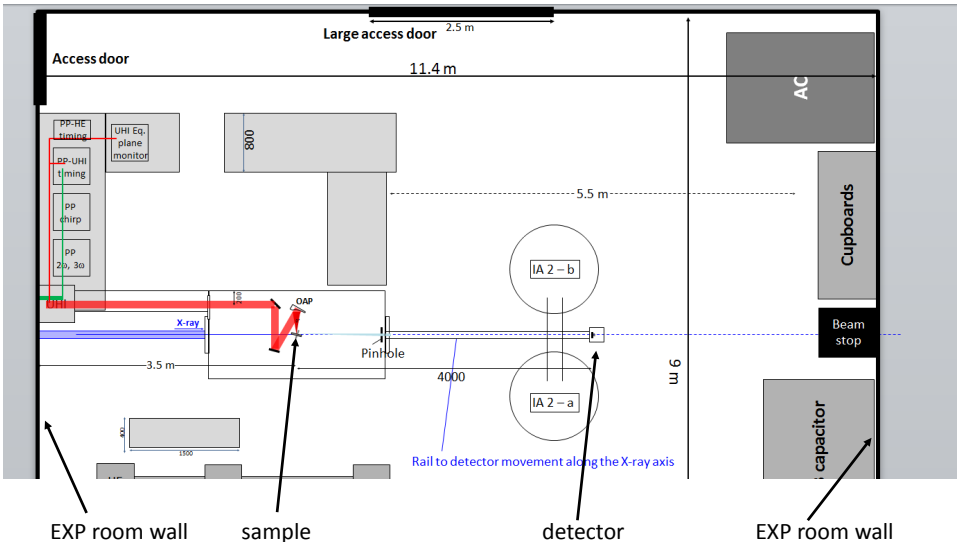

Figure 7-12. *Sketch of the prototypical SAXS setup for ultrahigh-intensity laser–plasma interaction study. The UHI-OL comes from the east side of the interaction chamber. Followed by two planar mirrors, a 30° off-axis parabolic mirror focuses the beam perpendicular to the X-ray axis (from up to down in the figure). The detector is mounted a few metres downstream of the sample on the rail. The detector and the chamber are connected through a variable-length ~ DN100 vacuum tube.*

7.5.3 X-ray Thomson scattering (XRTS)[e]

X-ray Thomson scattering (XRTS) refers to a technique comprising the measurement of elastic Rayleigh scattering from bound electrons, as well as inelastic non-collective Compton scattering and inelastic collective plasmon scattering, both from free electrons. Experimental observables are temperature, density, degeneracy, and charge state. In forward scattering geometry, the inelastic energy separation of the up- and down-shifted plasmons yields the free-electron density. The temperature is inferred from the shape of the spectra or the intensity ratio of the up-shifted to down-shifted plasmon intensities. The down-shifted non-collective Compton spectrum is broadened by the thermal motion of the electrons, thus inferring the electron velocity distributions, or, for degenerate systems, providing the Fermi energy so that the density is given.

[e] This section is based on the experiment detail descriptions provided by R.W. Lee, J. Hastings, and P. Neumayer as well as further discussions with U. Zastrau.

7.5.3.1.1 *Requirements for optical lasers and their applications*

- HE-OL and VISAR
  - — High-pressure studies of shock or ramped laser-compressed matter

    HE-OL: 100 J, 2ω, top-hat spatial profile, smoothed beam with few 100 µm spot, temporal shaping, *f*/# = 4–10
  - — WDM creation by laser-induced shock

    HE-OL: ~ 10 J, top-hat profile, smoothed beam with few 100 µm spot
- PP-OL
  - — WDM generation through ballistic electron transport

    PP-OL mode-I: 1 mJ / ~ 30 fs, few 100 µm spot, Gaussian temporal profile
  - — WDM generation through laser-induced shock

    PP-OL mode-II: 100 mJ / ~ ps, few 100 µm spot, Gaussian temporal profile

7.5.3.1.2 *Requirements for X-ray delivery*

- X-ray photon energy: 5–5 keV
- Bandwidth: 10^{-4}–10^{-3}. Such a bandwidth can be provided by a standard Si_{111} monochromator.
- Beam size on sample: 10–50 µm, smaller than the pump pulse
- Repetition rate: in most cases, < 10 Hz or pulse on demand

7.5.3.1.3 *Requirements for diagnostics and detectors*

- Due to the polarization factor, scattering will be detected in the vertical plane. A vertical table is installed inside the experiment chamber to mount and move the XRTS spectrometers in the vertical plane. The mechanical design of a scanning device that would allow the remote definition of the scattering angle still needs to be achieved. The dispersion plane of the spectrometers will also be in the vertical plane.
- Angular coverage: near-forward to near-backward scattering to scan different *q* values

- Energy resolution: $\Delta E/E$ ~ few 10^{-3} for collective scattering and ~ 10^{-2} for non-collective Compton scattering

The current design of the spectrometer uses the von Hamos geometry employing mosaic cylindrical crystals. Details of this spectrometer are described in Section 8.2, “X-ray diagnostics—von Hamos–type spectrometer”. A prototypical experiment setup for XRTS measurements is shown in Figure 7-13.

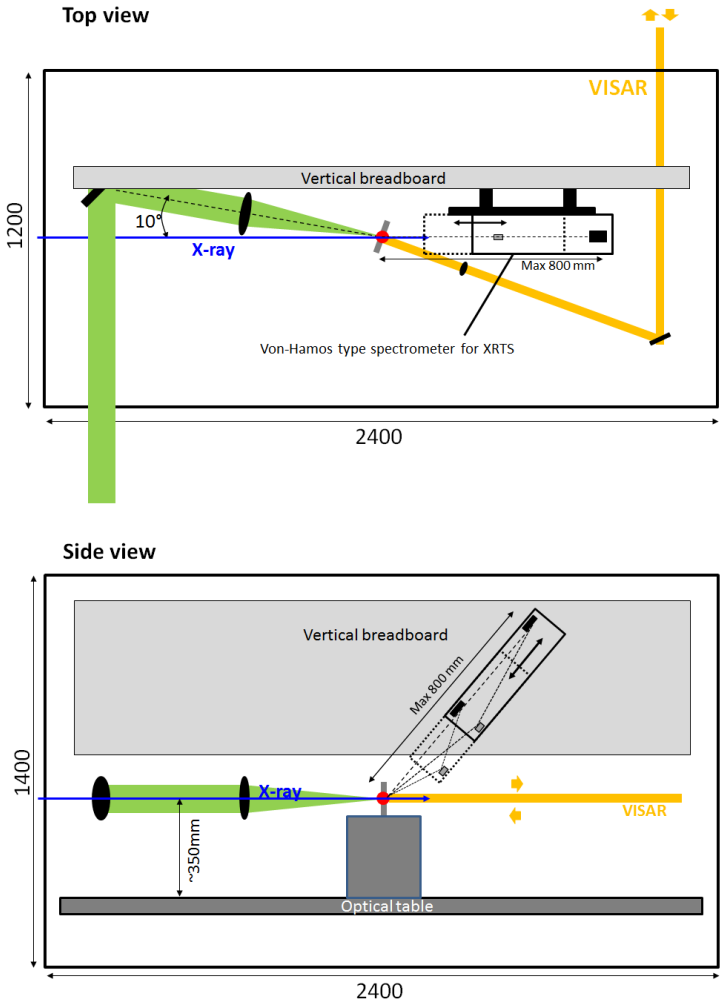

Figure 7-13. *Sketches of the prototypical setup for XRTS experiments in high-pressure studies of laser-compressed matter. HE-OL generates a shock or a ramp compression wave within the sample, whose breakout is optically probed using VISAR. The laser irradiates the sample close to collinear to the X-ray beam. The VISAR laser irradiation is normal to the sample surface.*

7.5.4 High-resolution inelastic X-ray scattering (hr-IXS)[f]

The measurement of the dynamic structure factor using high-resolution inelastic X-ray scattering (hr-IXS) with meV resolution provides information of the properties of the ions [31]. The ion acoustic modes in the ion–ion structure factor are separated by $2\hbar\omega_{\mathrm{pi}} \sim 0.2 - 1\ eV$ in most WDM states (ω_{pi} is the ion–plasma frequency). Experiments at small *q* values (small scattering angles) provide information about the acoustic waves, in particular on the longitudinal sound velocity and viscosity. At large *q* values, the single-particle limit is approached, giving information on the ion temperature.

A sub-eV energy resolution requires crystal analysers providing a near 90° Bragg reflection to increase the Darwin width ($\Delta E/E \tan\theta_{\mathrm{Bragg}}$) to a value comparable to the X-ray beam divergence. This geometry also requires a large distance from the sample to the analyser.

Requirements for optical laser properties using hr-IXS are very similar to those using XRTS. An additional requirement comes from the necessity of highly uniform heating through laser irradiation, as macroscopic inhomogeneities introduce broadening of the resonance lines.

7.5.4.1.1 Requirements for X-ray delivery

- X-ray photon energy: only discrete $h\nu$ are possible due to the fixed Bragg angle geometry of analyser and monochromator. Examples: 7.919 keV (Si_{444}), 9.899 keV (Si_{555}), or 13.858 keV (Si_{777}).
- Bandwidth: High monochromatization ($\leq 5 \times 10^{-6}$) is required. The bandwidth $\Delta E/E$, or energy resolution, needs to be matched for the monochromator and the hr-IXS spectrometer. As an example, Si_{444} gives $\Delta E/E \sim 60$ meV at 7.9 keV.
- Beam size on sample: ~ 10 µm or smaller with respect to the OL spot size and to the pixel size of the detector
- Repetition rate: in most cases, < 10 Hz or pulse on demand

[f] This section is based on an experiment detail description provided by and further discussions with G. Monaco.

7.5.4.1.2 *Requirements for diagnostics and detectors*

- Energy resolution: $\Delta E/E \sim 5 \times 10^{-6}$
- Diagnostics consist of a spherical analyser and a detector in Rowland circle geometry.
  - Distance sample–analyser is ~ 1 m.
  - Detector sits ~ 100 mm next to the sample (backscattered, Bragg angle ~ 87°).
- Scattering geometry is on the vertical plane and dispersive direction is on the horizontal plane.
  - Angular coverage: few to ~ 150° to scan different *q* values
  - It should be possible to change the scattering angle, ideally through remote control, e.g. analyser mounted on rails and rotatable detector stage. The mechanical design still needs to be achieved.
- Analyser
  - Spherical shape with ~ 1 m radius of curvature, size ~ 10 cm
  - Silicon is used due to its high crystalline quality.
  - A Si_{444} crystal is used for ~ 7.9 keV, Si_{555} for ~ 9.9 keV, and Si_{777} for ~ 14 keV.
  - Elastic bending of the crystal destroys the resolution. Therefore, the analyser will be built by slicing a Si wafer, thus producing many "Si blocks" on a wafer membrane and gluing the wafer on a spherical substrate.
- Detector
  - Pixel size: < 100 µm (point spread function is few 100 µm)
  - Chip size: > 5 cm, or > 1 eV coverage in dispersive plane
  - Single-photon sensitivity
  - Dynamic range: ~ 10^4
- Alignment precision

  ~ 10^{-2} mrad in theta

A prototypical setup for hr-IXS experiments is shown in Figure 7-14.

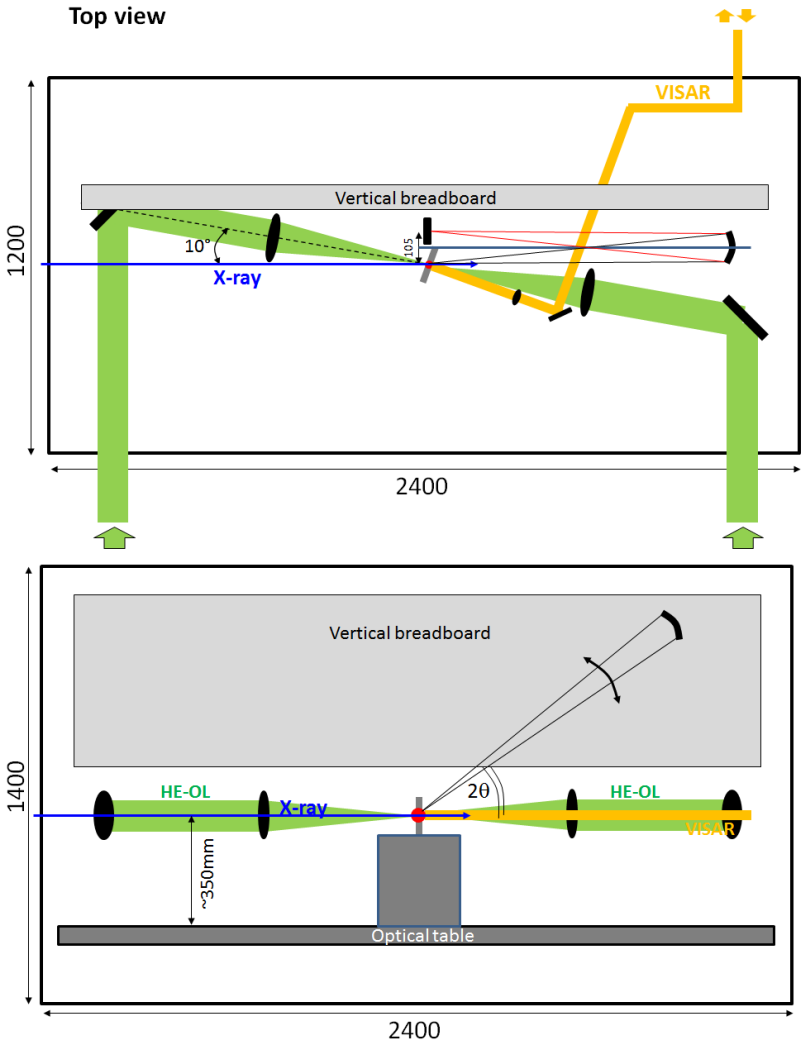

Figure 7-14. *Sketches of a prototypical setup for hr-IXS experiments, e.g. studying acoustic excitations in WDM. The top panel shows a top view and the bottom panel a side view. Two split, synchronized, nanosecond HE-OL beams, each ~ 10 J, λ = 1 µm, counter-propagate to the sample, where the ~ 50 µm focused beams generate WDM conditions at the coalescence point of the two laser-driven shock waves. The HE-OL axis is close to collinear with respect to the X-ray beam. The X-ray beam size on sample is ~ 10 µm. The shock front uniformity is measured by VISAR. All OLs are in the horizontal plane, while the IXS spectrometer operates in the vertical plane.*

7.5.5 X-ray spectroscopy[g]

7.5.5.1 Near-edge X-ray absorption spectroscopy (XANES)

XANES spectroscopy, in general, provides information on the electronic and short-range geometric structure. Typically, spectral modulations above the absorption edge up to ~ 100 eV are analysed for this purpose. Even further above the edge, one speaks about extended X-ray absorption fine structure (EXAFS). In the following, we do not specifically distinguish these two methods and use the term X-ray absorption spectroscopy (XAS) instead.

XAS experiments, in general, require bandwidth and are therefore more difficult to implement for monochromatic FEL sources. Two techniques can be distinguished: In the first technique, a narrow-bandwidth X-ray beam is used to measure the absorption by the sample, and then the photon energy is scanned to establish the photon energy variation absorption signal. This technique has severe requirements for shot-by-shot normalization of the different measurements [32]. A second technique employs an as wide as possible bandwidth of the X-ray beam and a dispersive experiment geometry to detect different photon energies separately. This second technique enables single-shot experiments, which would be a big advantage for the HED instrument, with its requirements to exchange samples after each shot. However, the available bandwidth poses significant limitations on this method.

Recently, the application of the XANES technique for studying WDM states has been shown at a laser-only facility [33]. In that case, the excited state was created by UHI-OL–generated proton beams. However, these experiments were very complex, using three samples for each shot—one for proton generation, one for WDM creation, and one for the generation of the wide-bandwidth X-ray beam—whereas at X-ray FELs, it may be possible to reduce the experiment complexity, eventually even enabling operation at 10 Hz to accumulate data at the highest possible statistical accuracy.

[g] This section is based on the experiment detail description provided by F. Dorchies as well as further discussions with F. Dorchies, M. Harmand, and and A. Ravasio.

The XANES measurement requires very high energy resolution, typically 0.5 eV or better. On the other hand, the efficiency of this measurement is not as important as for other spectrometers due to the use of the direct beam. Therefore, a defocusing geometry using convex crystals can be used to gain high resolution (Figure 7-15). A cylindrically bent single Si crystal recently developed at LCLS [15] is a good candidate for this purpose.

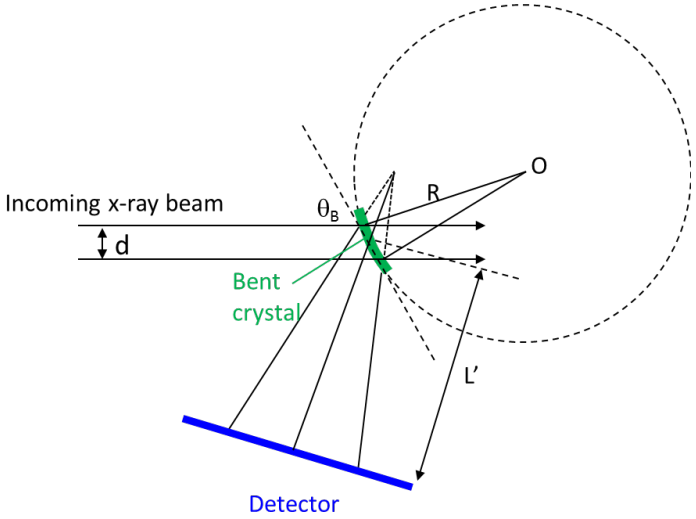

Figure 7-15. *Dispersion geometry of curved Bragg crystal membrane with the shape of a diving board. X-ray beam coming from the left with beam size d. The crystal–detector distance is denoted by L'. More details about this spectrometer can be found in [15].*

7.5.5.1.1 Requirements for optical lasers

Optical lasers are used to heat the sample. In principle, the vertical direction can be used for spectral dispersion. It is therefore crucial to ensure a high homogeneity in optical-laser heating over the probed area along this axis. That is, all X-ray photons in the measured spectrum have to arise from a sample region heated in the same manner. Therefore, the OL beam size (ϕ_{OL}) on the sample should be larger than the X-ray probe size ($\phi_{X\text{-}ray}$) on the horizontal axis.

- High homogeneity in laser heating is crucial.
- $\phi_{OL} >> \phi_{X\text{-}ray}$ on sample in the horizontal dimension.
- Incidence angle is quasi-parallel to the X-ray beam.

- HE-OL: 10–100 J for compression or WDM creation, top-hat and uniform spatial profile, typical spot on sample A_{OL} > 200 µm. VISAR required.
- PP-OL: 1–100 mJ, to heat samples to higher P-T regime; A_{OL} ≥ 100 µm.
- UHI-OL: 100 TW–class. ϕ_{OL} ~ 3 µm for secondary-particle generation.

7.5.5.1.2 Requirements for X-ray delivery

One can benefit from the large X-ray beam size on the analyser crystal (along the dispersive direction) to extend its spectral range. If a sufficient spectral range cannot be covered in a single shot, rotation of the crystal is necessary. Such an arrangement would need reconstruction of spectra, and extremely good references and high stability would be required. The X-ray photon flux may be relatively low, as the direct beam is measured. A collimated beam is required, as divergence degrades the energy resolution.

- X-ray photon energy: up to ~ 12 keV, determined by the absorption edges of the relevant elements in the sample.
- X-ray bandwidth: 10^{-2} (100 eV at 10 keV) will be ideal for XANES measurements. The natural bandwidth of the X-ray FEL beam is ~ 10^{-3}, and special operation schemes to provide larger bandwidth are under investigation.
- X-ray beam pattern on sample:
  - Spatially uniform pattern
  - Beam size: In the dispersive direction of the spectrometers, the beam size should be smaller than that of the OL beam. In the non-dispersive direction, the beam size could be larger than the optical beam size, likewise providing 1D spatial resolution, e.g. to distinguish between heated and non-heated sample regions.
  - A collimated beam using CRL1 can be used, and an adjustable rectangular beam shape on sample should be possible. Slits at different locations can be used to eliminate unwanted diffraction background.
- X-ray divergence: < ~ 10 µrad (~ 10 µm focusing at ~ 10 keV)
- Repetition rate: in most cases, < 10 Hz or pulse on demand

7.5.5.1.3 Requirements for diagnostics and detectors

The stochastic nature of SASE-FEL radiation gives rise to shot-to-shot fluctuations of beam properties, including its spectral content. Therefore, precise knowledge of incident X-ray spectra (reference spectra) on a shot-by-shot basis is crucial for normalization of absorption spectra. The HED group therefore plans to install single-shot spectral monitors (see details in Chapter 4, “X-ray beam transport”). In principle, 1D strip detectors are sufficient, but 2D detectors will also be requested for specific experiments that require definition of the area for the spectral analysis. The detector can be placed in air by using a Kapton window, at the expense of a potential increase of background scattering. The crucial parameters are the selection of the crystal analyser, the analyser–detector distance, and the detector pixel size. Silicon is the obvious candidate for the analyser crystal, due to its crystal perfection. An alternative is high-grade diamond, which has a higher single-shot ablation threshold, excellent thermal conductivity, and higher transparency to the X-ray beam. The drawback is the limited availability of large diamond pieces of high crystalline quality and their cost. The best choice of the material is under investigation.

- Two spectrometers (reference and XAS), ideally identical and symmetric (same distance with respect to the sample, same energy resolution, etc.).
- The reference spectrometer is in the optics hutch (HED-OPT), and the XAS spectrometer is the end of the beam transport in the experiment hutch (HED-EXP).
- 1D detector; 2D detector (CCD) upon request
- Energy resolution: $\Delta E/E \sim 5 \times 10^{-5}$ or 0.5 eV at 10 keV (goal)
- Energy (spectral) coverage: $\Delta E/E < 10^{-2}$ or 100 eV at 10 keV (goal)
- Requirements for the detector:
  - Pixel size: ~ 25 µm, no larger than 50 µm
  - Pixel number: ~ 500 px in spectral dimension
  - Dynamic range: $\geq 10^3$

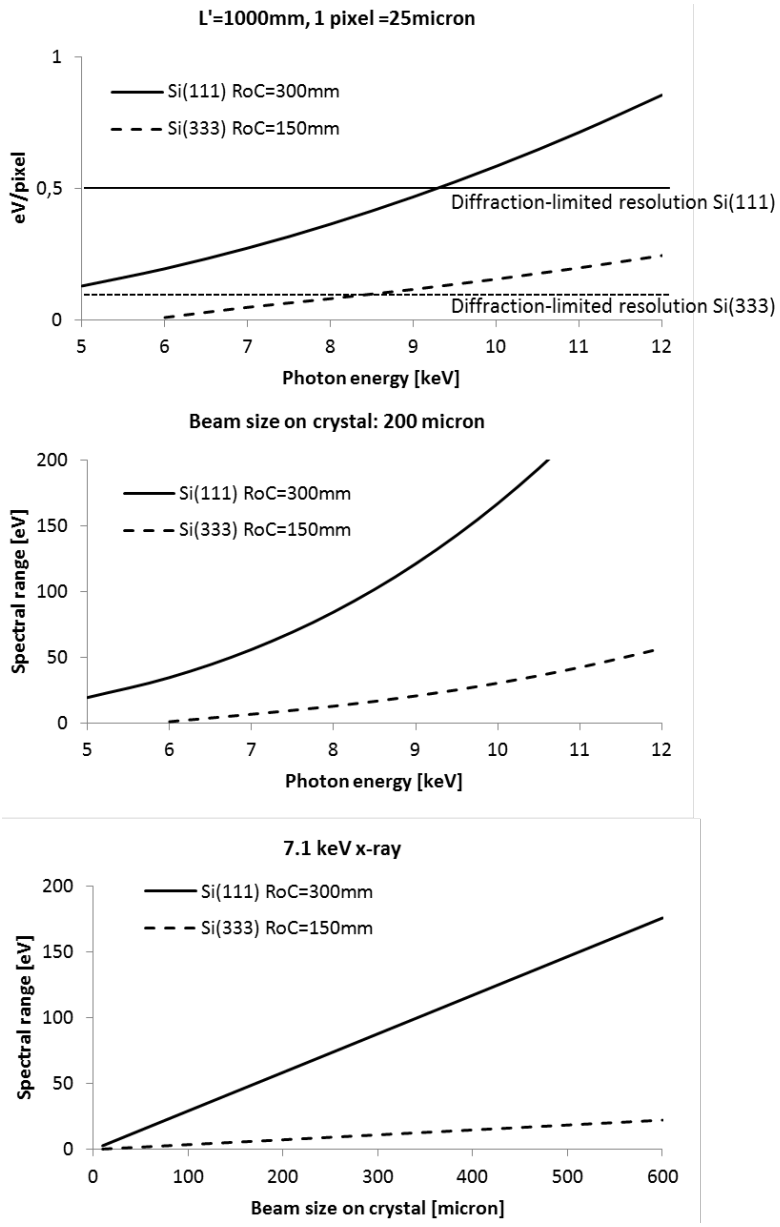

Figure 7-16. Top: *Energy resolution with Si_{111} and Si_{333} reflections. A membrane thickness of 10 µm is assumed. The calculations were done with a beam size of 200 µm and an analyser–detector distance of 1 m. The curvature of the crystal does not affect the resolution much.* Middle: *Spectral range as a function of photon energy. The spectral range is limited by the beam size but not by the detector chip size. A smaller radius of curvature will provide a larger spectral range.* Bottom: *Spectral range as a function of beam size on the crystal at 7.1 keV.*

Figure 7-16 shows several calculations of the spectral range as a function of photon energy. Si_{111} and Si_{333} reflections are chosen as examples, following [15]. A bending radius of curvature (RoC) of 300 mm is chosen for Si_{111}. For

Si_{333}, the doubled amount of bending, i.e. RoC = 150 mm, is chosen to provide a larger energy range. While Si_{333} provides a superior resolution of ~ 0.1 eV, the spectral range is strongly limited despite the larger RoC. In addition, it cannot be used at < 6 keV as the Bragg angle approaches 90°. Si_{111} provides a larger energy range, paired with poorer resolution. To achieve ~ 0.5 eV resolution, the crystal–detector distance *L'* needs to be as large as 1 m, and the pixel size needs to be as small as 25 µm. The resolution is not strongly dependent on the bending RoC. Larger *L'* or smaller pixel size gives better resolution, but the resolution is also diffraction-limited to ~ 0.5 eV for Si_{111} and to ~ 0.1 eV for Si_{333} [17]. The spectral range is limited by the X-ray beam size on the crystal and by the RoC. For the HED instrument, a smaller bending radius seems to better suited to provide a larger spectral range.

7.5.5.2 X-ray emission spectroscopy (XES)

Self-emission spectroscopy is best located at 90° from the X-ray axis, on the horizontal plane, to eliminate the contribution from X-ray scattering. In this technique, the photon energy is determined by the elements in the sample and their excitation state; it is independent of the incident X-ray photon energy. The details of the design of these spectrometers still need to be settled.

7.5.6 X-ray imaging (XI)[h]

X-ray imaging (XI) is applied here as a technique to detect real-space structure and density modulation at mesoscopic to microscopic length scales. Using XI, high spatial resolution can be achieved by either magnified XI in real space or diffractive imaging in reciprocal space. In either case, highest resolution requires tight focusing of the X-ray beam. Therefore, we plan to build a nanofocusing setup for down to 100 nm focal spots for this technique. The device will enable magnified phase contrast imaging (PCI) experiments to be carried out at the HED instrument. Since the method is sensitive to phase changes, the X-ray wave field accumulates while passing through a

[h] This section is based on discussions with A. Schropp and Ch. Schroer.

sample, it is very photon-efficient and allows the imaging of structures otherwise invisible in absorption contrast.

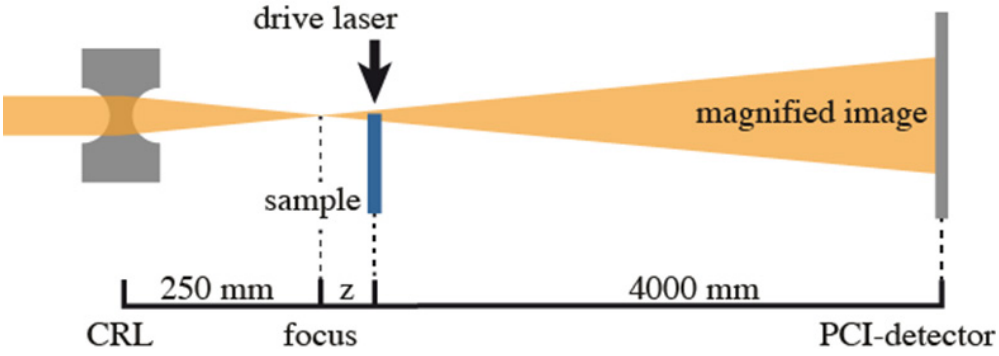

Figure 7-17. *Schematic of the X-ray imaging setup. Note that this is the same schematic as in Figure 4-22 on page 57.*

The imaging scheme is based on an inline arrangement of Be CRLs to focus the X-ray beam, a sample positioned at a distance *x* behind this focus, and a 2D detector further downstream (see Figure 7-17). For a typical value of x = 100 mm, a magnification $M > 60$ can be achieved, which yields a sub-micrometre resolution element per pixel on the detector. ~ 50 nm per pixel were demonstrated at the Matter in Extreme Conditions (MEC) instrument at LCLS.

Since the phase contrast image is a near-field representation of the actual density variation within the sample, the image data have to be numerically processed in order to obtain quantitative structural information. Additionally, the quantitative analysis requires a precise characterization of the nanofocused X-ray beam, which could be achieved by scanning coherent X-ray microscopy (also called ptychography). The latter method yields the complete information on the nanofocused X-ray FEL beam with high spatial resolution, and developments are ongoing to establish the method as a standard characterization tool at X-ray FEL sources [34].

The requirements for XI are similar to those for SAXS. An additional elementary requirement is the nanofocusing optics (Be CRLs), which should be positioned at a distance of 20–30 cm from the centre of the target chamber. Details are summarized in Chapter 4, “X-ray beam transport”. Ptychography requires a high positioning accuracy of the sample stage, which will be

provided by a nanopositioning piezo device. Thermal drifts and mechanical vibrations should be reduced as much as possible.

7.5.6.1.1 Requirements for optical lasers

- HE-OL and VISAR for PCI of dynamically compressed matter
  - HE-OL: ≤ 100 J, top-hat spatial profile, *f*/# = 4–10
  - Incidence angle: ~ 90° with respect to the X-ray beam

7.5.6.1.2 Requirements for X-ray delivery

- X-ray photon energy: 5–25 keV
- X-ray bandwidth: better than 10^{-3} due to the chromaticity of refractive X-ray lenses. A standard Si_{111} monochromator can be used.
- Nanofocusing setup: The focal length of the Be CRLs is about 200–300 mm. Since the sample is typically positioned 100 mm behind the focus, the distance between Be CRLs and sample should be around 350 mm. A linear translation of the Be CRLs along their optical axis is required to accommodate a fixed focus position for different photon energies and to adjust the magnification of the imaging setup.
- Repetition rate: in most cases, 10 Hz limited by the OL repetition rate in high-energy experiments.

7.5.6.1.3 Requirements for detectors

The detector is positioned at a large distance behind the sample. In order to ease the numerical reconstruction of the sample, the optical geometry needs to be adapted to the specific experiment requirements, which depend on the size of the object, the desired spatial resolution, and the photon energy.

- Location of the detector: The detector is located in the forward direction at large distance, e.g. 4 m or more (max. 6.7 m). Window-less vacuum transport is preferred (necessary for ptychography) to reduce X-ray scattering generating background.
- Specification of the detector: A pixel size ≤ 30 µm is preferable for a total chip size of ≥ 30 mm (≥ 1000 px). A dynamic range > 10^3 photons/pixel is

requested. As an alternative to pixel detectors, the X-rays can be converted to visible light by using a ~ 100 µm thick Ce:YAG scintillator screen and imaging the scintillator image onto a scientific CCD optimized for the visible energy spectrum. For this assembly, an increase of the background signal due to readout noise has to be considered. For ptychography applications, a large dynamic range with single-photon detection capability is desirable. However, scintillator-based detectors such as the Princeton Instruments PIXIS-XF: 2048 were also successfully used.

7.6 High repetition rate sample refreshment[i]

The unique combination of capabilities brought together in the HED instrument places correspondingly unique demands on the samples and the equipment needed for sample insertion and alignment as well as on the sample acceptance criteria. The large number of samples that will be destroyed will render unacceptable previously usable materials and configurations. As the HED instrument will be operating in a completely new regime compared to previous light sources or laser facilities, the sample handling solutions will require verification before implementation. The required tests are described in the following sections.

The HED instrument is built to deliver 100 J and 100 TW—with kilojoule energies and petawatt intensities for future work—at a 1–10 Hz repetition rate. These are unique requirements: whereas light sources use much higher repetition rates, they deliver much less energy per shot (≤ mJ), while large laser facilities deliver similar energy but at a much lower rate (~ 10 shots/day). Combining large energy per shot and high shot rate has many consequences that drive the sample requirements. Samples fall into several classes (solid, liquid, and multi-sample) with distinct requirements. We will consider them separately.

[i] This chapter is based on reports and documents provided by and discussions with R. Stephens and C. Deiter.

High-intensity shots using up to a petawatt laser involve focusing the laser to a diameter << 10 µm (FWHM). For dynamic compression experiments, using HE-OL uniform beam intensity over a few 100 µm diameter is required to generate a planar shock wave. For all experiments examined to date, a 300 µm diameter sample is sufficiently large to include diagnostic probe areas and avoid edge effects. This corresponds to an area < 0.1 mm^2 and, in many cases, a 100–200 µm diameter sample would be sufficient. Sample thickness is typically ≤ 100 µm.

7.6.1 Problem of high repetition rate high-energy laser shots

Previous X-ray FEL experiments carried out at high repetition rate have been designed for shots that deposit an energy of a few millijoule per shot. In this case, samples can be placed close together on a continuous sheet of material, allowing many thousands of shots to be taken using a single sheet of samples. For the high energies planned for the HED instrument, solid sample material vaporizes at a distance a few millimetres away from the focal spot, and shock waves are generated that can damage samples many centimetres away. Therefore, the samples must be carefully isolated from one another. Wide separation between shots on a continuous sheet is not an option for experiments aiming at tens of thousands of shots. Spacing samples by 1 cm would require 1 m^2 of sample material per 10^4 shots. Moreover, those 10^4 shots would vaporize ~ 100 mm^3 sample material (assuming 0.1 mm^2 area and 100 µm thickness), and would accelerate un-vaporized bits of the sample (“shrapnel”) into every exposed surface. The vaporized material volume must be minimized and the shrapnel eliminated or at least minimized. Since any structured sample, e.g. diamond-coated high-*Z* foils for equation of state (EOS) experiments, is relatively expensive to produce, the area of sample material needed for a complete experimental campaign must be minimized to keep experiments affordable.

Still, vaporization of the sample material generates a shock that in multi-sample holders has been observed to shatter the holder, destroy distant samples, or both. That problem is addressed by the sample support system. It is feasible to mount samples of the size discussed above on CH or C foils as thin as 30 nm stretched over rather large holes (Figure 7-18). Such a mount

has virtually no areal mass to create shrapnel or vapour, and cannot support an outgoing shock wave that would affect the sample holder or any of the distant samples.

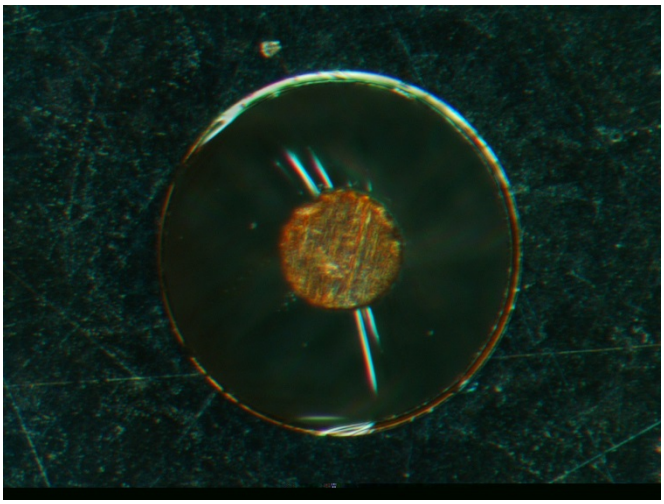

Figure 7-18. *Picture of a 190 µm diameter, 20 µm thick Cu disk supported on a ~ 30 nm thick CH film stretched over a 600 µm diameter opening in a metal disk. The support is robust enough for manually handling the assembly with a vacuum chuck. Photo courtesy of G. Lee (General Atomics in San Diego, California).*

It is also necessary to prevent the laser beam from directly interacting with the sample holder. Laser burn has often been observed on sample holders up to 1 cm from the focal spot; the extent of those marks had been put down to imperfect laser focus. The intensity in a perfectly focused laser beam (an Airy disc) decreases as a power law ($I(x) \sim (2J_1(x)/x)^2 \propto x^{-3}$·sinusoidal function and $x \propto$ angular distance from the centre) rather than the widely assumed Gaussian ($I(x) \sim e^{-x\hat{}2}$). The slower decrease puts significant laser energy at surprisingly large radii. A rule of thumb is that material is vaporized (and a shock generated for $I > 10^{11}$ W/cm^2). When dealing with an intensity at the focus of 10^{21} W/cm^2, for instance, one is concerned with the wings of the focused beam out to $I(r)/I_o \sim 10^{-10}$, which occurs at ~ 1000 times the radius of FWHM of the focused beam or a few millimetres from the focus. And that is the best possible condition; imperfections in the laser pulse wavefront will only make the problem worse. Therefore, adequate spatial confinement of the incident laser pulse is required, and shielding must be employed for sample and sample holder.

Finally, the upcoming samples in the sample holder must be protected from the vapour and heat generated by shots on the preceding samples. For efficient operation, one must load several hours of samples ($O(10^4)$) in the sample chamber on each pump-down. The last sample shot must be as clean as the first. That will require a vapour shield around the sample holder to prevent vapour recondensation. Moreover, a 100 J laser operating at 10 Hz deposits 1 kW of power into the sample chamber. This power must be properly absorbed and removed to prevent samples and mechanics from overheating.

7.6.2 Solid-sample requirements

Many of the above problems can be addressed by mounting minimal-mass samples on ultrathin substrates. Our concept uses mechanical isolation of the sample holder from the samples. In addition, it is necessary to clip low-intensity wings of the laser focus to avoid vaporization of additional sample material. This could be achieved by pinholes fixed to the sample holder. Such pinholes will also protect surrounding samples from the recondensing vapour. Still, the plasma generated in the high-energy experiments may interact with the edges of the sample holder. A study is needed to determine the necessary separation between sample and holder that will sufficiently minimize the transmitted shock.

With the approach outlined above, the requirements for fabricating structured sample material for experiments at the HED instrument will be approximately within the capability of existing sample fabrication shops. Some laboratories have developed their own specialized capabilities, some contract outside laboratories for their needs. As an example, Si wafers can be processed *en masse* and with an extremely wide variety of structures. Sample fabrication facilities, such as SciTech at Rutherford Appleton Laboratory (RAL) in the UK, have developed the capability to produce thin-film samples of specified composition, thickness, and density stretched over ~ 1 mm diameter apertures. To accept sample structures not compatible with Si processing (diamond-tamped high-*Z* foils for EOS experiments, for instance), the Si wafers would be processed as substrates, arrays of thin CH film–covered holes onto which independently made samples would be glued.

By requiring minimal-mass samples. i.e. less than ~ 300 µm diameter, the extant fabrication facilities are acceptable. Sample areas of 10 cm x 10 cm are sufficiently small to be produced by most fabrication apparatuses and, importantly, are sufficiently small to maintain structural uniformity across the sample area, so these would suffice for > 10^4 samples.

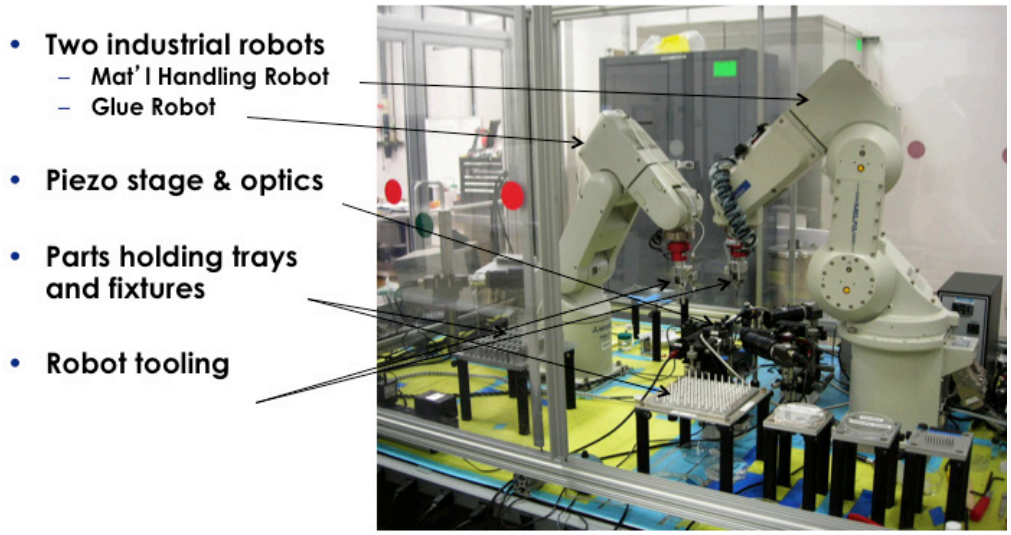

Figure 7-19. *General Atomics sample pick-and-place assembly station. The commercial robotic arms have an open-loop accuracy of ± 20 µm; tooling and other errors add ± 50 µm. Visual feedback allows a positioning accuracy of near ± 1 µm [35].*

Turning that material into samples suitable for insertion will require developing central capabilities to cut the material into sub-millimetre pieces and then to assemble them on carriers suitable for sample handling systems. Such systems, consisting of a laser cutting setup and a pick-and-place robotic assembly system as shown in Figure 7-20, have been used at General Atomics for a number of years; because of the number of shots in current experiments, neither the laser cutting setup nor the pick-and-place robotic assembly system has been pushed as to speed or quantity. The jigs associated with this equipment were, of course, developed to handle a few 100s of samples. It will be necessary to develop dedicated versions of those systems that have a production level that is able to keep up with the shot rate and the capacity to assemble ~ 10^4 samples. If, in an actual campaign, about 10% of the time is spent shooting samples at the maximum rate, the lasers

and robot arms in the current setups would possibly be adequate; the main task would be the development of the material-handling jigs.

In summary, the fabrication of material structures needed for samples exist at a few very well equipped laboratories and therefore could remain the responsibility of each research team. However, since access to these labs and possibly even the cost could be prohibitive, it will be investigated whether centralized sample fabrication will be necessary to ensure the best scientific exploitation of the HED instrument.

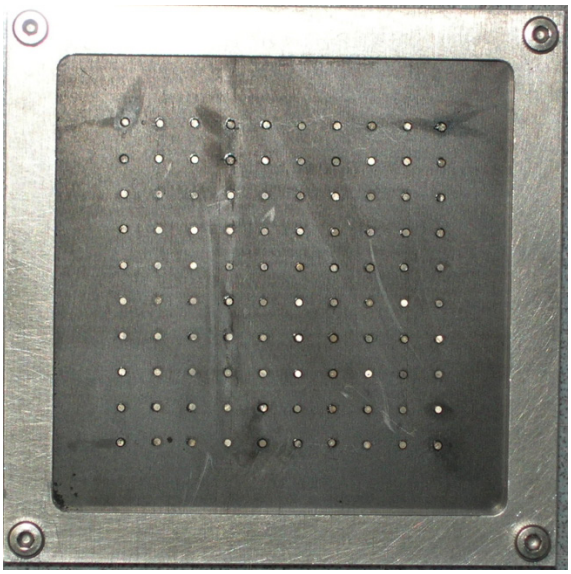

Figure 7-20. *10 x 10 array of laser-cut 300 µm diameter Al–Ni–Cu samples robotically glued to a carbon substrate with < 100 µm uncertainty in xyz [35]*

7.6.3 Liquid-sample requirements

Liquid samples are a very different issue that is worked on in many places due to the newly developed injection techniques for FEL and liquid-chemistry experiments. Furthermore, liquid hydrogen jet and droplet injectors have already been used in FEL experiments. In general, recapture of the injected material is wanted to avoid contaminating the sample chamber. Illumination of the jet using high-energy OLs will vaporize the jets and further disturb the laminar flow of the jet for a much longer period than the laser impact. For this reason, it might be advisable to further develop and employ the droplet-on-demand technology, which reduces the vaporized mass considerably. For the high-energy laser applications at the HED instrument, it needs to be

considered that energy emitted from the interaction region, which is a few 10 kW at a distance of a few centimetres, may eventually damage the liquid injection port. A study is needed to determine necessary protection for the nozzle.

7.6.4 Multi-sample requirements

Complex experiments have been discussed that use a subsidiary sample to convert the laser pulse energy in various ways—to fluorescence X-rays for backlighting, or to protons or neutrons—for subsequent use as pump or probe of the sample to illuminate the physical process of interest. Real-time crystal damage and recovery studies would be in this class. These studies typically require two separate samples to be moved independently. The system described in Section 7.6.2, “Solid-sample requirements”, is necessary for samples to be hit by high energy. Standard practice in current HED experiments is to mount subsidiary samples, like a fluorescence back-lighter, to the main sample on an attached strut. The stalk would create shrapnel and would not likely be amenable to inexpensive, i.e. robotic, assembly; it would therefore not be suitable for the large sample numbers to be shot on this instrument. A more likely solution is to mount the components on separate, suitably overlapped sample handling systems, but that is a task to be postponed until Stage 2.

7.6.5 Sample positioning and replacement

The material evaporated by the high deposited energy is detrimental to all optical surfaces and windows in or near the sample chamber; the high repetition rate will increase the degradation rate by several orders of magnitude compared to current practice. It may be necessary to surround every sample handler with a disposable vapour barrier that has openings only as needed to accommodate fields of view for lasers and diagnostics.

To ensure safe, reliable operation, the sample handling systems must be qualified, maintained, and operated by the facility operators.

7.6.5.1 Solid-sample handling

The sample handler, in addition to satisfying the constraints described in the previous sections, must do each of the following:

1 Accept arbitrary samples—limited only by the experimenter's imagination and the safety constraints of the facility.

2 Put each sample at the laser focal point within the laser depth of focus to a fraction of the focused beam width.

NOTE: It is a separate problem to ensure the intersection of the laser and the X-ray beam as well as to ensure that whatever other beams are used remain steady relative to the laser focus.

3 Allow for at least several hours of operation before opening the sample chamber for resupply, as pump-down will require tens of minutes or more to reach the stated vacuum level of 10^{-7} mbar.

4 Survive exposure to the intense electromagnetic pulse (EMP) created at the laser–plasma interface (LPI) on every shot.

The capability of the sample handling system to handle arbitrary samples is crucial to the success of this device in allowing currently unknown, unspecified, innovative, and ground-breaking experiments. The sample handler must move its samples into position with ~ 10 µm open-loop accuracy at 10 Hz, improved with optical feedback as necessary to ~ 1 µm accuracy. Such sample handlers are nominally available at DESY both as rotary and as 2D raster devices. They typically use Si wafers for the sample array holder; the flatness and rigidity of such wafers minimize the focusing motion (after initial alignment). Rotary holders make efficient use of Si wafers by cutting the wafer into eight vanes to be bolted onto a central hub.

The 2D raster device, with at 10 cm x 10 cm frame, allows the use of four-inch Si wafers to hold a square array of samples. If 3 mm sample spacing is acceptable, each wafer could hold ~ 1000 samples. The sample handler would have to be associated with an adequate-capacity cassette and be designed for the automatic exchange of holders.

Production of the Si wafers is straightforward: sample fabrication labs at HZDR (Germany) and RAL (UK) can handle four-inch wafers. Further existing

equipment can deal with all the depositions needed for many of the sample types as well as for thin substrates to mount those outside the bounds of microelectromechanical systems (MEMS) technology, e.g. diamond-coated metal layers. The bottleneck is the deep etching required for windows that are stretched across thin support films and the separation of the components. Investment in deep reactive ion etching (DRIE) equipment could remove this bottleneck and enable the production of ~ 100 wafers in a week in one lab.

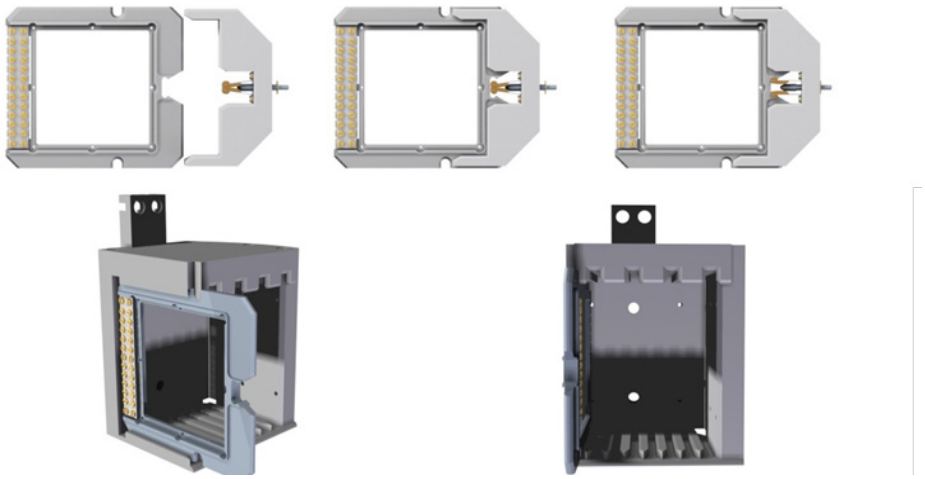

Figure 7-21. Top: *Sample frame concept. The samples are mounted in a frame that can be picked up by a robot arm.* Bottom: *Cassette storage of multiple frames in a separable chamber to allow exchange without venting the main interaction chamber.*

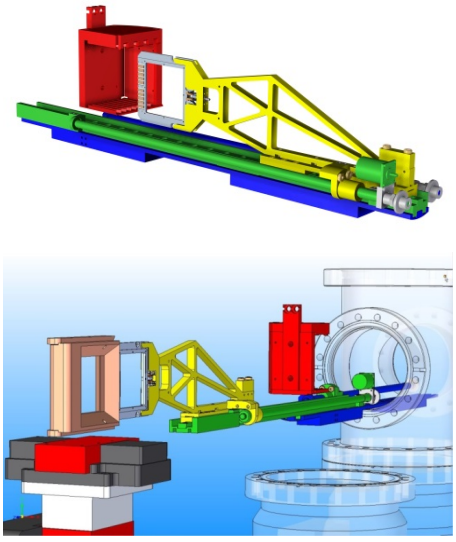

Figure 7-22. *Frame exchange concept developed for the Spectroscopy and Coherent Scattering (SCS) instrument at European XFEL. Courtesy of C. Deiter.*

7.6.5.2 Liquid-sample handling

Liquid delivery systems currently exist; however, these have not been made for operation close to an HED experiment. The problem in this case is the radiation or shock incident on the orifice; it might be necessary to develop a replaceable tip for these devices. And, of course, all electronics and motors associated with them must be ruggedized against EMP.

7.6.6 Safety aspects

For all experiments at the HED instrument, the sample design must be carefully reviewed for compatibility with the operation of the instrument. Experiments done easily at a high rate and a low deposited energy, or at a very low rate and a high deposited energy, might be problematic at a high rate and a high deposited energy. This is due to the much increased mass of evaporated material. Particular attention has to be paid to samples that are hazardous or could be activated under very specific conditions. The evaporated mass will be limited by the sample design described above, but it would still be enough for an element that “bounces”, e.g. Pb, to eventually creep into all parts of a sample chamber and significantly contaminate the chamber. Nuclear activation would become an issue if, in the future, very high intensity shots using the UHI-OL would be performed on high-*Z* materials.

8 Detectors and diagnostics

To observe the physical parameter changes occurring in the systems under investigation at the HED instrument, various detection schemes are used. In this chapter, we describe our current understanding for X-ray area detectors, X-ray spectrometers, optical FDI and VISAR diagnostic methods, and particle detectors to be employed.

8.1 X-ray detectors

As described in the previous chapter, X-ray area detectors will be used for a variety of applications:

- X-ray diffraction (XRD: Bragg, powder, and non-crystalline)
- Small-angle X-ray scattering (SAXS)
- X-ray imaging (XI)
- Spectroscopy

The most important requirements for detectors arising from these applications have been described in the previous chapter and are listed in Table 8-1. There exist further, general requirements for these detectors for employment at the HED instrument. All X-ray detectors need to be protected against visible light and optical laser radiation. Experiments in IA1 typically require that the detectors be mounted inside the vacuum chamber. We are considering, in addition, the possibility of mounting detectors or entire assemblies on flanges, thus placing the vacuum interface at the detector and having the detector electronics in air. While such a configuration eases the detector cooling and its vacuum capability, it also means that the detector will be relatively far away from the sample located at the centre of IA1 (0.6–1.5 m). Large distance corresponds to small solid angle and, therefore,

to small efficiency. For applications at IA2, we plan to mount detectors independently of the instrument vacuum.

Table 8-1. *Detector requirements arising from scientific applications*

	Angular resolution [µrad]	**Pixel**	**Dynamic range**	**Central hole**	**Comments**
XRD (forward)	~ 500	≥ 10^6	High ≥ 10^4	Yes	Single experiments could require all types (Bragg, powder, and non-crystalline scattering) while their requirements are different. In the Bragg case, the beam intensity needs to be reduced.
XRD (large *q*)	1000	≥10^5	Medium ≥ 10^3	No	Diffraction at large angles (e.g. parts of powder rings); detectors close to sample
SAXS	20–50	10^6	High ≥ 10^4	Yes	Forward scattering inside vacuum
XI	20–50	10^6	High ≥ 10^4	No	Similar to SAXS requirements, but without central hole
Spectros-copy	50–100	≥ 10^5	Medium ≥ 10^3	No	Various types for different spectrometers. Using 1D detector enables fast readout.

A special case is the X-ray area detector at large, variable distance from the IA1 sample location required for SAXS and XI applications. This detector needs to be inside the beam vacuum, provides the possibility to measure signal at very small momentum transfer, and needs to let pass the direct X-ray FEL beam in the SAXS case. Whether a single detector without active pixels (hole), a beamstop/attenuator for the direct X-ray beam, or a realization with several detector segments placed around the beam will be used, still requires further investigation.

There are two further requirements for X-ray detectors that are specific to the HED instrument and need to be considered in their deployment and implementation. First, the debris created by the strong excitation and subsequent explosion of the samples should not hit the detector. This requirement is not specific to detectors, as it is also valid for other components inside the IA chamber. But for detectors, it becomes very important due to their high value and the complexity of replacement in case of damage. Second, in particular when employing the UHI-OL, one has to consider the high electromagnetic pulses (EMP), which can damage the

electronics of the detectors. Inside the IA chamber, fields as high as 100 kV/m may be expected (worst-case scenario, linearly downscaled from petawatt laser estimates for the ELI Beamlines facility). On the outside of the chamber, a factor 10 smaller field strength seems possible. The high fields inside the IA chamber pose a significant challenge to all electronic devices. The high degree of electronic integration in a detector head makes these devices particularly sensitive to such electromagnetic interference (EMI). The damage of the devices can be reversible or irreversible, depending on field strength, and switching off devices can help to reduce damage. It is clear that, for all experiments using the UHI-OL, extreme care has to be taken about this issue and that ideally all electronics is removed from the IA chamber, or at least, is switched off. Removing of the electronic devices, including detectors, is in stark contrast to the concept of having the instrumentation inside IA1 as permanent as possible in order to minimize setup and change times. With respect to detector type selection, the EMP/EMI issues do not play a decisive role, as all electronic detectors will be sensitive in a similar fashion. This aspect is more important for chamber layout and detector placement, and possibly for scheduling of experiments.

Taking the requirements from the different applications and building a scenario that can cover most of the requirements, the following implementation would be nearly ideal:

- **Area detectors in or at IA1**
  - 1 large-area (1 Mpx) detector: either centred on the X-ray beam or covering one half-angle; pixel size / angular resolution 70–100 µm / 0.1–0.5 mrad; max. angular range 500 mrad; dynamic range > 10^4; energy range 5–20 keV; low noise; repetition rate 10 Hz; placed inside IA1 at variable distance to sample; for XRD applications
  - 4 medium-area (2 x 128 x 256 or 128 x 512 px) detectors: pixel size 50–100 µm; dynamics range 10^3–10^4; energy range 5–20 keV; low noise; repetition rate 10 Hz; placed inside IA1 at various locations; for spectrometer applications and XRD at large angles

— Additional units of these medium-size area detectors might be required for use in tandem with X-ray emission spectrometers. These could initially be replaced by commercially available X-ray CCDs.

- **Area detectors in or at IA2**

  — 1 large-area (1–2 Mpx) detector: either centred on the X-ray beam or covering one half-angle; pixel size / angular resolution 70–100 µm; angular range 500 mrad; dynamics range > 10^4; energy range 5–20 keV; low noise; repetition rate 10 Hz; outside vacuum at variable distance to sample; for XRD applications

  — 1 medium-area (2 x 128 x 256 or 128 x 512 px) detector: placed on a goniometer arm, the detector will be used to detect certain Bragg reflections and cover a specific θ angle; pixel size 100 µm; angular range of a few mrad; dynamics range > 10^4; energy range 8–16 keV; low noise; repetition rate 4.5 MHz

- **Area detectors at the SAXS/XI station**

  1 large-area (1 Mpx) detector: centred on the X-ray beam; pixel size / angular resolution 70–100 µm; dynamics range > 10^4; energy range 5–20 keV; low noise; repetition rate 10 Hz; placed inside the X-ray beam vacuum, its mount will enable variable distances to the sample position; an open issue is that, for SAXS application, a central hole seems mandatory (highly collimated beam), while for XI applications there should be no central hole.

- **Detectors for the XAS spectrometers**

  — 2 1D (1–2 kpx) strip detectors: pixel size 25 µm; dynamics range 10^3; energy range 5–20 keV; low noise; repetition rate ≥ 1 MHz; placed at locations inside HED-OPT and at the end of the beam transport in HED-EXP; outside vacuum mount on goniometer arm.

  — 2 X-ray CCDs as 2D detectors for these XAS spectrometers will allow alignment of the spectrometers and provide spatial resolution in one direction for specific experiments; mount exchangeable with strip detectors.

Independently of the requirements arising from the experiment detail reports, we will limit the frame rate for X-ray large-area detectors to 1–10 Hz during a first implementation. While some components of the HED instrument will be designed to deal with the much higher repetition rates of up to 4.5 MHz of the X-ray delivery inside the pulse train, we presently do not see the possibility to include into the HED instrument a large-area detector (~ 1 Mpx) based on the technologies developed by consortia on behalf of European XFEL for such a frame rate. This limitation follows from budgetary reasons, but is also linked to the significant challenge to integrate and read out such detectors. However, for specific applications requesting the use of several X-ray pulses of a train, we are preparing the option to employ a tile (128 x 512 px) of the AGIPD detector (see Table 8-2) and also 1D strip detectors, developed at PSI (Switzerland).

Table 8-2. *Possible choices for X-ray area detectors (this list is by no means exclusive and only represents the current understanding)*

	Pixel size [µm]	**Typical number of pixels**	**Comments**
FastCCD (LBNL)	30	1k x 2k	Today, up to 9 keV due to thin 200 µm Si sensor. Optimization for higher $h\nu$ (500 µm Si) is under way. 100 Hz. Day-1 operation seems feasible. Small dynamic range: 1E3 at 2 keV, 3E2 at 6 keV.
MPCCD (SACLA)	50	1k x 1k	Limited energy range capability. > 6 keV due to noise and < 12 keV due to Si sensor thickness (50 µm). 60 Hz. Thicker sensor in preparation.
pnCCD (HLL Munich)	75	0.5–2 Mpx	0.05–25 keV. 200 Hz. 450 µm Si sensor. Dynamic range: 1E3 at 12 keV. High radiation hardness. Availability is unclear.
Jungfrau (PSI)	75	Tiles (128 x 256) up to Mpx	AGIPD electronics with three gains. 3–500 µm Si sensor. ~ kHz. Availability unclear.
CSPAD (SLAC)	110	Tiles (185 x 388) up to Mpx	Latest versions show much improved performance, but production will be stopped as SLAC rolls out a new development (EPIX).
EPIX (SLAC)	50 (?)	Tiles (? x ?) up to Mpx (?)	Parameters and availability to be found out.
AGIPD (DESY)	200	Tiles (128 x 512) up to Mpx	Three gains. MHz intraburst readout. Huge electronics behind. Available in ~ 2016.

The combination of requirements for a decent high frame rate of 1–10 Hz, low noise, high dynamic range for X-rays, and pixel sizes matching the required angular resolution and ranges led to the following conclusion: commercially available detectors (typically of the CCD type) still impose significant limitations on one or several of these requirements. An alternative is recently developed X-ray area detectors using either CCD-type or independent pixel architecture and readout. For independent pixel detectors, only the charge integration technology is possible, likewise allowing the measurement, in a single event, of up to thousands of X-ray photons impinging on a single pixel. In Table 8-2, we provide an overview of some of the detector developments that have been pre-selected for deployment at the HED instrument and introduce some of their most relevant parameters.

8.2 X-ray diagnostics—von Hamos–type spectrometer[j]

An X-ray spectrometer with a resolution of down to $\Delta E/E$ = 0.001–0.01 can be provided by using a cylindrically bent crystal in von Hamos geometry to collect and refocus the X-ray photons onto an area detector.

The most important parameters are summarized here:

- Energy resolution: $\Delta E/E$ = 0.01 for non-collective regime and $\Delta E/E$ = few 0.001 for collective regime
- Geometry: von Hamos
- Crystal: size 30 x 30 mm^2, cylindrical mosaic graphite crystal, lattice constant $2d(002)$ = 6.708 Å, 84 mm radius of curvature
- Range of Bragg angles: 12–23°
  - Sample–crystal distance: 200–400 mm (1D translation)
  - Sample–detector distance: 400–800 mm (1D translation)

[j] This section was written including the results of discussions with U. Zastrau of Friedrich Schiller University (FSU) Jena, Germany

- Scattering angle: ~ 7° – ~ 150° with respect to the X-ray beam in the vertical plane

Requirements for the detector:

- Pixel size: ~ 100 µm
- Chip size: ~ 50 mm (~ 500 px) in dispersive direction and ~ 5 mm for the focusing direction (perpendicular to dispersion)
- Readout: 10 Hz
- Dynamic range: ~ 10^3

Von Hamos–type spectrometers using mosaic crystals are being considered for use at the HED instrument. A mosaic spread leads to higher reflectivity compared to that of perfect crystals. Mosaic crystals are made up of numerous small perfect crystallite domains of micrometre and sub-micrometre size, which are oriented almost parallel to one another. Highly oriented pyrolytic graphite (HOPG) [36] is an artificial graphite with a mosaic spread of about 0.4° at a thickness of 100 µm. Highly annealed pyrolytic graphite (HAPG) provides a smaller mosaic spread, thus gives higher energy resolution but also lower reflectivity than HOPG. A schematic setup of the von Hamos spectrometer geometry diagnostic is shown in Figure 8-1.

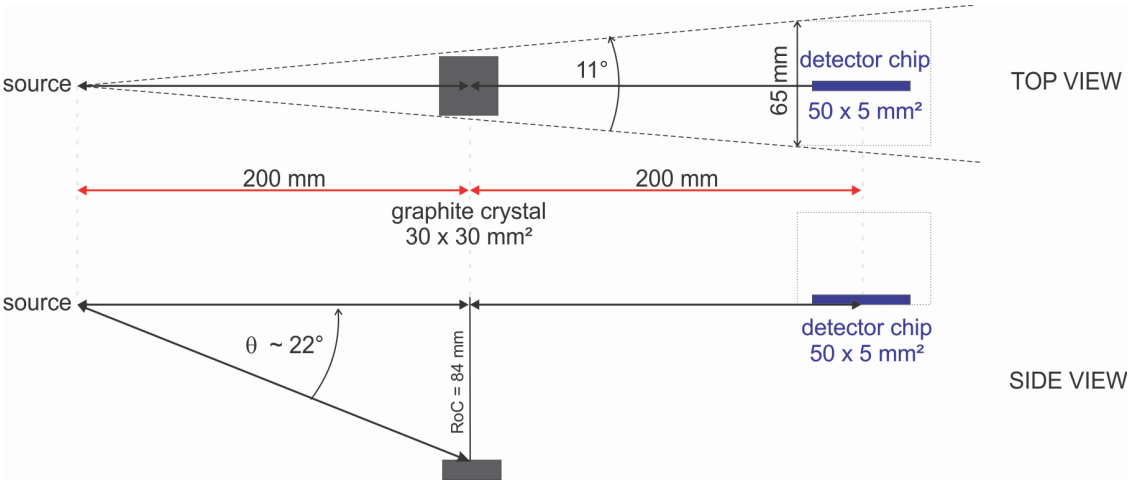

Figure 8-1. *Schematic setup of von Hamos–type spectrometer considered for use at the HED instrument. The setup shown is for smallest distances / largest Bragg angles at 5 keV (002, first order) or 9.5 keV (004, second order). The distances source–crystal and crystal–detector must match. Courtesy of U. Zastrau (FSU Jena).*

A crystal size of 30 x 30 mm^2 will provide sufficient spectral range for all experiments at a single photon energy, e.g. ~ 600 eV bandwidth at 5 keV. To cover various photon energies, the distances source–crystal and crystal–detector both need to be adjusted. This can be achieved using a 1D translation.

The current design is optimized for a source–crystal distance from 200 mm to 400 mm. This change in distance is necessary to adopt Bragg condition for different photon energies. This reconfiguration can be achieved by sliding the whole spectrometer box with fixed crystal. In addition, one needs to move the detector by the same distance with respect to the crystal. Keeping the Bragg angles larger than, but near 13° relative to the surface is desirable to avoid depth broadening due to deeply penetrating X-rays, which degrades the resolution [37]. In addition, detecting very high photon energies leads to Bragg angles much smaller than 13°, and instead, we will employ second- (004), or third-order (006) reflections. Altogether, this arrangement will allow us to keep the Bragg angle between 12–23° (Figure 8-2) and an overall distance source–detector of < 800 mm.

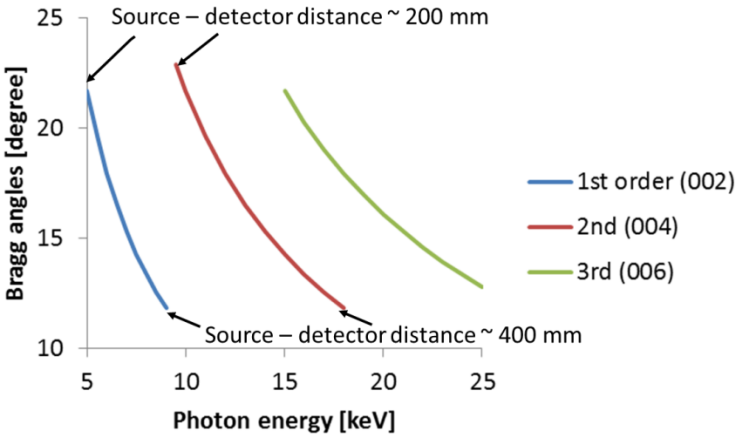

Figure 8-2. *Bragg angles as a function of photon energies. Cylindrical graphite crystal is assumed. High photon energies resulting in Bragg angles smaller than 13° will employ second- (004) or third-order (006) reflections.*

Focal aberrations on the detector depend on the crystal mosaicity and the *f*-number of the optics [36]. Depth broadening due to shallow incidence angle also gives energy spread on the detector. When those are taken into account, the point spread function for monochromatic X-rays in the 5–25 keV range is

on the order of a few 100 µm on the detector (Table 8-2). Therefore, detector pixels smaller than 100 µm will not improve the overall resolution.

Table 8-3. *Energy resolution and size of the point source on the imaging point for 5–25 keV photon energy obtained from ray-tracing calculations. A cylindrical 100 µm thick HAPG crystal (mosaicity 0.14°, radius of curvature 84 mm) is assumed. Higher photon energies use higher-order reflections.*

Photon energy [keV]	***hkl***	**Dispersion [µm/eV]**	**Resolution [eV]**	**Spectral point spread function [µm]**
5	002	100	5	500
10	002	90	15	1300
10	004	50	13	650
15	004	45	22	1000
20	006	25	24	600
25	006	20	30	600
25	008	20	15	300

Concerning the detector chip size, ideally the dispersive direction needs to be twice as long as the crystal length to cover the entire spectral range given by the crystal. In most cases, full coverage is not required, thus ~ 50 mm length may be a reasonable requirement. For the focusing direction, 5 mm width is enough to cover a large fraction of the scattering X-rays (see Figure 8-3). A wider detector will collect only photons that are not properly focused by the crystal, but smeared out in an X-shaped aberration pattern [36].

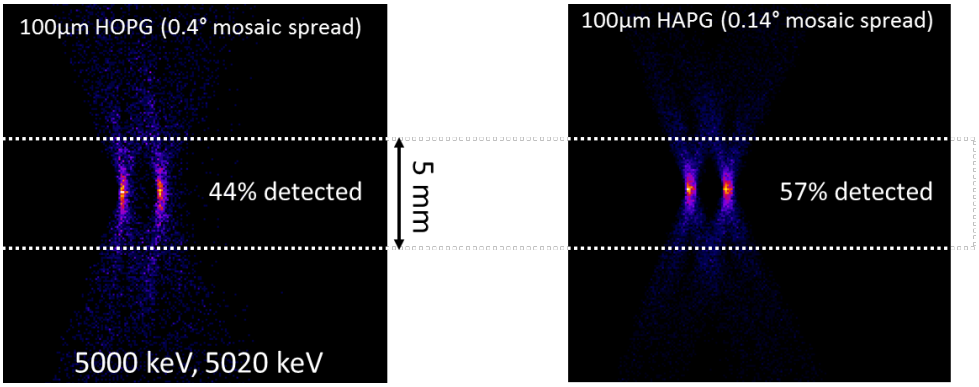

Figure 8-3. *Monte Carlo ray tracing for mosaic crystals [36]. A 5 keV monochromatic point source is assumed. The focal aberration depends on mosaicity and f-number of the crystal. HOPG (left) has larger mosaicity, resulting in higher reflectivity but severe aberrations. HAPG (right) provides better focusing. The energy spread (due to depth broadening) can be mitigated by reducing the thickness of crystal. Courtesy of U. Zastrau (FSU Jena).*

8.3 Optical diagnostics

This section describes FDI and VISAR.

8.3.1 Fourier domain interferometer (FDI)[k]

FDI enables both the amplitude and the phase of the complex reflection coefficient of an excited solid to be measured with high spatial and temporal resolution in a single shot. These quantities are closely related to both the optical properties of the probed sample and its hydrodynamic evolution.

At the HED instrument, the FDI will be used to characterize solids excited by the X-ray FEL beam, by optical lasers or eventually even by laser-induced particles (e.g. protons). When using the optical laser as excitation source (pump), the diameter of the pumped area of the sample can be fairly large, i.e. 10 to a few 100 µm. In contrast, the X-ray FEL pump scheme requires very tight focal spots, i.e. less than a few micrometres, as otherwise the X-ray

[k] This section was written including the results of discussions with C. Fourment, F. Dorchies, and J. Gaudin of Centre Lasers Intenses et Applications (CELIA) in Bordeaux, France.

intensity is not sufficient to create highly excited solid or warm dense matter for larger focal spots. Usually, the probe beam size on the sample is several times larger than the spot size of the pump beam in order to be able to consider uniform illumination over the excited region.

Table 8-4. *Typical parameters required for FDI for various applications*

	Area to study (similar to or larger than the pump beam size on sample)	**FDI beam size on sample**	**Spatial resolution needed**	**Temporal resolution needed**
X-ray pump	< few µm	Few 10 µm	~ 1 µm	~ 10 fs
Optical (~ mJ) pump	Few 10 µm	~ 100 µm	~ few µm	~ 10 fs
UHI-OL–induced particle pump	>100 µm	~ 1 mm	~ 10 µm	~ 100 fs
UHI-OL pump	> 100 µm	~ 1 mm	~ 10 µm	100–1000 fs

8.3.1.1 Types of FDI

There exist two types of FDI techniques. The chirped-mode FDI [4] gives the complete time history in a single shot, but with poor temporal resolution. Non-chirped FDI [5] requires multiple shots to obtain the time history, but the temporal resolution is limited only by the probe pulse duration, which is ~ 20 fs in our case. The HED instrument provides high-repetition (≥ 10 Hz) capability, and achieving ultrahigh temporal resolution is one of the most important aspects for various applications. Therefore, the non-chirped mode FDI better suits the overall HED instrument scope.

The chirped-mode FDI, also called TASRI [38], uses chirped beam. The final temporal resolution, which is now limited by the chirped pulse duration τ_{chirp}, is expressed by $\sqrt{\tau_{\text{chirp}}\tau_{\text{compressed}}}$.

For the non-chirped FDI, also called twin probe configuration, the probe pulse is divided into two arms to generate the probe and reference pulses, which

are separated temporally. The reference pulse irradiates the sample surface before the excitation pulse, and the second pulse probes the sample after excitation. The two pulses interfere because of the dispersion of the spectrograph grating, acting as pulse stretcher to make the pulses overlap in time. To obtain a complete time history of the perturbation under study requires *multiple shots,* but the temporal resolution is limited only by the probe pulse duration.

8.3.1.2 Requirements for the probe laser

The PP-OL will be used as a probe beam for the FDI system. This laser provides ~ 20 fs pulse duration, ~ 60 nm bandwidth, maximum pulse energies of 3–5 mJ, and infrared wavelength (λ ~ 800 nm). The probe beam flux on the sample should be lower than the damage threshold of the sample, which is around a few 0.1 J/cm^2 for femtosecond duration pulses. Assuming a probe spot size on the sample of ~ 100 µm, a required fluence of 0.1 J/cm^2 corresponds to 10 µm pulse energy. Thus, the PP-OL has largely sufficient pulse energy for the FDI system.

8.3.1.3 Probe beam transport

The PP-OL transport up to the entrance of the HED-EXP is summarized in Chapter 5.1.3. Inside HED-EXP, the beam can be converted to the second harmonic (2ω ~ 400 nm) or third harmonic. The shorter wavelength improves the signal-to-noise (*S*/*N*) ratio of the signal and also the spatial resolution. For FDI applications, the beam will be separated into two polarization states (*s*- and *p*-polarization). One of the two arms accommodates an additional delay line to compensate the optical path length difference between the two arms after splitting. The beams are focused by achromatic lenses with focal lengths of > 1 m, giving a far-field diameter on sample of a few tens of micrometres. Larger beam sizes can be achieved by defocusing. The two beams can either illuminate the same surface of the sample, which allows polarization-dependent measurement, or one beam each illuminates the front and the rear surfaces to measure the uniform expansion of the sample following X-ray excitation.

8.3.1.4 Imaging system

The spatial resolution is limited by the numerical aperture of the collecting lens inside the experiment chamber. The highest resolution of ~ µm level needs a microscope objective close to the sample. While a relatively large working distance objective is now available, optics damage due to sample debris or laser power will be an issue, even at large distances. This scheme will thus be realistic only for X-ray pumping or for low-energy optical laser pumping experiments. Alternatively, an achromatic lenses with *f*/# ~ 3 can be used, albeit at the cost of lower resolution on the order of ~ 5 µm.

8.3.2 VISAR

VISAR [39], an optical reflection technique measuring the surface motion [40], allows the determination of the shock breakout timing and shock velocity. It requires 10–50 ns duration, temporally coherent probe laser pulses. The required laser energy is ~ 1–10 mJ. Commercially available lasers can be used (for example, “Quanta-ray” Nd:YAG, *Q*-switch laser). The laser will be installed inside HED-EXP. Details can be found in the HED CDR [1].

8.4 Particle detectors

The scintillator-based online detector shown in Figure 8-4 consists of two units, the scintillator unit itself and the CCD camera unit. The scintillator unit houses the central element for proton detection, which is a stack of 10 scintillator layers, each 50 mm iwide, 40 mm high, and 350 µm thick. The scintillation material is the polyvinyl toluene–based plastic scintillator BC418 from Bicron with a central emission wavelength of 391 nm. Protons hitting the 10 mm high and 50 mm wide detection area of the detector pass through the scintillator stack and deposit energy in each layer until they stop in the stack depth that corresponds to their energy-dependent range. The energy deposited in each layer is converted into scintillation photons that are emitted isotropically. As in a light guide, these photons are guided through the 350 µm thick layers from the detection area towards the scintillator edges by total internal reflection (critical angle θ_c = 39.3°) at the polished scintillator

surfaces. The light emitted at the upper scintillator edge is imaged onto the CCD camera located above within the unit. This design allows for a very slim scintillator unit that is only 15 mm thick by 76 mm wide overall, so that the detector can be arranged close to the proton source or in any other tight experiment setup. The total height of the detector including the CCD camera housing is 310 mm, and it has a footprint of 80 mm by 80 mm.

In order to obtain a good spatial separation of the different scintillator layers in the imaging plane, the scintillator stack is set up as a fan with the layers being in contact in the detection area and separated by 300 µm thick spacers at the upper layer edge (see Figure 8-4). Cross talk between different scintillator layers via the scintillator surfaces is avoided by covering each layer with 13 µm thick light-tight black plastic foil. Furthermore, the aluminium case of the scintillator unit is lined with black light-absorbing foil to avoid reflections and scattering inside the case. A representative detector image measuring laser-accelerated protons is shown at the top of Figure 8-4. The individual scintillator layers are well resolved, and the deepest layer showing signal provides a measure of the maximum proton energy in the pulse. The resolution of the maximum proton energy is determined by the thickness of the scintillator layers, which was chosen to yield a resolution below 1.5 MeV above a proton energy of 12 MeV, as summarized in the table included in Figure 8-4. In the lateral direction, the signal from each layer corresponds to the angular distribution of the proton distribution in horizontal direction (parallel to the scintillator edge) integrated over the vertical dimension of the detection area. Usually positioned 50 mm behind the source, the detector captures a proton distribution with a divergence half-angle of up to 26°.

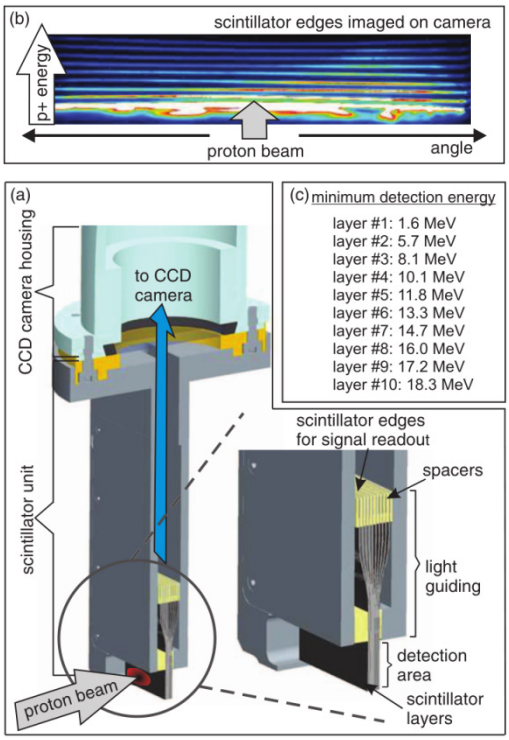

Figure 8-4. *(a) Protons irradiating the detection area pass through the stack of 10 thin scintillator layers and deposit an amount of energy characteristic of their initial energy in each individual layer. The produced scintillation light is then guided towards the upper scintillator layer edge in each scintillator layer and imaged onto a CCD camera installed in the CCD camera housing. The online detector resolves 10 different energy layers and offers angular resolution of the proton distribution along the horizontal dimension of the detection area. (b) Raw data showing the scintillator edges imaged onto the CCD camera. The lateral direction resolves the angle, and in the vertical direction the distinct scintillator layers can be seen. The light output of the scintillator layers as a measure of the deposited proton dose is encoded in a colour table ranging from white to blue for decreasing signal intensity. (c) The table summarizes the minimum initial energy a proton needs in order to reach a specific scintillator layer, which was simulated using the Stopping and Range of Ions in Matter (SRIM) software packages.*

Appendix

This appendix describes the operational modes at the European XFEL, the heat load studies carried out by the X-Ray Optics and Beam Transport group (WP73), and the HED advisory review team (HED-ART) report on this TDR.

A.1 Operation modes at the European XFEL

Table A-1 lists the proposed definition of beam modes at the European XFEL.

Table A-1. *Proposed definition of beam modes. The numbers indicate the maximum number of allowed pulses within one pulse train. Modes highlighted in green were proposed for the accelerator, while the others are additionally proposed for the X-ray beamlines.*

	≤ 0.1 nC	**≤ 0.25 nC**	**≤ 1 nC**	**> 1 nC**
Mode 1	1	1	1	1
Mode 2	600	200	30	1
Mode 3	2700	1350	200	10
Mode 4	2700	2700	< 2700	< 2700

Mode 1: Basic commissioning mode of accelerator, beam transport, and experiments. With one pulse per pulse train (10 Hz operation), even a miss-steered beam should not be able to destroy components of the beam transport.

Mode 2: Basic commissioning mode of the accelerator with pulse trains (30 pulses). For the beam transport, the X-Ray Optics and Beam Transport group (WP73) propose to make this mode charge-dependent, so it can be used to run experiments with a diamond window in air (FXE and MID).

Mode 3: This mode is defined by the beam transport. It is essentially defined by the number of pulses that a water-cooled piece of B_4C can absorb without

being damaged. Also, the hard X-ray monochromator and Be lenses work only up to Mode 3.

Mode 4: Full beam: the beam power is only limited by the performance of the accelerator and the electron beam dumps. Typically, only the totally reflecting mirrors can handle this beam power. X-ray beam loss monitors have to be operational and fully commissioned to reach this mode.

A.2 WP73 heat load studies

The X-Ray Optics and Beam Transport group (WP73) carried out analytical and finite element analysis (FEA) studies of the materials response to the heat loads generated by the radiation fields arising during typical operational modes. These studies can be found in Ref [41].

A.3 Report from the HED-ART on the TDR

The HED advisory review team (HED-ART) met on 19 March to discuss and review the TDR for the HED instrument. For this purpose, the HED-ART had received a preliminary version of the TDR several days before the meeting. At the meeting—which R.W. Lee chaired and in which P. Audebert, A. Higginbotham, H.-P. Liermann, D. Neely, P. Neumayer, K. Sokolowski-Tinten, and S. Toleikis participated—the HED group provided presentations of the major subsystems.

T. Tschentscher first gave an introduction and reviewed the construction progress. He indicated issues of a technical nature with Cu-plating parts of RF couplers and other delays in the accelerator construction that will extend the timeline for the European XFEL completion. P. Audebert raised the question about the specifications for air conditioning control in the laser rooms, which should be on the order of 0.1°.

Next, T. Tschentscher provided an overview of the HED instrument design. He emphasized the capability of the HED instrument to enable a wide class of X-ray techniques and science applications. He stressed that the issue of

sample production needs to be clarified beyond the TDR. T. Cowan commented that contributions to the HED instrument through the HIBEF user consortium (UC) may cover this aspect. However, this will need to be defined. The issue of detectors was addressed, and it was mentioned that, for SAXS applications, the detector would need to be moved between different positions. J. Hastings asked why not two detectors, which would require less movement. Civil construction of the HED experiment hutch has started, and a tunnel for future connection to an external laser building has been completed. The walls of the experiment room need to be very thick due to PW laser generation of MeV particle beams. Details of a few experiment configurations were provided.

It was emphasized that several items remain to be defined soon to complete the TDR. These include sample replacement strategies and detectors as the two most prominent ones.

With respect to risks, the following assessments were presented:

- X-ray optics: Small risk. Pointing stability, throughput, etc.
- Ultrahigh-intensity optical laser: While a modest risk exists for the procurement of such a system, the operational aspects could involve a higher risk.
- High-energy optical laser: Medium risk. First prototype exists for ELI; European XFEL gets a second one, so kinks should be worked out.
- Sample fabrication: Medium risk. The ART noted that this risk depends very much on the desired shot repetition rate and efficient utilization of the available beamtime. For efficient utilization, a high shot rate may be needed and, for such experiments, special sample schemes need to be developed, therefore creating a significant risk.

The following issues were raised by the ART:

- P. Audebert noted that the pointing alignment issue is the same for optical and X-ray lasers.
- D. Neely emphasized that activation is an issue that can be easily dealt with but that nevertheless requires attention. The activation decays with

time after the last high-intensity laser shot. If one needs to access the chamber in a time much shorter than the decay time of the activated matter (i.e. chamber, sample holders, equipment, etc.), there could be issues whereby experiment turnaround times were substantially prolonged, leading to a decrease in experiment capacity.

- J. Hastings stressed that three instruments at the SASE2 beamline will be important for an efficient turnaround.

The following presentation by T. Cowan introduced the status of the HIBEF UC. He emphasized the complexity of the consortium organization, which is non-standard, as HIBEF comprises both people and money from various agencies. Los Alamos National Laboratory (LANL) in Los Alamos, New Mexico, has signed a memorandum stating that it will significantly contribute to the HIBEF UC. Cowan reported that the contribution of a 100 J diode-pumped laser by the UK is now funded at the 8 M€ level and further stressed that HIBEF would allow funding of the HED instrumentation were the baseline funding to be exhausted. The ART acknowledged the impressive progress in building the HIBEF UC.

Next, K. Appel introduced X-ray optical components and monitors. She showed schematics of beamline components and mentioned that the mirrors with Pt coating could be used for energies as high as 60.7 keV. Also, the possibility for 1 Hz pulse picking between HED and MID was introduced. In response to a comment from the CDR review, the configuration of the CRLs was re-analysed, and six CRL configurations were shown to fulfil the experiment requirements of different focal spot sizes from ~ 1 μm to > 100 μm. The ART discussed the issue of pointing stability, given the mechanical holder of the CRLs, and emphasized this point. It was reported that this matter was already being addressed internally as being very important. K. Appel also reported on the special configuration for two-colour experiments. Transport of the first- and third-harmonic radiation pulses and a delay with respect to each other present a challenge and special case for the X-ray transport system. The pulse picker uses a rotating-disc design, and beam monitors were presented in the context of the beamline layouts.

Next, G. Priebe introduced the high-power optical laser systems and their integration. He reiterated that both the 100 TW / 10 Hz and the 100 J / 10 Hz lasers will be supplied by external groups. He then discussed the two vendors, Thales and Amplitude, as well as laser possibilities for the 100 TW system, and proposed as one modification to keep the dazzler feedback loop on all the time. The 100 J laser provided by Rutherford Appleton Laboratory (RAL) in the UK was mentioned. As part of this presentation, P. Neumayer presented information about the long-pulse laser at GSI Helmholtzzentrum für Schwerionenforschung in Darmstadt, Germany, for which pulse shaping is an important but soluble problem. He stressed the need to have a good ramp generator. P. Audebert asked about getting the 100 J laser into the chamber, i.e. the relaying of the beam. T. Cowan asked if anyone had information about the Thales laser pulse contrast, as all the known Thales lasers are used for wakefield generation. P. Audebert mentioned that he would try to find out. Furthermore, the ART emphasized the need to provide a figure for residual changes in the beam when used for long periods of time. This needs to be a specification in the requirement to instrumentation (RFI). A discussion ensued about building a propagation system that could handle larger beams, which, though not needed for the on-sample spot size for the contemplated experiments, could be extremely useful, e.g. to minimize damage on the large grating. This would have the advantage of reducing the thermal loading and thus enhancing the lifetime of the components substantially.

Finally, M. Nakatsutsumi introduced the optical laser transport for the four lasers—UHI-OL, HE-OL, PP-OL I, and PP-OL II—and the experiment geometries and chamber arrangement. Each setup for the possible laser combinations was discussed, and the implementation of phase contrast imaging (PCI) was presented. After this presentation, a general discussion began. T. Cowan noted that target alignment capability was not mentioned. J. Hastings, H.-P. Lehrmann, D. Neely, and K. Sokolowski-Tinten discussed the detector choices, indicating that some further effort may be needed. In response to a comment about detector hardness to electromagnetic pulse (EMP), D. Neely pointed out that there are mitigation techniques for EMP. However, operation of detectors in such a high-power laser facility will lead to frequent EMP issues with detectors and electronics. In this context,

emphasis was put on several other requirements, e.g. beam overlap, access to the various components of the instrument, and others.

There ensued a discussion concerning the place that the TDR takes in the advancement of the project. This was explained by the HED group to be necessary for advancing the HED construction to the next level. The HED group further stressed the necessity of a review and agreement on the issue of a fixed interaction point. It was stressed that only this design, to present knowledge, could enable a fast, two-day turnaround of different experiments. On this issue of a fixed interaction point, some discussion arose, in particular due to the desire to bring different types of large-area detectors close to the sample for diffraction-type experiments. The HED group emphasized that they are aware of this issue and of the apparent limitation of the current interaction chamber design. However, the selection and placement of detectors was not yet final and still required more work. The requirements for diffraction experiments had been identified and had not changed, and the final implementation of the HED instrument would respond to these requirements.

Summary

The ART considers the progress achieved by the HED group and reported in the HED TDR impressive. During the previous review, the HED group was asked to engage various users to submit their ideas for their experiments and define the equipment, constraints, and special requirements. This information was solicited, and the HED group incorporated the experiment concepts into the TDR. The results of the HED group's efforts were embodied in the set of talks presented at the ART meeting, which clearly indicated the amount of effort expended on the details of the experiment planning.

Acknowledgements

This technical design report was written by the HED group—Motoaki Nakatsutsumi, Karen Appel, Ian Thorpe, and Thomas Tschentscher—with substantial contributions from Gerd Priebe (Optical Lasers group), Alexander Pelka (HIBEF user consortium), and Bruno Muller (LULI).

First of all, we would like to express our very great appreciation to the HED advisory review team—Richard W. Lee (chair), Patrick Audebert (LULI), Andrew Higginbotham (U. Oxford), Hae-Ja Lee (SLAC), Hanns-Peter Liermann (DESY), David Neely (STFC), Paul Neumayer (GSI), Klaus Sokolowski-Tinten (U. Duisburg), and Sven Toleikis (DESY)—for their time, input, and thorough review of the present TDR.

Chapter 7, “Experiment chamber setups”, was developed with the help of experiment detail descriptions provided by Klaus Sokolowski-Tinten, Andrew Higginbotham, Paul Neumayer, Giulio Monaco, Martin von Zimmermann, Richard W. Lee, Jerome Hastings, Zuzana Konopkova, Emma McBride, Alexander Pelka, Hans-Peter Schlenvoigt, and Stewart McWilliams. We thank them for these most valuable contributions.

We wish to thank Thomas E. Cowan (HZDR), the coordinator of the HIBEF UC, and Anna Ferrari (HZDR) for their substantial contributions to the radiation shielding layout and simulations for the UHI-OL.

We thank the Optical Lasers group, led by Maximilian Lederer, and especially Guido Palmer for their substantial advice on optical laser integration and PP-OL beam transport design. We also thank Ulrich Schramm (HZDR) and Toma Toncian (U. Düsseldorf) for their contributions and advice on UHI-OL integration. We would also like to thank John Collier and Klaus Ertel (STFC-RAL) for their contributions to the description of the DiPOLE laser.

We are very grateful to Harald Sinn, Martin Dommach, and Fan Yang of the X-Ray Optics and Beam Transport group for their very important input to the definition of our X-ray beam transport design.

We thank Wolfgang Tscheu, Lewis Batchelor, Antonios-Vassilios Lalechos, Viktor Lyamayev, and Osama Ahmed Salem of the Central Instrumentation Engineering group for the realization of various device designs presented in this report.

We thank Jan Grünert of the X-Ray Photon Diagnostics group for giving us advice on X-ray beam monitor systems.

Tobias Haas, Gerd Wellenreuther, and Niko Saaristo in the Photon Systems Project Office, and Bruno Becker-de Mos in Technical Services provided substantial support on hutch designs and infrastructures.

We thank the MID instrument team—Anders Madsen, Thomas Roth, Jörg Hallmann, and Gabriele Ansaldi—for substantial contributions on shared issues, i.e. the CRL realization, hutch layout, and many others.

We would also like to extend our thanks to the Detector Development group, especially Markus Kuster and Jolanta Sztuk-Dambietz, for their valuable advice and comments on detector choice.

The split and delay unit is designed and developed by Sebastian Roling and Helmut Zacharias (U. Münster). We thank them very much for their initiative and contribution.

We thank Sigrid Kozielski, Eric Boyd, and Sabrina Scherz in the Safety and Radiation Protection group and Albrecht Leuschner from DESY for their careful advice on safety concepts, especially on radiation shielding and the realization of the experiment enclosure.

We thank Joachim Schulz, Carsten Deiter, and Sadia Bari of the Sample Environment group, as well as Richard Stephens (General Atomics), for their contributions to the sample handling strategy.

In addition, we acknowledge most helpful discussions with and suggestions from Beata Ziaja and Nikita Medvedev (DESY); Ulf Zastrau (U. Jena); Fabien Dorchies, Jérôme Gaudin, and Claude Fourment (CELIA); Marion Harmand and Alessandra Ravasio (LULI); Andreas Schropp and Christian Schroer (TU Dresden); and Jon Eggert (LLNL).

We would like to thank many other colleagues at European XFEL for fruitful discussions and contributing ideas: Christian Bressler, Nicola Coppola, Andreas Galler, Wojciech Gawelda, Adrian Mancuso, Tommaso Mazza, Michael Meyer, Liubov Samoylova, Andreas Schertz, Joachim Schulz, Jinxiong Wang, and Christopher Youngman.

Finally, we thank Kurt Ament and Ilka Flegel for assistance in formatting and proofreading this report.

References

[1] M. Nakatsutsumi, Th. Tschentscher: “Conceptual Design Report: Scientific Instrument High Energy Density Physics (HED)”, XFEL.EU TR-2013-003, doi:10.3204/XFEL.EU/TR-2013-003

[2] P.M. Celliers et al.: “Line-imaging velocimeter for shock diagnostics at the OMEGA laser facility”, Rev. Sci. Instrum. **75** 4916 (2004) doi:10.1063/1.1807008

[3] J.E. Miller et al.: “Streaked optical pyrometer system for laser-driven shock-wave experiments on OMEGA”, Rev. Sci. Inst. **78** 034903 (2007) doi:10.1063/1.2712189

[4] J.-P. Geindre et al.: “Single-shot spectral interferometry with chirped pulses”, Opt. Lett. **26**, 1612 (2001) doi:10.1364/OL.26.001612

[5] J.-P. Geindre et al.: “Frequency-domain interferometer for measuring the phase and amplitude of a femtosecond pulse probing a laser-produced plasma”, Opt. Lett. **19**, 1997 (1994) doi:10.1364/OL.19.001997

[6] E.A. Schneidmiller, M.V. Yurkov: “Photon beam properties at the European XFEL”, XFEL.EU TR-2011-006 (2011) doi:10.3204/DESY11-152

[7] H. Sinn, J. Gaudin, L. Samoylova, A.Trapp, G. Galasso: “Conceptual Design Report: X-Ray Optics and Beam Transport”, XFEL.EU TR-2011-002 (2011) doi:10.3204/XFEL.EU/TR-2011-002

[8] G. Geloni et al.: “A novel self-seeding scheme for hard X-ray FELs”, J. Mod. Opt. **58**, 1391 (2011) doi:10.1080/09500340.2011.586473

[9] J. Amann et al.: “Demonstration of self-seeding in a hard-X-ray free-electron laser”, Nature Photonics **6**, 693–698 (2012) doi:10.1038/nphoton.2012.180

[10] B. Lengeler et al.: “Imaging by parabolic refractive lenses in the hard X-ray range” J. Synchrotron Rad. **6**, 1153 (1999) doi:10.1107/S0909049599009747

[11] A. Madsen et al., “Technical Design Report: Scientific Instrument Materials Imaging and Dynamics (MID)”, XFEL:EU TR-2013-005 (2013) doi:10.3204/XFEL.EU/TR-2013-005

[12] O. Chuba, M.-E. Couprie, M. Labat et al.: “Time-dependent FEL wavefront propagation calculations: Fourier optics approach”, Nuclear Instruments and Methods in Physics Research Section A: Accelerators, Spectrometers, Detectors and associated Equipment **593**, 30–34 (2008) doi:10.1016/j.nima.2008.04.058

[13] L. Samoylova, A. Buzmakov, G. Geloni et al.: “Cross-platform wave optics software for XFEL applications”, Advances in Computational Methods for X-Ray Optics II, San Diego, California, 23 September 2011, Proc. SPIE **8141**. 81410A (2011) doi:10.1117/12.893044

[14] S. Rohling et al.: “Optical design and time-dependent waverfront propagation simulation for a hard x-ray split-and-delay unit for the European XFEL”, Proceedings of FEL2013 WEPSO56 (2013)

[15] D. Shu et al.: “Precision mechanical design of an UHV-compatible artificial channel cut X-ray monochromator”, Proc. SPIE **6665**, 66650O-1 (2007) doi:10.1117/12.733101

[16] H. Sinn, M. Dommach, X. Dong et al.: “Technical Design Report: X-Ray Optics and Beam Transport”, XFEL.EU TR-2012-006 (2012) doi:10.3204/XFEL.EU/TR-2012-006

[17] D. Zhu et al.: “A single-shot transmissive spectrometer for hard x-ray free electron lasers”, Applied Physics Letters **101**, 034103 (2012) doi:10.1063/1.4736725

[18] P. Karvinen et al.: “Single-shot analysis of hard X-ray free electron laser radiation using a non-invasive grating spectrometer”, Optics Letters, **37**, 5073–5075 (2012) doi:10.1364/OL.37.005073

[19] C. Ozkan: “Conceptual Design Report: Imaging Stations for Invasive Photon Diagnostics”, XFEL.EU TR-2012-004 (2012) doi:10.3204/XFEL.EU/TR-2012-004

[20] F. Yang: “Technical Specification for Front-End WP73”, XFEL.EU (2013)

[21] M.J. Lederer, M. Pergament, M. Kellert, C. Mendez: “Pump-probe laser development for the European X-ray Free-Electron Laser facility”, X-Ray Free-Electron Lasers: Beam Diagnostics, Beamline Instrumentation, and Applications, San Diego, USA, 12 August 2012, Proc. SPIE **8504** (2012) doi:10.1117/12.928961

[22] G. Cerullo, S. De Silvestria: “Ultrafast optical parametric amplifiers”, Rev. Sci. Inst. **74**, 1 (2003) doi:10.1063/1.1523642

[23] Y. Inubushi, K. Tono, T. Togashi et al.: “Determination of the Pulse Duration of an X-Ray Free Electron Laser Using Highly Resolved Single-Shot Spectra”, Phys. Rev. Lett. **109**, 144801 (2012) doi:10.1103/PhysRevLett.109.144801

[24] M. R. Bionta, H.T. Lemke, J.P. Cryan et al.: “Spectral encoding of x-ray/optical relative delay”, Optics Exp. **19**, 21855 (2011) doi:10.1364/OE.19.021855

[25] M. Beye, O. Krupin, G. Hays et al.: “X-ray pulse preserving single-shot optical cross-correlation method for improved experimental temporal resolution”, Appl. Phys. Lett. **100**, 121108.1–121108.4 (2012) doi:10.1063/1.3695164

[26] M. Harmand, R. Coffee, M.R. Bionta et al.: “Achieving few-femtosecond time-sorting at hard X-ray free-electron lasers”, Nature Photonics **7,** 215–218 (2013) doi:10.1038/nphoton.2013.11

[27] N. Medvedev, H.O. Jeschke, B. Ziaja: “Nonthermal graphitization of diamond induced by a femtosecond x-ray laser pulse”, Phys. Rev. B **88**, 224304 (2013) doi:10.1103/PhysRevB.88.224304

[28] N. Medvedev: “Conceptual design for femtosecond hard x-ray pulse-duration monitor”, submitted.

[29] N. Medvedev. H.O. Jeschke, B. Ziaja: “Nonthermal phase transitions in semiconductors induced by a femtosecond extreme ultraviolet laser pulse”, New J. Phys. **15** 015016 (2013) doi:10.1088/1367-2630/15/1/015016

[30] T.R. Schibli: “Attosecond active synchronization of passively mode-locked lasers by balanced cross correlation”, Opt. Lett. **28**, 947 (2003) doi:10.1364/OL.28.000947

[31] G. Gregori, D.O. Gericke: “Low frequency structural dynamics of warm dense matter”, Phys. Plasmas **16**, 056306 (2009) doi:10.1063/1.3100203

[32] H.T. Lemke et al.: “Femtosecond X-ray Absorption Spectroscopy at a Hard X-ray Free Electron Laser: Application to Spin Crossover Dynamics”, J. Phys. Chem. A **117**, 735 (2012) doi:10.1021/jp312559h

[33] A. Mancic et al.: “Picosecond Short-Range Disordering in Isochorically Heated Aluminum at Solid Density”,
Phys. Rev. Lett. **104**, 035002 (2010)
doi:10.1103/PhysRevLett.104.035002

[34] A. Schropp et al.: “Full spatial characterization of a nanofocused x-ray free-electron laser beam by ptychographic imaging”,
Sci. Rep. **3**, 1633 (2013)
doi:10.1038/srep01633;
A. Schropp et al.: “Scanning coherent x-ray microscopy as a tool for XFEL nanobeam characterization”, SPIE **8849**, 88490R
doi:10.1117/12.2024784

[35] R. Stephens et al.: Workshop on Petawatt Lasers at Hard X-Ray Light Sources, Dresden Germany, 5–9 Septtember 2011

[36] A.W. Moore: “Chemistry and physics of carbon: highly oriented pyrolytic graphit”, Marcel Dekker, New York, U.S.A. (1973)

[37] U. Zastrau et al.: “Focal aberrations of large-aperture HOPG von-Hàmos x-ray spectrometers”, JINST **7**, P09015 (2012)
doi:10.1088/1748-0221/7/09/P09015;
U. Zastrau et al.: “Characterization of strongly-bent HAPG crystals for von-Hámos x-ray spectrographs”, JINST **8**, P10006 (2013)
doi:10.1088/1748-0221/8/10/P10006

[38] P. Antici et al.: “Time and space resolved interferometry for laser-generated fast electron measurements”,
Rev.Sci. Inst. **81**, 113302 (2010)
doi:10.1063/1.3499250

[39] P.M. Celliers et al.: “Line-imaging velocimeter for shock diagnostics at the OMEGA laser facility”, Rev. Sci Inst. **75**, 4916 (2004)
doi:10.1063/1.1807008

[40] J.E. Miller et al.: “Streaked optical pyrometer system for laser-driven shock-wave experiments on OMEGA”, Rev. Sci. Inst. **78**, 034903 (2007)
doi:10.1063/1.2712189

[41] G. Galasso, H. Sinn: “Heat Load Calculations for Spontaneous Radiation Apertures”, European XFEL Technical Report,
EDMS No. 2004661 (2011)
http://edmsdirect.desy.de/edmsdirect/file.jsp?edmsid=2004661